TURBULENCE-COPEPOD INTERACTION: *ACARTIA TONSA* BEHAVIORAL RESPONSE TO BURGERS′ VORTEX

A Thesis
Presented to
The Academic Faculty

by

David Louis Young

In Partial Fulfillment
of the Requirements for the Degree
Master of Science in the
School of Civil and Environmental Engineering

Georgia Institute of Technology
August 2014

TURBULENCE-COPEPOD INTERACTION: *ACARTIA TONSA* BEHAVIORAL RESPONSE TO BURGERS' VORTEX

Approved by:

Dr. Donald R. Webster, Advisor
School of Civil and Environmental Engineering
Georgia Institute of Technology

Dr. Jeannette Yen
School of Biology
Georgia Institute of Technology

Dr. Kevin Haas
School of Civil and Environmental Engineering
Georgia Institute of Technology

Date Approved: 2 June 2014

ACKNOWLEDGEMENTS

I am grateful to so many individuals who helped me along the path to submitting this thesis that I could write a treatise on all of your contributions. This section is in no way a complete list of all the assistance I have been offered, whether it was kind words of encouragement or basically doing half my Tomo-PIV experiments for me (looking at you Daniel!).

This thesis has been the most herculean scholastic task I have undertaken, and it's just my Masters thesis! I can only imagine how crushing my PhD thesis will be. At several different points along the way I really wanted to be finished with it, and I want to thank those who really helped keep me from caving in. First and foremost I want to thank my Lord and Savior, Jesus Christ. Thank you for staying with me, and carrying me when I could not carry myself. Thank you for blessing me when I do not deserve it. Chief among my long list of blessing that I am not worth are my parents, Louis and Danita Young. Everything that I have accomplished and will accomplish is a direct result of your unwavering belief and support in me. I also want to single out both Aaron True and David Murphy for giving me advice an encouragement; it's a hard road to walk, and I appreciate both of you who have gone before helping me along the way. Lastly, thank you Dr. Haas for being a (somewhat?) willing sound board for my frustrations; I really appreciate the chance to discuss them with someone further along in their academic career.

Equally as important as the encouragement required to complete this thesis is the expertise. There is no better person to start with when discussing expertise than Dr. Webster. I could not wish for a better and more knowledgeable person to work for and to advise me. Thank you for your wisdom and your patience, as well as your

investment in and your commitment to me. Similarly, Dr. Yen, thank you for your knowledge and your truly impressive enthusiasm for your work.

In addition, I want to take this opportunity to thank the many students who shared what they knew with me, to fill in the (enormous) gaps in my own knowledge. First amongst them is Aaron True, who has helped me with everything from Matlab code, to planar PIV, to statistical analysis, and everything in between. I know you had a lot of stuff going on, and I appreciate you making the time to help me; it's definitely something I will remember when I'm slammed with my own PhD thesis and one of the other graduate students needs my help. Right behind him is Daniel Borrero, who basically tutored me through my entire Tomo-PIV data collection. There is literally no way I would have finished this thesis without your help and, as with Aaron, I know you had other things you needed to do, so I really appreciate you taking the time to help me. I also want to thank Rachel Lasley-Rasher for continuing to send me *Acartia*, even after I managed to kill them all, and Larisa Pender-Healy for teaching me how to keep them alive long enough to run my experiments.

One area in particular in which I desperately needed some assistance was in building the Burgers Vortex Apparatus. I basically had no idea how to take the little sketch I had drawn in my lab notebook and turn it into a functional device. Fortunately, Mr. Andy Udell took the time to build the device with me. Andy helped me with basically everything involved with the procurement of the device, from the material acquisition, to fashioning the components, to the final assembly of the device. The Burgers vortex apparatus would have been renamed worthless pile of junk had I not had your help building it, so thank you Andy.

Last, but certainly not least, I want to single out the three undergrads that manually tracked many of my *Acartia* videos in DLTdv5. Perhaps no one understands more than me how mind numbing it can be (well, Aaron probably does), and over the Christmas break the thought of tracking all the videos myself was crushing my

spirit. So I want to extend a big thanks to Briana Corcoran, John Jung, and Jennifer Young, for helping me shoulder that burden.

TABLE OF CONTENTS

LIST OF TABLES

LIST OF FIGURES

SUMMARY

The purpose of this study is to quantify the effect of finescale turbulence on copepod behavior in order to shed light on the influence of turbulence on copepod distribution. Specifically, the study will examine the behavioral response of the marine copepod *Acartia tonsa* to a steady state Burgers′ vortex intended to mimic the characteristics of a turbulent vortex (Jumars et al. [2009]) that a copepod is likely to encounter in the coastal zone. A laboratory apparatus was constructed to create a Burgers′ vortex with size and strength consistent with turbulence vortices in the coastal zone (and relevant to the marine copepod species). The radius, circulation, and axial strain of the Burgers′ vortex were specified to match typical dissipative vortices corresponding to two turbulence intensity levels. The levels are described by Webster et al. [2004] as Level 2 ($\epsilon = 0.009\ cm^2/s^3$) and Level 3 ($\epsilon = 0.096\ cm^2/s^3$), which span an apparent behavior transition in copepods [Yen et al., 2008].

Tomographic particle image velocimetry (Tomo - PIV) was performed to calibrate the device and verify that it produces the desired vortex characteristics, as well as to provide a three dimensional velocity vector field to compare with behavioral assays. The laboratory apparatus, dubbed the "Burgers′ Vortex Apparatus", accurately reproduces the appropriate vortex characteristics of the Turbulence Level 2 and 3 vortex cartoons. Copepod behavioral assays were conducted with *Acartia tonsa*.

When exposed to these vortices, *Acartia tonsa* did not exhibit a meaningful behavioral response to the Level 2 vortices, but drastically altered their swimming behavior in the presence of Level 3 vortices. In the presence of a Turbulence Level 3 vortex, *Acartia tonsa* increased relative swim speed, decreased turn frequency, increased the

angle of alignment with the vortex axis, increased net-to-gross displacement ratio, and increased escape acceleration (relative to control). These alterations in swimming kinematics all served to move the animal away from the vortex core.

CHAPTER I

INTRODUCTION

The interaction between small biological organisms and turbulence remain fascinating and mysterious to biological oceanographers. Studies by Rothschild and Osborn [1988], Saiz and Kiørboe [1995], and Incze et al. [2001] in particular have raised puzzling open ended questions regarding the effect of the hydrodynamic forcing imposed on small organisms such as copepods due to the turbulent flow field they inhabit. It is known that copepods are of similar size to the Kolmogorov microscale in coastal-zone turbulence [Jimenez, 1997] and typically swim at speeds on the order of the fluctuating fluid velocity [Yamazaki and Squires, 1996], effectively linking the study of finescale turbulent velocity fluctuations to the behavior of copepods in coastal environments. It is likely that the effects of turbulence on copepod behaviors such as feeding rate, growth rate, predator prey interaction etc..., are species specific (Dower et al. [1997], Marrase et al. [2000], MacKenzie [2000], Peters and Marrase [2000]), indicating that fully understanding the interaction of zooplankters and turbulence will prove to be a herculean task (e.g. Jonsson and Tiselius [1990], Saiz and Alcaraz [1992], Yamazaki [1996], Visser et al. [2001], Saiz et al. [2003], Galbraith et al. [2004], Lewis [2005]). One observation of species-specific turbulence mediation of copepod behavior is the variable vertical distribution of copepod species, seemingly in response to the distribution of turbulence intensity within the water column [Heath et al., 1988, Haury et al., 1990, Mackas et al., 1993, Lagadeuc et al., 1997, Incze et al., 2001, Visser et al., 2001, Manning and Bucklin, 2005]. Intuitively grasping that the physical forcing of turbulence mediates the vertical distribution of copepods is relatively straightforward, however understanding the role that changes in copepod

behavior in response to hydrodynamic cues associated with the turbulent velocity fluctuations play in the vertical distributions of copepods is more difficult to fathom, and more difficult still to quantify.

To tackle this challenge, one must first understand how copepods collect sensory information from the surrounding environment, specifically, how they detect the hydrodynamic cues associated with the velocity fluctuations. To detect hydrodynamic signals, copepods possess an array of mechanosensory hairs, called setae, on many of their appendages. These setae are most numerous and most sensitive along the copepod antennae [Yen and Fields, 1992, Boxshall et al., 1997, Fields et al., 2002]. These setae bend in response to velocity differences between the animal and the ambient fluid. The sensitivity of copepods to hydrodynamic cues is truly impressive. For example, Yen et al. [1992] reported that copepods detect displacements as small as 10 nm and Woodson et al. [2005] reported sensitivities to strain rate as low as 0.025 s^{-1}. Several studies have attempted to isolate the specific hydrodynamic cues that elicit certain copepod responses, with most of them concluding that the hydrodynamic cue that elicits escape response is the strain rate [Haury, 1980, Fields and Yen, 1997, Kiørboe et al., 1999].

The very nature of turbulence presents unique challenges to those who wish to merely quantify the velocity field, let alone perform animal assays in the presence of such a flow. Turbulent flows are characterized by (among other things) their random and unpredictable nature. Further, the velocity fluctuations are intermittent, which presents itself as infrequent but extreme peaks and troughs in both the time record of flow velocity and the difference in flow velocity between points in physical space (at the same time). This presents enormous difficulties to an individual wishing to perform behavioral assays of organisms such as copepods in a turbulent flow field. One cannot be sure when the organism will swim through the experimental control volume and there is no way to anticipate the instantaneous turbulent velocity field

characteristics. Therefore, fully time resolved three-dimensional velocity data must be constantly acquired throughout the behavioral assay. Furthermore, many of the copepod behaviors that are of interest (such as escape jumps) are relatively infrequent events, and the events must occur within the experimental control volume while data are being taken (such that the hydrodynamic cues triggering the event are quantified). Compounding this issue is the fact that experimental flow imaging techniques that allow fully time resolved three-dimensional velocity data collection, such as Tomo-PIV, have a limited range of scales that necessitates a relatively small measurement volume to meet resolution requirements around the zooplankton [Murphy et al., 2012]. Continuously taking flow data, while waiting for an animal to swim through the necessarily small control volume and perform an infrequent escape jump (or behavior modification) is a recipe for countless hours of behavioral assays to acquire even a few quantified behavior events.

As the icing on the difficulty cake, it is all but impossible to determine a set hydrodynamic cue (i.e., strain rate, vorticity etc...) threshold with this approach. Since the flow field is constantly varying in space and time, there is no way to quickly test copepod response to a specific value of, say, strain rate, because there is no way to fix the strain rate to that specific value in a turbulent flow field. The only available approach is to collect a cornucopia of data, such that a distribution of copepod response as a function of strain rate (or other parameters of interest) can be calculated in hopes of identifying a behavior transition. Acquiring even a few of these data points is a monumental task, and this approach requires a multitude to achieve statistically significant results.

It would be very convenient therefore to create a steady state flow field that could mimic the important characteristics of a turbulent flow field, allowing one to take a single set of Tomo-PIV data to quantify the velocity field, and then perform the

animal behavior assays separately. Jumars et al. [2009] presents a theoretical turbulence cartoon to accomplish this by exploiting characteristics of isotropic turbulence. Recent Direct Numerical Simulation (DNS) experiments indicate that microscale turbulence is best described as a writhing tangle of vortex worms [Yokokawa et al., 2002]. Further numerical simulations by Hatakeyama and Kambe [1997] indicate that an ensemble of Burgers′ vortices under the right conditions can accurately mimic critical flow characteristics of isotropic turbulence. Combining these concepts, Jumars et al. [2009] presents a method to mimic a single turbulence vortex "worm" with a Burgers′ vortex "cartoon", given certain statistical characteristics of the corresponding turbulent flow field.

The current study designs and constructs a laboratory realization of the Jumars et al. [2009] turbulent vortex cartoon and quantifies the three-dimensional flow pattern via Tomo-PIV. Target turbulent vortex parameters are specified from isotropic turbulence Levels 2 and 3 in the Webster et al. [2004] T-Box experiments. The goal of this study is to test the hypothesis that the copepod *Acartia tonsa* senses hydrodynamic cues in turbulent flows and actively responds via changes in swimming kinematics (acting to remove the copepod from the vortex region).

CHAPTER II

LITERATURE REVIEW

Copepods, found in marine and freshwater ecosystems, are considered to be the most numerous multicellular organisms on earth [Wiebe et al., 1992, Humes, 1994]. These small aquatic crustaceans, typically 0.5 to 3.0 mm in length, are a major food source for multiple aquatic species such as krill, fish, and some species of whales [Mauchline, 1998]. In addition they are critical consumers of phytoplankton [Kleppel, 1993, Bronmark and Hansson, 2005, Gretchen et al., 2006]. As the dominant (both in terms of numbers and biomass) subset of mesozooplankton in marine waters, copepods play a crucial role in marine ecosystems [Mauchline, 1998, Miller, 2004]. As a result, there is significant interest in better understanding how copepods interact with the marine environment.

The topics considered in this review are intended to provide the reader with the necessary copepod sensory ecology and behavioral background, as well as some critical fluid mechanics and turbulence knowledge to form the foundation for this study.

2.1 Copepod Locomotion and Ecology

2.1.1 Copepod Swimming Behavior

Copepod locomotion can be divided into two main categories, cruise swimming and jumping [Jiang et al., 2002]. During cruise swimming, the animals forward propulsion is provided by the rapid beating of the paired cephalic appendages. Body position, swim direction, and swim velocity are highly depend on copepod size and species

[Jiang et al., 2002, Murphy, 2012].

While jumping, copepods stroke their antennae and larger swimming legs [Yen, 2000, Jiang et al., 2002]. This causes the copepod to rapidly accelerate, reaching swimming velocities of up to 1 m/s; this allows a given copepod to exceed its typical cruise swimming velocity by one to two orders of magnitude [Yen, 2000, van Duren and Videler, 2003, Lenz et al., 2004]. This behavior can serve to reposition the animal, close in on prey, or to escape a potential predator [Murphy, 2012].

Jumps performed in an effort to escape a predator are a special subset of jump behavior referred to as escape jumps, also referred to as an escape reaction elsewhere in this document [Yen, 2000]. Escape jumps are characterized by the copepod stroking their swimming appendages multiple times and, as a result, escape jumps are much more powerful than ordinary jumps [Yen, 2000]. It follows that the maximum velocities given for copepod movement generally occur during escape jumps.

Alterations in jump behavior is one of the most distinctive markers of copepod behavioral response, as the jumps are clear and drastic deviations from muted cruise swimming behavior.

2.1.2 Foundational Mechanics Analysis of Fluid Elements

This section provides a brief overview of the concept of fluid strain (deformation) rate, the distinction between strain rate and rotation rate, as well as the difference between linear strain rate and shear strain rate (the components of strain rate). The foundational fluid mechanics discussion is critical for a physical understanding of the flows and for understanding copepod mechanosensing response. This section makes some use of index notation; shorthand notation for dealing with vectors and matrices. In index notation, non-scalar quantities are given one or more subscripts (indices), which correspond to specific elements in the vector (or matrix) quantity. In fluid

mechanics, these indices generally have values of 1, 2, or 3, corresponding to the x, y, and z coordinate directions. For example, the velocity vector $\vec{u}$ is written in index notation as u_i. The velocity in the x-direction is given by u_1, the y-direction velocity by u_2 etc.... The three dimensional velocity gradient, $\frac{\partial u_i}{\partial x_j}$, is a second order tensor; as such it has 9 distinct components [Kundu and Cohen, 2004]. This tensor can be decomposed into symmetric and anti-symmetric parts. Symmetric tensors are symmetric about the diagonal elements, whereas for anti-symmetric tensors the elements mirrored across the diagonal are equal in magnitude and possess the opposite sign. This decomposition is shown below [Kundu and Cohen, 2004].

$$\frac{\partial u_i}{\partial x_j} = e_{ij} + \frac{1}{2} r_{ij} \tag{2.1}$$

In the above equation, e_{ij} corresponds to the strain (deformation) rate tensor, and r_{ij} to the rotation tensor.

The strain rate tensor is defined as [Kundu and Cohen, 2004]:

$$e_{ij} = \frac{1}{2}\left(\frac{\partial u_i}{\partial x_j} + \frac{\partial u_j}{\partial x_i}\right) = \begin{vmatrix} \frac{\partial u_1}{\partial x_1} & \frac{1}{2}\left(\frac{\partial u_2}{\partial x_1} + \frac{\partial u_1}{\partial x_2}\right) & \frac{1}{2}\left(\frac{\partial u_3}{\partial x_1} + \frac{\partial u_1}{\partial x_3}\right) \\ \frac{1}{2}\left(\frac{\partial u_2}{\partial x_1} + \frac{\partial u_1}{\partial x_2}\right) & \frac{\partial u_2}{\partial x_2} & \frac{1}{2}\left(\frac{\partial u_3}{\partial x_2} + \frac{\partial u_2}{\partial x_3}\right) \\ \frac{1}{2}\left(\frac{\partial u_3}{\partial x_1} + \frac{\partial u_1}{\partial x_3}\right) & \frac{1}{2}\left(\frac{\partial u_3}{\partial x_2} + \frac{\partial u_2}{\partial x_3}\right) & \frac{\partial u_3}{\partial x_3} \end{vmatrix} \tag{2.2}$$

And physically corresponds to the superposition of linear and shear strain rate. Linear strain can be considered as a stretching of a fluid element along a specific reference axis, whereas shear strain "is defined as the rate of decrease of the angle formed by two mutually perpendicular lines on the (fluid) element" [Kundu and Cohen, 2004].

The rotation tensor is defined as [Kundu and Cohen, 2004]:

$$r_{ij} = \frac{\partial u_i}{\partial x_j} - \frac{\partial u_j}{\partial x_i} = -\varepsilon_{ijk}\omega_k = \begin{vmatrix} 0 & -\left(\frac{\partial u_2}{\partial x_1} - \frac{\partial u_1}{\partial x_2}\right) & -\left(\frac{\partial u_3}{\partial x_1} - \frac{\partial u_1}{\partial x_3}\right) \\ \left(\frac{\partial u_2}{\partial x_1} - \frac{\partial u_1}{\partial x_2}\right) & 0 & -\left(\frac{\partial u_3}{\partial x_2} - \frac{\partial u_2}{\partial x_3}\right) \\ \left(\frac{\partial u_3}{\partial x_1} - \frac{\partial u_1}{\partial x_3}\right) & \left(\frac{\partial u_3}{\partial x_2} - \frac{\partial u_2}{\partial x_3}\right) & 0 \end{vmatrix} \quad (2.3)$$

The rotation tensor physically corresponds to the relative fluid velocity due solely to solid body rotation of the fluid element (i.e., if the fluid element did not deform at all). Another parameter of interest closely related to the rotation tensor is vorticity. The vorticity ($\vec{\omega}$) is defined as the curl of the velocity vector ($\vec{V}$):

$$\vec{\omega} = \nabla \times \vec{V} = \begin{bmatrix} \frac{\partial u_3}{\partial x_2} - \frac{\partial u_2}{\partial x_3} \\ \frac{\partial u_1}{\partial x_3} - \frac{\partial u_3}{\partial x_1} \\ \frac{\partial u_2}{\partial x_1} - \frac{\partial u_1}{\partial x_2} \end{bmatrix} \quad (2.4)$$

By inspection, it is clear that the elements in the vorticity vector correspond to the off diagonal terms in the rotation tensor.

Thus, the velocity gradient tensor consists of the sum of both pure rigid body rotation and pure strain (deformation) of a fluid element.

2.1.3 Mechanosensing and Relevant Studies

To detect predators, mates, and food, copepods rely upon chemoreception and mechanoreception, the latter of which will be the focus of this thesis [Strickler and

Bal, 1973, Lenz et al., 1996, Yen et al., 1992]. Mechanoreception, as it relates to copepods, refers to the animals ability to detect nearby fluid motion [Mauchline, 1998]. To facilitate detection of fluid flow parameters, copepods posses an array of mechanosensory hairs (called setae) on many appendages; these setae are most numerous and most sensitive along the paired antennae [Yen and Fields, 1992, Boxshall et al., 1997, Fields et al., 2002].

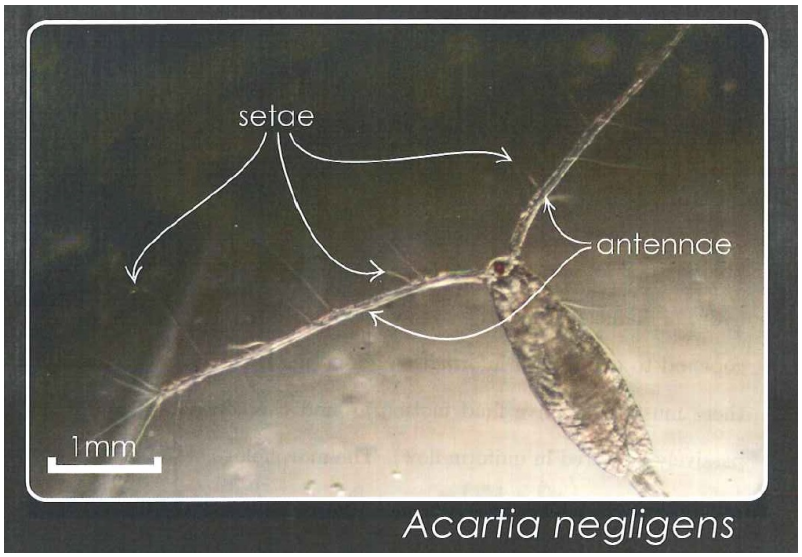

Figure 2.1: Image of *Acartia negligens* identifying the setae and antennae, reprinted from True [2011].

These hairs give the animals the ability to sense fluid motion by bending in response to a velocity difference between the copepod and the surrounding fluid [Fields et al., 2002, True, 2011]. Utilizing these setae, copepods possess impressive sensitivity to relative fluid motion, detecting displacements as small as 10 nm in studies by Yen et al. [1992]. Woodson et al. [2005] reported sensitivities to thin layer structure with strain rate thresholds as low as 0.025 s^{-1}.

The majority of studies to date have specifically focused on the copepods ability to detect predators. Pioneering studies by Haury [1980] investigated the effects of fluid acceleration, total fluid strain, strain rate, and pressure on *Calanus finmarchicus*.

Their results suggested that strain-rate-related parameters correlated most closely with animal response. Subsequent work by Fields and Yen [1996, 1997] exposed copepods to a siphon flow in an attempt to mimic the feeding current of a larger predator. The escape behavior of copepods was spatially quantified and related to the flow velocity and strain rate. Fields and Yen [1997] found that strain rate was the least variable characteristic eliciting an escape reaction, in agreement with the earlier hypothesis of Haury [1980]. The threshold value necessary to provoke an escape response varied considerably among copepod species [Fields and Yen, 1997]. Research by Kiørboe et al. [1999] utilized a series of experiments in different laminar flow fields in an attempt to expose copepods to a specific flow parameter with the goal of better isolating the fluid mechanical cue (acceleration, vorticity, linear or shear strain rate) that best explained copepod behavior. They also concluded that strain rate was the critical flow parameter and that, for *Acartia tonsa* females, the threshold strain rate value was a constant, regardless of whether the copepod was exposed to pure linear or pure shear strain [Kiørboe et al., 1999]. Analysis by Kiørboe and Visser [1999] indicated that while perception of predators depends on velocity gradient related parameters, such as strain rate, vorticity or acceleration, perception of prey relies solely on the magnitude of the fluid velocity.

2.2 Turbulence and Turbulence-Copepod Interactions

Turbulence is a fluid flow phenomenon that arises from instabilities in the fluid flow that form and propagate at high Reynolds numbers. The Reynolds number, shown below, is a dimensionless parameter that gives the relative importance of inertial forces to viscous forces in a fluid flow.

$$Re = \frac{vL}{\nu} \tag{2.5}$$

In this equation v is the fluid velocity, L is the characteristic length scale, and ν is the kinematic viscosity of the fluid.

Practically speaking, instabilities form in all fluid flows. However, at low Reynolds numbers, viscous dampening eventually eliminates the disturbances, not allowing them to propagate. At some threshold value of the Reynolds number (variable, depending on the type of flow) flow instabilities will no longer be controlled by viscous dampening. Instead the instabilities propagate and eventually becomes truly chaotic, or turbulent [Kundu and Cohen, 2004].

When dealing with turbulence, it is convenient to break the velocity vector into two components, the mean component and the fluctuating component - defined as the deviation from the mean velocity. This decomposition is shown:

$$u(\vec{x}, t) = \bar{u}(\vec{x}, t) + u'(\vec{x}, t) \tag{2.6}$$

where u is the x-direction component of velocity, $\bar{u}$ is the time-averaged value, and u' is the fluctuating component.

2.2.1 Characteristics of Turbulent Flows

A major reason why it is convenient to decompose the velocity in this manner when dealing with turbulent flows is that they are characterized by (among other things) their random and unpredictable nature. The velocity fluctuations are intermittent, which presents itself as infrequent but extreme peaks and troughs in the time record of flow velocity. Turbulent flows are also diffusive, meaning they result in rapid mixing of heat, momentum, fluid particles etc... [Kundu and Cohen, 2004].

Turbulence can be thought of as consisting of a host of semi-coherent structures, called eddies that are constantly moving, reorienting, and evolving [Kundu and Cohen, 2004]. The size of these eddies span a wide range of scales. The largest structures are on the order of the size of the "container" (such as the depth of the ocean) and the smallest are on the order of *mm* [Kundu and Cohen, 2004]. This feature makes turbulence extremely difficult to study, as any instrumentation must be large enough to capture very large scale motions as well as sensitive enough to detect fluid motion at the microscales.

Most of the energy in turbulent flows is contained in the largest eddies. This energy is transferred to slightly smaller eddies, then to smaller eddies still, until it at last reaches the smallest structures [Kundu and Cohen, 2004]. This process is referred to as the energy cascade, and was first identified by Lewis Richardson in 1922 [Kundu and Cohen, 2004]. Once the energy reaches the smallest eddies, it is dissipated as heat due to the effects of viscosity, leading to the last important characteristic of turbulent flows discussed here; they require a constant source of energy to make up for the energy lost due to viscous dissipation [Kundu and Cohen, 2004].

The rate of dissipation, ϵ, is given by the expression [Tennekes and Lumley, 1972]:

$$\epsilon = 2\nu\overline{s_{ij}s_{ij}} \tag{2.7}$$

In the above expression ν is the kinematic viscosity and s_{ij} is the strain rate of the velocity *fluctuations*, given by:

$$s_{ij} = \frac{1}{2}\left(\frac{\partial u_i'}{\partial x_j} - \frac{\partial u_j'}{\partial x_i}\right) \tag{2.8}$$

The expression for ϵ can be simplified considerably if certain conditions are met, as will be addressed later.

2.2.2 Scaling Relationships, Homogeneity, and Isotropy

As mentioned previously, turbulent eddies span a wide range of scales, ranging from the size of the container, to the order of millimeters. Several scaling relationships have been developed to quantify certain critical eddy sizes, the most relevant of which will be discussed here.

The Kolmogorov length scale, η, provides a scaling relationship for the size of the smallest (or dissipative) eddies in a turbulent flow [Kolmogorov, 1941], and can be estimated using the following expression:

$$\eta = \left(\frac{\nu^3}{\epsilon}\right)^{\frac{1}{4}} \tag{2.9}$$

Marine copepods are often as small as or smaller than the size of the Kolmogorov length scale in a typical coastal zone turbulence [Lazier and Mann, 1989]. This is critical in the context of turbulence research, due to the concept of local isotropy. In his seminal 1941 paper, Kolmogorov hypothesized that, at sufficiently high Reynolds numbers, turbulent flows are homogeneous and locally isotropic [Kolmogorov, 1941]. That is to say that if the distances between two points in a turbulent flow field are small enough then the statistics of the turbulent velocity fluctuations are both independent of translation of the coordinate axis (homogeneous) as well as independent of both arbitrary rotation and arbitrary reflection of the coordinate axis (isotropic) [Pope, 2000]. For future reference, statistical isotropy implies statistical homogeneity, however the reverse is untrue (i.e., all isotropic flows are homogeneous, but not all

homogeneous flows are isotropic). Therefore, elsewhere in this thesis it is understood that isotropic turbulence is necessarily homogeneous.

Isotropic turbulent flows are considerably easier to work with than non-isotropic turbulent flows, simplifying many equations frequently encountered in discussions of turbulent flow fields. For example, in isotropic turbulence the dissipation rate, ϵ, discussed in the previous section, may be formulated as [Tennekes and Lumley, 1972]:

$$\epsilon = 15\nu\overline{\left(\frac{\partial u_1}{\partial x_1}\right)^2} \tag{2.10}$$

Another scale of interest, used later to define some experimental parameters, is the Taylor microscale. Denoted by the Greek symbol λ, it is a length scale that loosely corresponds to the eddy size at which dissipation rate, flow kinetic energy, and viscosity all interact [Taylor, 1921], and is given as:

$$\lambda = \sqrt{\frac{15\nu}{\epsilon}}u_{rms} \tag{2.11}$$

Further, one can form the Taylor-scale Reynolds number by combining the root mean square of the velocity fluctuations (u_{rms}) with the Taylor-scale Reynolds number, shown below [Pope, 2000]:

$$Re_\lambda = \frac{u_{rms}\lambda}{\nu} \tag{2.12}$$

2.2.3 Cartoons

As Jumars et al. [2009] mentions, the way turbulence is conceptualized has been greatly affected by the exponential increase in available computing power, and the accompanying rise of direct numerical simulations of turbulent flows. As an example, he notes that recent direct numerical simulations (DNS) and experiments illustrate microscale turbulence as a writhing tangle of vortex worms [Yokokawa et al., 2002]. Jumars et al. [2009] notes that this stands in stark contrast to the long held argument that at the scale of a typical copepod, the flow field is comprised of steady shear flow with constant vorticity [Lazier and Mann, 1989].

To facilitate applying this new understanding of turbulence to experimental marine copepod research, Jumars et al. [2009] proposes using what he refers to as a vortex cartoon. They reason that if turbulent motion at the microscale is in fact comprised of many individual vortices, then perhaps useful information about plankton behavior in a turbulent environment can be gleaned by examining the vortex/plankton interaction. This lab generated vortex would necessarily possess similar flow characteristics to that of isotropic turbulence in a typical coastal zone marine environment, such that it is applicable to plankton research.

2.2.4 Turbulence in the Marine Environment

It is critical to have a sense of the fluid environment a marine copepod is likely to experience. The objective is to be certain the vortex cartoon will be an accurate representation of the in situ flow field. Fortunately, substantial work has been done in this area by Webster et al. [2004], in their development of an apparatus to create a homogeneous isotropic turbulent flow field at scales relevant to copepod research.

Webster et al. [2004] describes the apparatus, colorfully dubbed the "T-Box", which generates nearly isotropic and homogeneous turbulence. They also provide the turbulence parameters for four different turbulence levels, intended to approximate typical turbulence found in the coastal zone, and compares them to several field studies of oceanic turbulence conducted by other researchers to verify their relevancy [Webster et al., 2004].

Tables 2.1, 2.2 and 2.3 contain the turbulence parameters for each of the four turbulence levels from the Webster et al. [2004] "T-Box" experiments:

Table 2.1: Flow statistics in the 1 & 3 directions (x and z) for each of the four turbulence levels in the Webster et al. [2004] "T-Box", including mean velocity, root mean square of the velocity fluctuations, ratio between them etc... Reprinted from Webster et al. [2004] (Table 2).

Turbulence Level	**1**	**2**	**3**	**4**
$\langle U_1 \rangle$ (cm/s)	-0.07	-0.03	0.18	0.07
$\langle U_3 \rangle$ (cm/s)	-0.11	0.07	0.12	0.22
$\langle u_{1_{rms}} \rangle$ (cm/s)	0.081	0.30	0.69	0.88
$\langle u_{3_{rms}} \rangle$ (cm/s)	0.089	0.27	0.78	0.91
$\langle u_{1_{rms}}/u_{3_{rms}} \rangle$	0.91	1.11	0.89	0.98
$\overline{(u_1' u_3')}$ (cm^2/s^2)	0.001	-0.004	-0.002	-0.058
Skewness, u_1	-0.6	-0.5	0.0	0.1
Skewness, u_3	-0.2	0.2	0.1	-0.2
Kurtosis, u_1	3.5	3.3	3.2	3.2
Kurtosis, u_3	3.3	3.3	2.9	2.9

Table 2.2: Flow statistics in the 2 & 3 directions (y and z) for each of the four turbulence levels in the Webster et al. [2004] "T-Box", including mean velocity, root mean square of the velocity fluctuations, ratio between them etc... Reprinted from Webster et al. [2004] (Table 3).

Turbulence Level	**1**	**2**	**3**	**4**
$\langle U_2 \rangle$ (cm/s)	0.10	0.04	-0.12	0.07
$\langle U_3 \rangle$ (cm/s)	-0.13	0.08	0.28	-0.10
$\langle u_{2_{rms}} \rangle$ (cm/s)	0.13	0.25	0.76	0.97
$\langle u_{3_{rms}} \rangle$ (cm/s)	0.15	0.29	0.76	0.96
$\langle u_{2_{rms}}/u_{3_{rms}} \rangle$	0.83	0.85	1.00	1.02
$\overline{(u_2' u_3')}$ (cm^2/s^2)	-0.006	-0.014	0.19	0.39
Skewness, u_2	0.5	0.1	0.0	-0.4
Skewness, u_3	-0.3	0.4	0.1	-0.2
Kurtosis, u_2	3.2	3.1	3.1	3.3
Kurtosis, u_3	2.6	3.2	2.8	3.0

Table 2.3: Mean dissipation rate of kinetic energy, Kolmogorov length scale, Taylor length scale, and Taylor-scale Reynolds number for each of the four turbulence levels in the Webster et al. [2004] "T-Box". Reprinted from Webster et al. [2004] (Table 4).

Turbulence Level	**1**	**2**	**3**	**4**
$\langle \epsilon \rangle$ (cm^2/s^3)	0.002	0.009	0.096	0.25
η (cm)	0.15	0.10	0.057	0.045
λ (cm)	0.93	1.15	0.90	0.73
Re_λ	10	32	65	68

As discussed in Webster et al. [2004] the parameters in Tables 2.1, 2.2, and 2.3 agree well with field studies of coastal zone and wind driven turbulence [Jimenez,

1997, Webster et al., 2004]. The dissipation rates of the turbulence levels in Table 2.3 compare favorably with studies by Granata and Dickey [1991] and Kiørboe and Saiz [1991], that estimate coastal zone dissipation rates in the range of 10^{-3} to 1 $\frac{cm^2}{s^3}$ [Webster et al., 2004]. The Kolmogorov length scales in Table 2.3 including of the turbulence levels were also in good agreement with those reported by Kiørboe and Saiz [1991] and Jimenez [1997], between 0.04 to 0.2 cm [Webster et al., 2004]. Lastly, the root mean square of the velocity fluctuations (u_{rms}) for the four turbulence levels (Tables 2.1 and 2.2) were in the range of the typical swim speed for marine copepods ($0.1\frac{cm}{s}$ to $1.0\frac{cm}{s}$) reported by Yamazaki and Squires [1996].

Because the turbulent parameter data of the T-Box is readily available, and the turbulence levels agree so well with coastal zone and wind driven turbulence [Webster et al., 2004], the vortex experiment outlined later in this thesis is intended to mimic the parameters of turbulence levels 2 and 3 of the Webster et al. [2004] T-Box device. These levels were selected because unpublished data collected by A. Brathwaite indicated that copepods exhibited the most drastic change in behavior between Turbulence Levels 2 and 3 of the T-Box.

2.3 The Burgers′ Vortex

Jumars et al. [2009] discusses two types of vortices that could be chosen as a cartoon to represent a single turbulence worm in isotropic turbulence: the Lundgren [1982] stretched spiral vortex and the Burgers [1948] vortex. They elect to use the Burgers′ vortex as the simplifying cartoon and justify the selection of the Burgers′ vortex because the Lundgren stretched spiral vortex decays asymptotically towards the Burgers′ vortex [Pullin and Saffman, 1998]. Furthermore, research by Hatakeyama and Kambe [1997] indicated that an ensemble of Burgers′ vortices with random size, orientation, and strength closely resembles DNS and laboratory measurements of the

longitudinal structure functions in isotropic turbulence *at dissipative scales*. In the situation of plankton-turbulence interaction, the critical scaling range is the dissipative range, which generally matches the size of plankton.

It is important to note that further research by He et al. [1999] indicated that, when using an ensemble of solely Burgers′ vortices, the transverse structure functions did not display the appropriate inertial range scaling. Velocity structure functions are the moments of the velocity difference between two points in space [Pope, 2000]. A longitudinal structure function is a particular subset of velocity structure function, in which the separation vector between the two points is in the same direction as the velocity components. Similarly, a transverse structure function is a velocity structure function in which the separation vector is transverse (perpendicular) to the velocity components.

2.3.1 Origins of the Burgers′ Vortex

The steady Burgers′ vortex was first presented in 1948 as a purely mathematical solution to the Navier-Stokes equations [Burgers, 1948]; a bit of a curiosity, as it did not "solve" any specific fluid mechanics issue of the day [Jumars et al., 2009]. It was not until much later, when research into the nature of isotropic turbulent flows through DNS made significant progress, that the significance of the Burgers′ vortex became apparent. The resulting equations for the three velocity components are given below (in cylindrical coordinates):

$$u_r = -ar \tag{2.13}$$

$$u_\theta = \frac{\Gamma}{2\pi r}\left[1 - e^{\left(\frac{-r^2 a}{2\nu}\right)}\right] \tag{2.14}$$

$$u_x = 2ax \tag{2.15}$$

In the above equations a is defined as a constant axial strain rate, Γ is the vortex circulation, and r is the radial distance from the Burgers′ vortex axis [Davidson, 2004]. Note that these equations are formulated slightly differently from those in Jumars et al. [2009]. In Equations 2.13, 2.14, and 2.15, a is equivalent to γ_{loc} and the x-axis is chosen as the axial coordinate direction, as opposed to the z-axis in Jumars et al. [2009]. In addition, Equation 12 in the Jumars et al. [2009] paper is incorrect - the expression for u_z is properly written $u_z = 2\gamma_{loc}z$ as per Davidson [2004]. In a Burgers′ vortex, the kinetic energy lost due to viscous dissipation is replaced by the energy related to the constant acceleration of the fluid along the vortex axis due to the strain rate, a, resulting in a steady state velocity field [Jumars et al., 2009]. Vorticity is also constant; as shown in the figure below - the outward diffusion of vorticity is in equilibrium with the inward advection of vorticity.

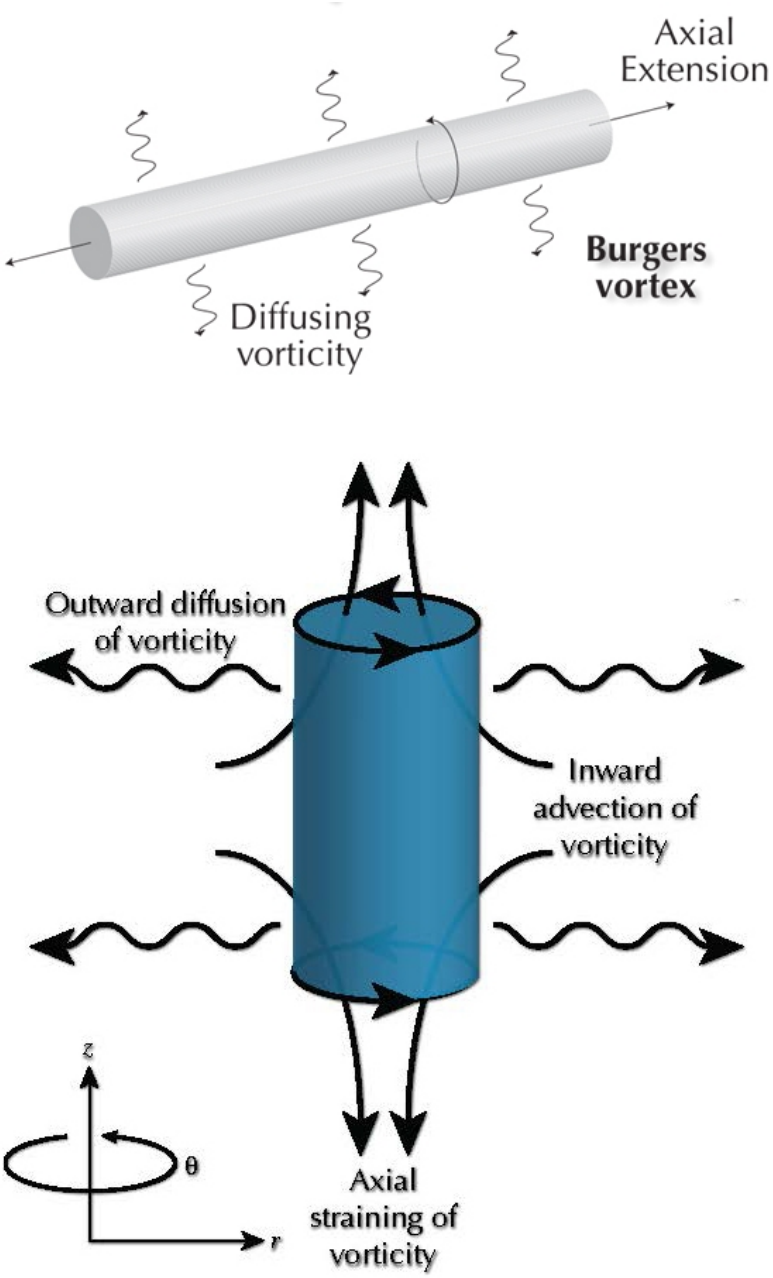

Figure 2.2: Cartoon of a steady state Burgers′ Vortex. Reproduced from Jumars et al. [2009].

2.3.2 Burgers′ Vortex Flow Field

This section varies the strain rate parameter, a, and the circulation, Γ, and compares the results to understand the effects on the vortex structure. With that goal in mind, this study graphically examines the effects these modifications have on transect plots of several key flow parameters of interest such as u_θ, u_x, the maximum principal strain rate (MPSR), $e_{r\theta}$, and ω_x.

A cursory examination of equations 2.13, 2.14, and 2.15 reveals that the Burgers′ vortex flow field is axisymmetric. As such, any flow parameter of interest will be a function of the radial and x positions only. As an example of this, consider the plots of $e_{r\theta}$ and ω_x in Figures 2.3 and 2.4.

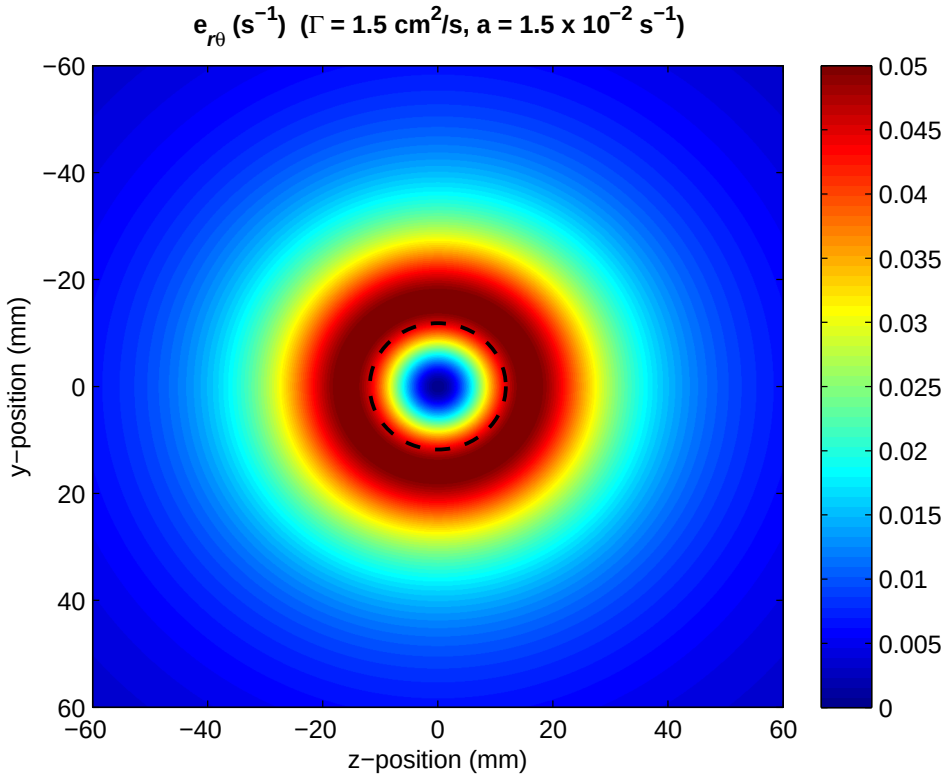

Figure 2.3: Isocontours of $e_{r\theta}$ on the $y-z$ (or $r-\theta$) plane.

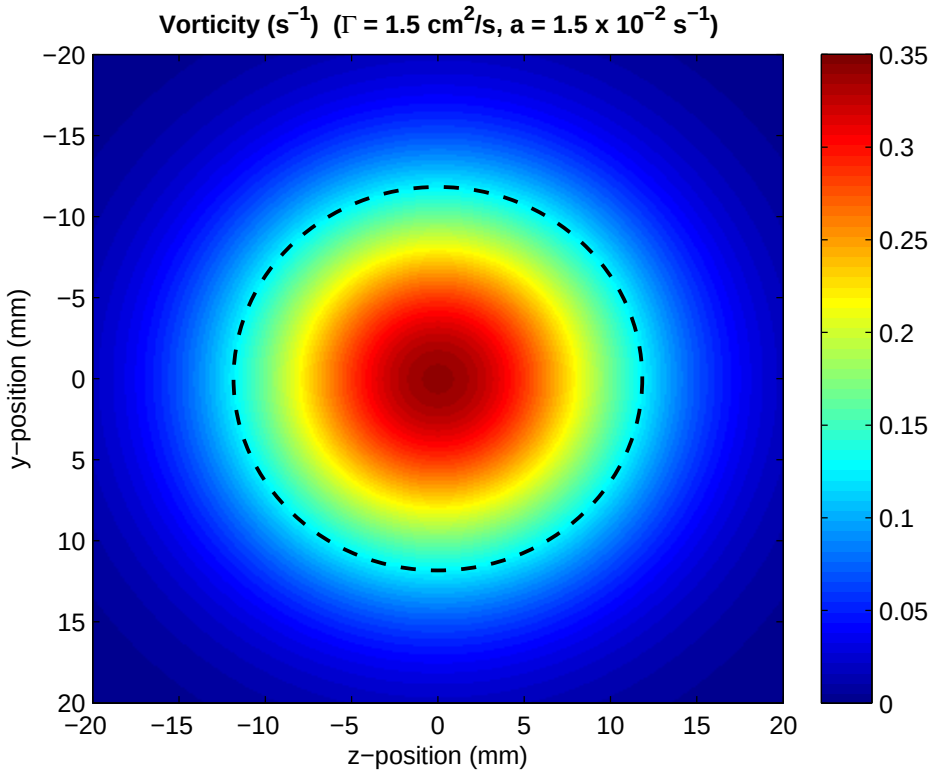

Figure 2.4: Isocontours of ω_x on the $y-z$ (or $r-\theta$) plane.

The dashed line in the two plots shown in Figures 2.3 and 2.4 refers to the radial position r_B, a measure of the characteristic vortex radius, defined as $r_B = \sqrt{\frac{2\nu}{a}}$.

To gain a better appreciation of the three-dimensionality of the flow, Figures 2.6 and 2.7 show two different viewing angles of the r and θ (y and z) components of the velocity vectors (located in the $r-\theta$ plane at the vortex centroid, $x=0$) and a single streamline. For clarity, Figure 2.5 shows the orientation of the viewing angles with respect to the Burgers′ vortex.

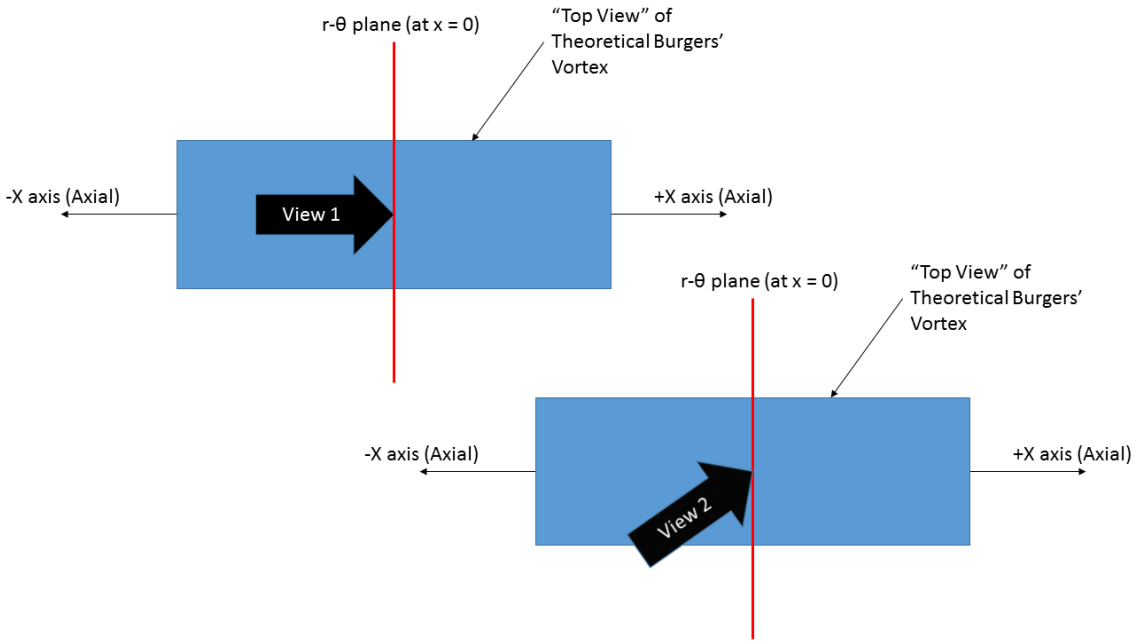

Figure 2.5: Orientation of the two viewing angles with respect to the Burgers′ vortex. View 1 corresponds to Figure 2.6 and View 2 corresponds to Figure 2.7.

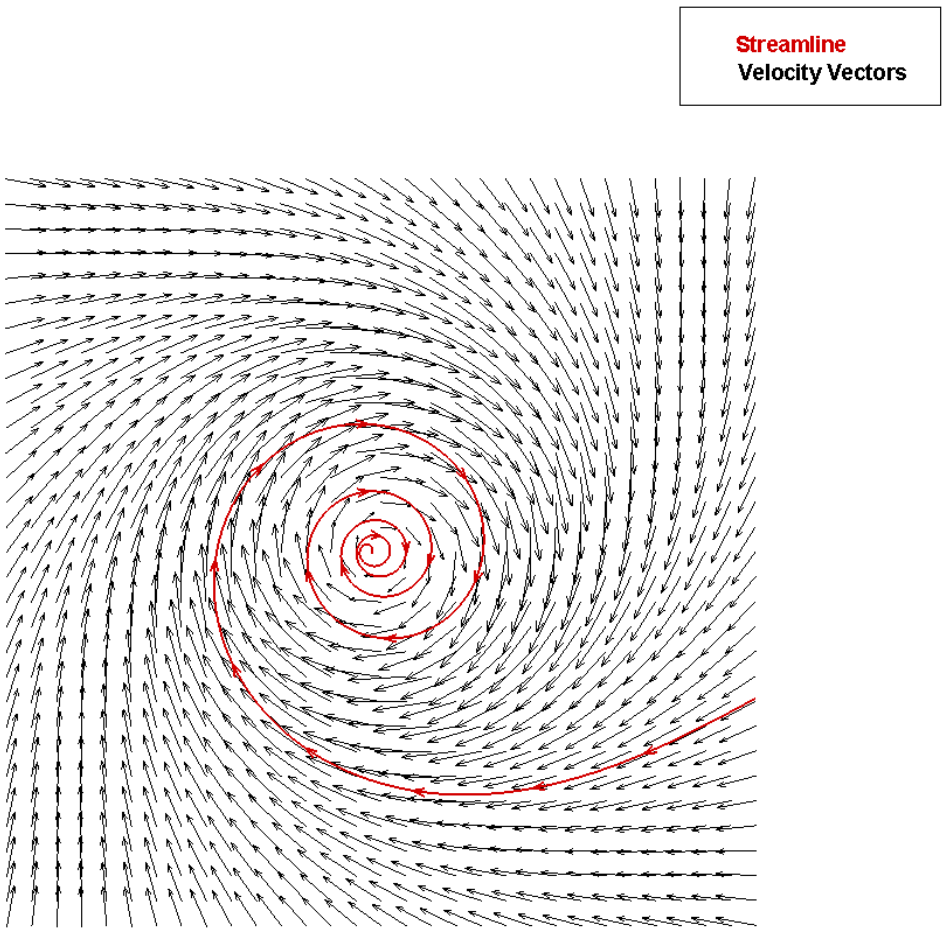

Figure 2.6: View 1 (see Figure 2.5) of the r and θ (y and z) components of the velocity vectors (black vectors) in the $r-\theta$ ($y-z$) plane at $x = 0$, and the shape of the three dimensional streamline from the perspective of View 1 (the red line with spaced arrows).

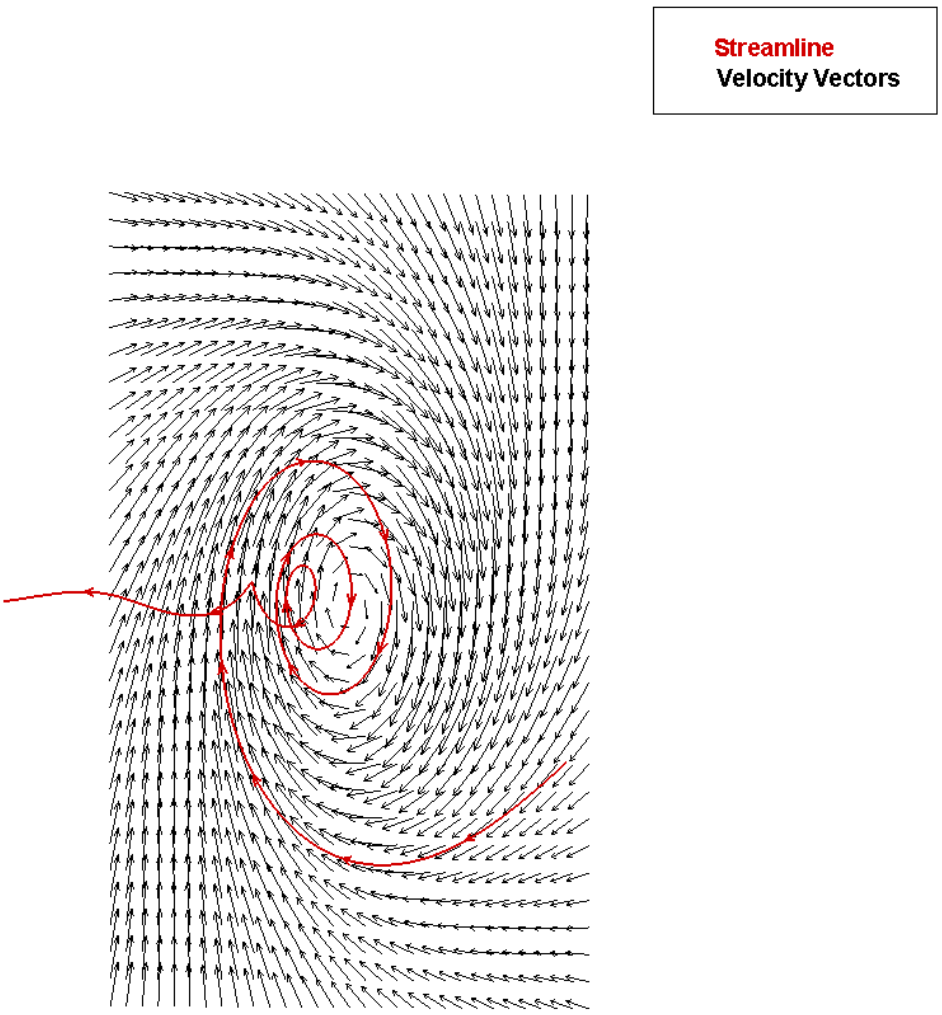

Figure 2.7: View 2 (see Figure 2.5) of the r and θ (y and z) components of the velocity vectors (black vectors) in the $r-\theta$ ($y-z$) plane at $x = 0$, and the shape of the three dimensional streamline from the perspective of View 2 (the red line with spaced arrows).

As a result of axi-symmetry, the most insightful plots of many these flow parameters are the plots as a function of radial position. u_θ, $e_{r\theta}$, and ω_x are easily defined as functions of r:

$$u_\theta = \frac{\Gamma}{2\pi r}\left[1 - e^{\left(\frac{-r^2 a}{2\nu}\right)}\right] \tag{2.16}$$

$$e_{r\theta} = \frac{\Gamma}{2\pi}\left[\left(\frac{a}{2\nu} + \frac{1}{r^2}\right)e^{\frac{-ar^2}{2\nu}} - \frac{1}{r^2}\right] \tag{2.17}$$

$$\omega_x = \frac{\Gamma a}{2\pi\nu}e^{\frac{-ar^2}{2\nu}} \tag{2.18}$$

In addition, the maximum principal strain rate (MPSR) is computed numerically as a function of r.

The axial velocity (u_x) is a function of position along the vortex axis (x) only:

$$u_x = 2ax \tag{2.19}$$

2.3.2.1 Discussion of Theoretical u_θ Profiles

Regardless of the values of a and Γ, the shape of the u_θ profiles share some common characteristics. As shown in Figures 2.8 and 2.9, u_θ rapidly increases from zero on the vortex centerline and approaches its peak value at a radial distance slightly larger than r_B. u_θ decays to zero as r approaches infinity, albeit more gradually than it approaches $u_{\theta_{max}}$ near the vortex core.

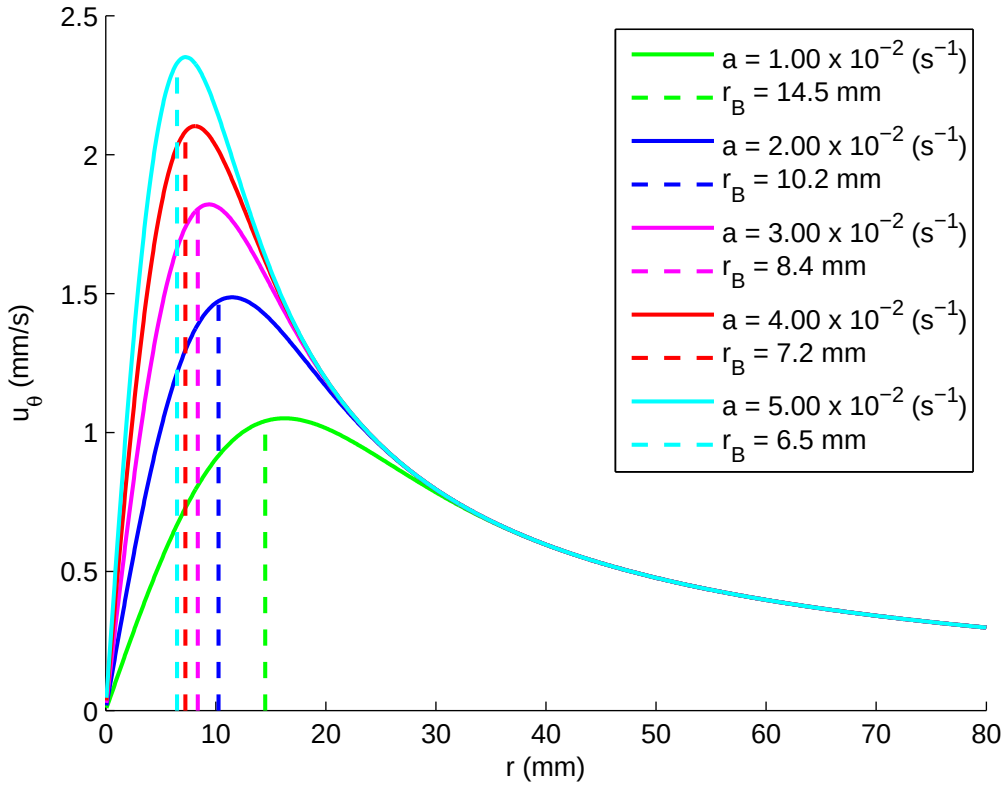

Figure 2.8: Profiles of u_θ with varying strain rate parameter, a. The value of Γ is 1.5 $cm^2 s^{-1}$.

Variation in the axial strain rate parameter, a, have several noticeable effects. As illustrated by Figure 2.8, increasing a increases the maximum value of u_θ. In addition, increases to a also shift the location of maximum u_θ (and r_B) in towards the vortex centerline ($r = 0$). The last effect of note in Figure 2.8 is, regardless of the value of a, the plots collapse to the same profile on the downslope (after the profile reaches $u_{\theta_{max}}$).

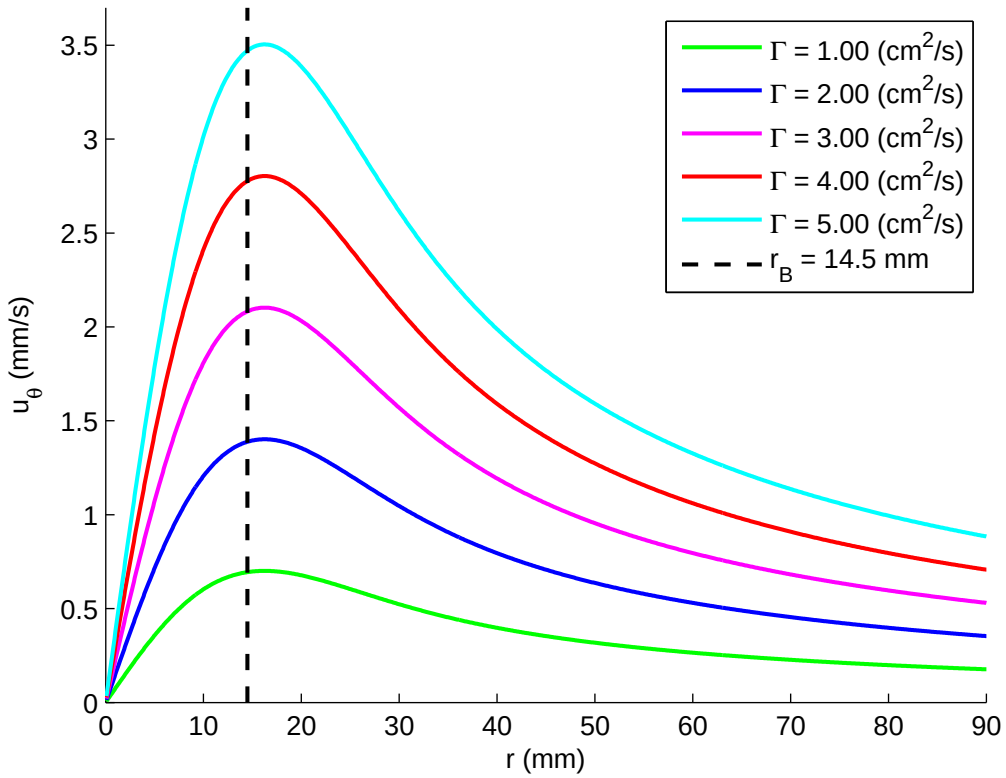

Figure 2.9: Profiles of u_θ with varying circulation, Γ. The value of a is $1 \times 10^{-2}\ s^{-1}$.

As shown in Figure 2.9, increasing the circulation, Γ, results in an increase in maximum u_θ, but the location of the peak and r_B do not vary. In addition, whereas the plots of u_θ with changing a collapsed to the same profile on the outer part of the profile, the plots of u_θ with varying Γ do not exhibit a similar collapse. Each profile approaches zero as r approaches infinity, but the profiles are still distinct 10 cm from the vortex centerline.

2.3.2.2 Discussion of Theoretical Axial Velocity Profiles

Profiles of u_x are straight lines, with the slope varying only on the value of the strain rate parameter, a (see Figures 2.10 and 2.11). The line passes through zero at the midpoint of the vortex axis (i.e., $x = 0$). From Figure 2.11, it is clear the value

of the circulation, Γ, has no effect on the u_x profile.

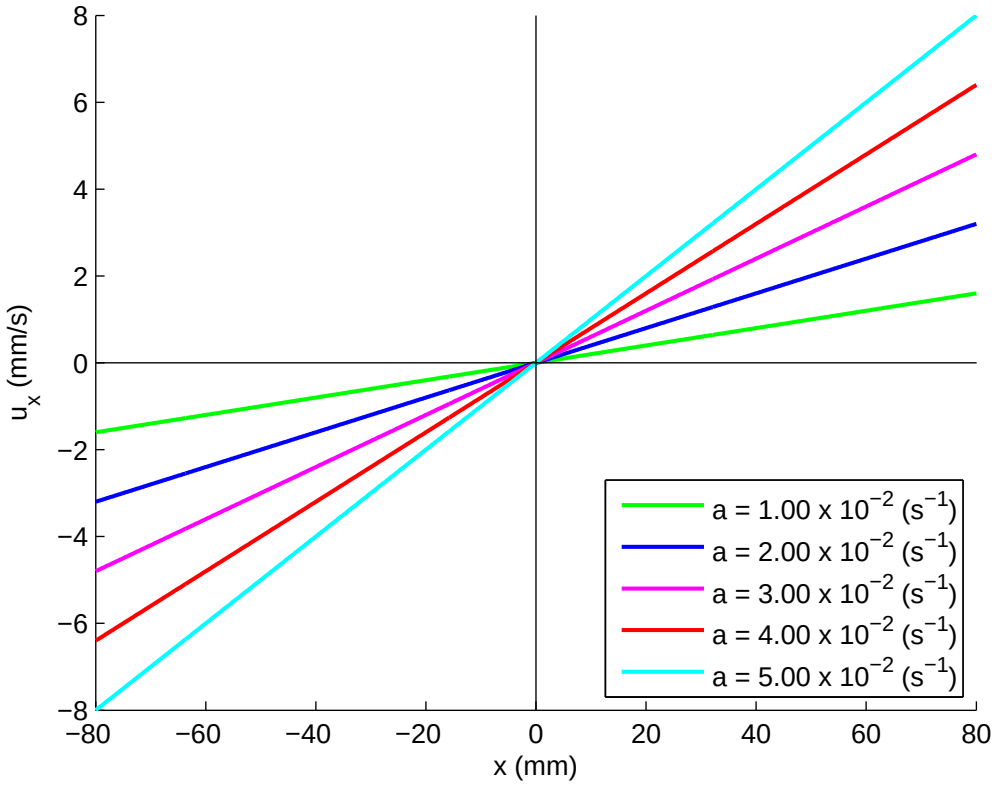

Figure 2.10: Profiles of u_x with varying axial strain rate parameter, a. The value of Γ is 1.5 $cm^2 s^{-1}$.

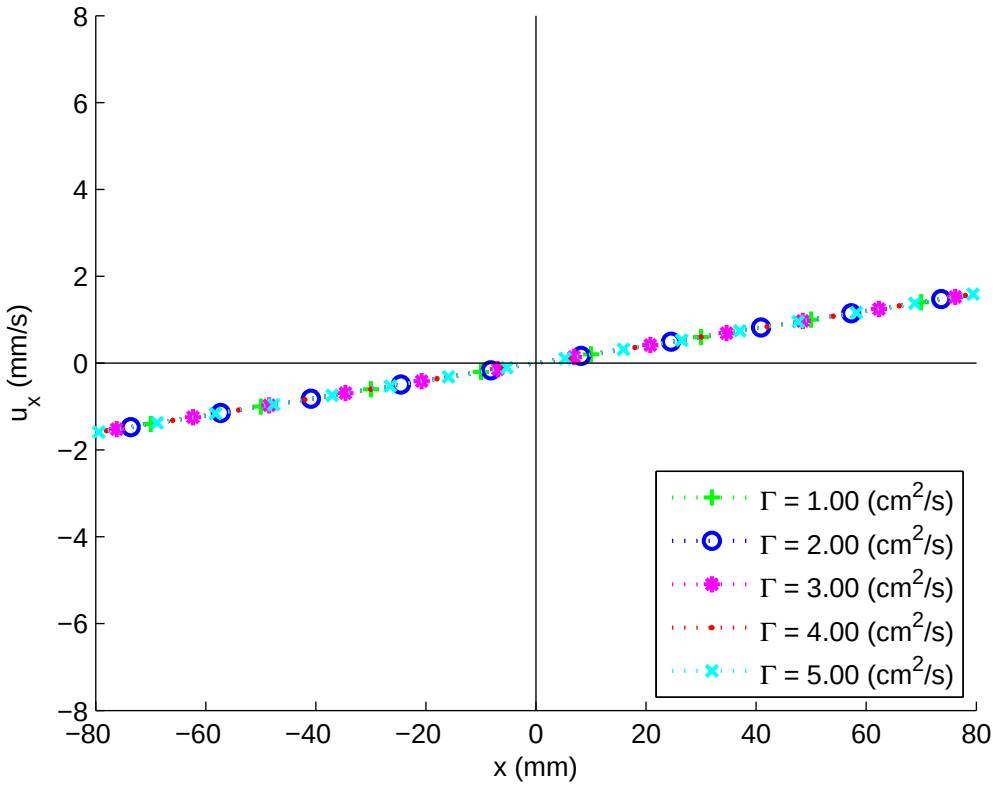

Figure 2.11: Profiles of u_x with varying circulation, Γ. The value of a is 1×10^{-2} s^{-1}.

2.3.2.3 Discussion of Theoretical Strain Rate Profiles

All maximum principal strain rate (MPSR) profiles start at a value of $2a$ (at the vortex centerline, $r = 0$). The profiles are flat at $2a$ near the centerline, then rapidly increases to the maximum MPSR, which occurs at a radial position slightly larger than r_B (also larger than the radial position corresponding to maximum u_θ). After reaching the peak value of MPSR, all profiles decrease back to the constant value of $2a$ and stay at that constant value as r approaches infinity (See Figures 2.12 and 2.13).

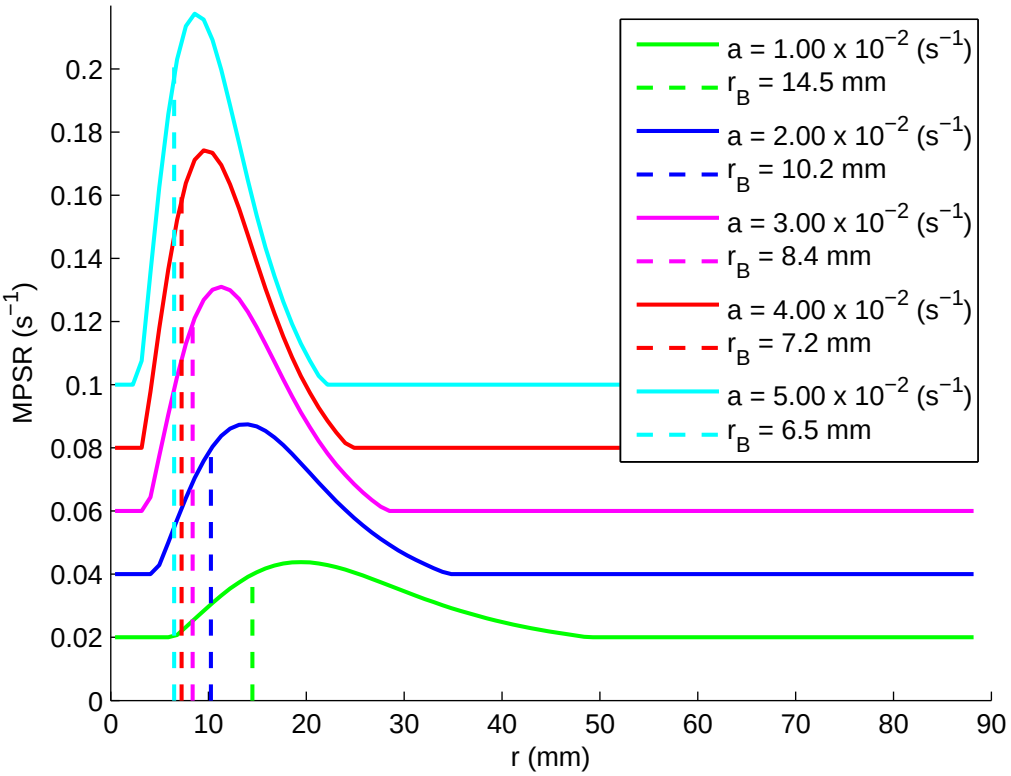

Figure 2.12: Profiles of MPSR with varying axial strain rate parameter, a. The value of Γ is 1.5 $cm^2 s^{-1}$.

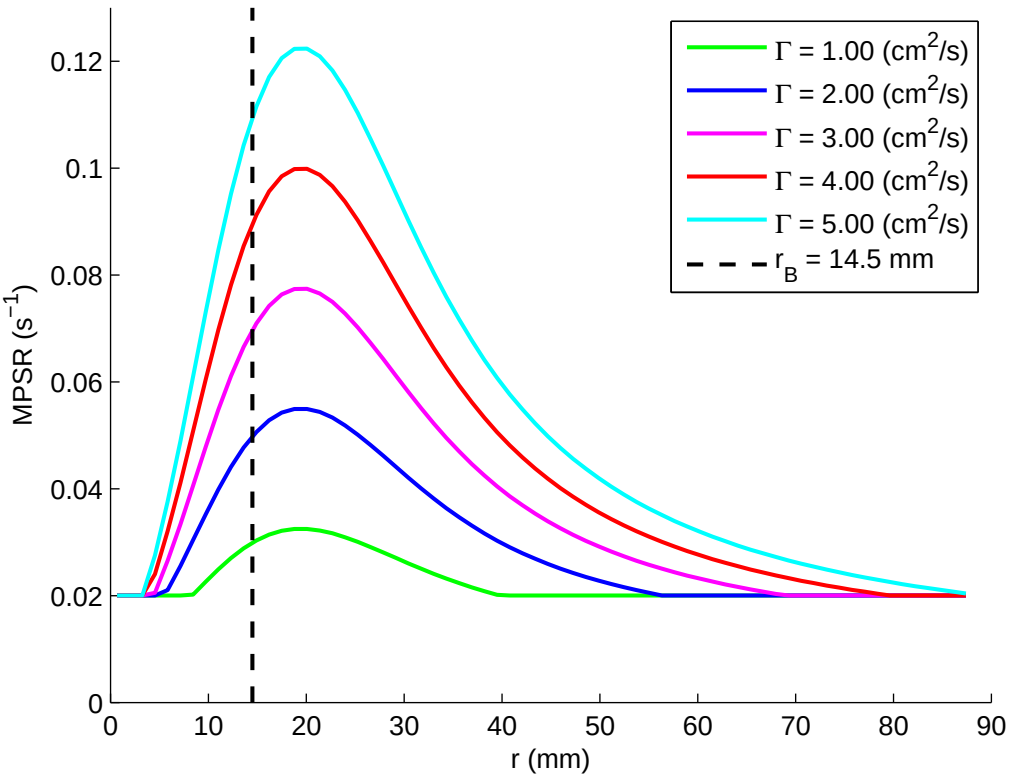

Figure 2.13: Profiles of MPSR with varying circulation, Γ. The value of a is 1×10^{-2} s^{-1}.

Increasing the strain rate parameter, a, increases the maximum MPSR and shifts the location of the maximum MPSR towards the vortex centerline, very similar to the effect of increasing a on the u_θ profiles. Increasing a also has the apparent effect of increasing the steepness of the profile, both approaching and leaving the maximum MPSR.

Similar to the effects of circulation on the u_θ profiles, increasing the circulation, Γ, increases the maximum MPSR, but does not alter the position that the maximum MPSR occurs. In addition, increasing Γ does not appear to affect the steepness of the peak as drastically as increasing the axial strain rate parameter, a.

The maximum principal strain rate is the best indicator of the maximum strain

rate experienced by a fluid element, as it is independent of the coordinate system chosen. However, in the case of the theoretical Burgers′ vortex, much of the interesting behavior of the MPSR profiles, particularly the location and shape of the peak, are the result of changes in $e_{r\theta}$. In fact, $e_{r\theta}$ is the only component of the strain rate tensor that is a function of radial position. As such, it is instructive to examine profiles of $e_{r\theta}$ directly.

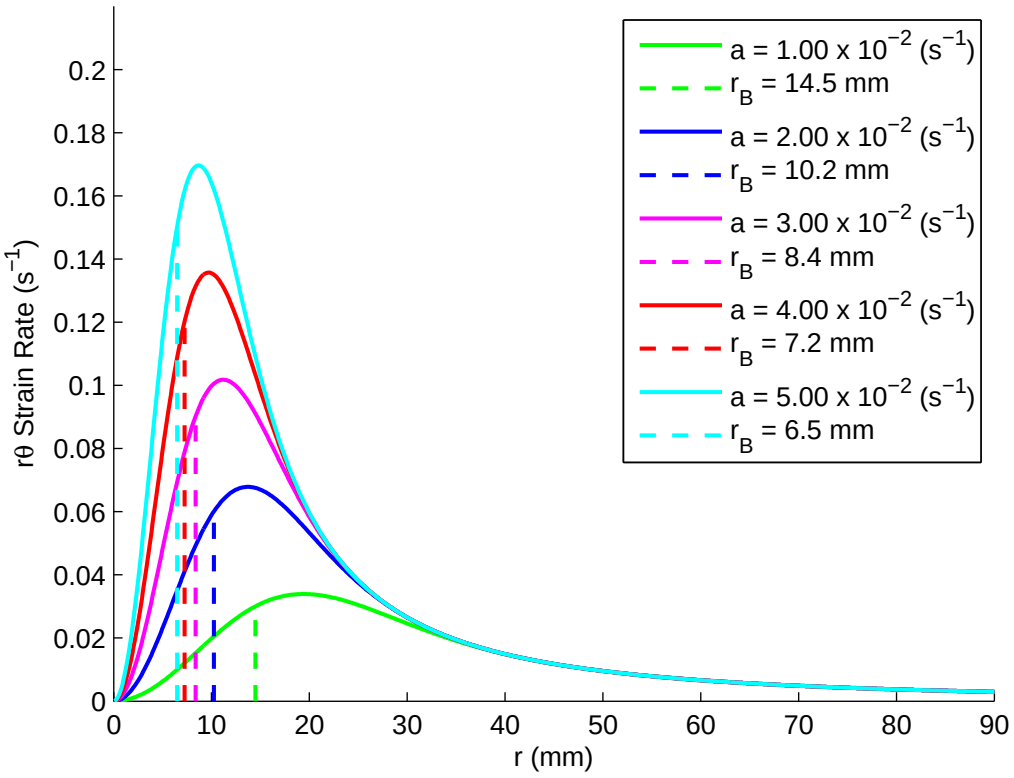

Figure 2.14: Profiles of $e_{r\theta}$ with varying axial strain rate parameter, a. The value of Γ is 1.5 $cm^2 s^{-1}$.

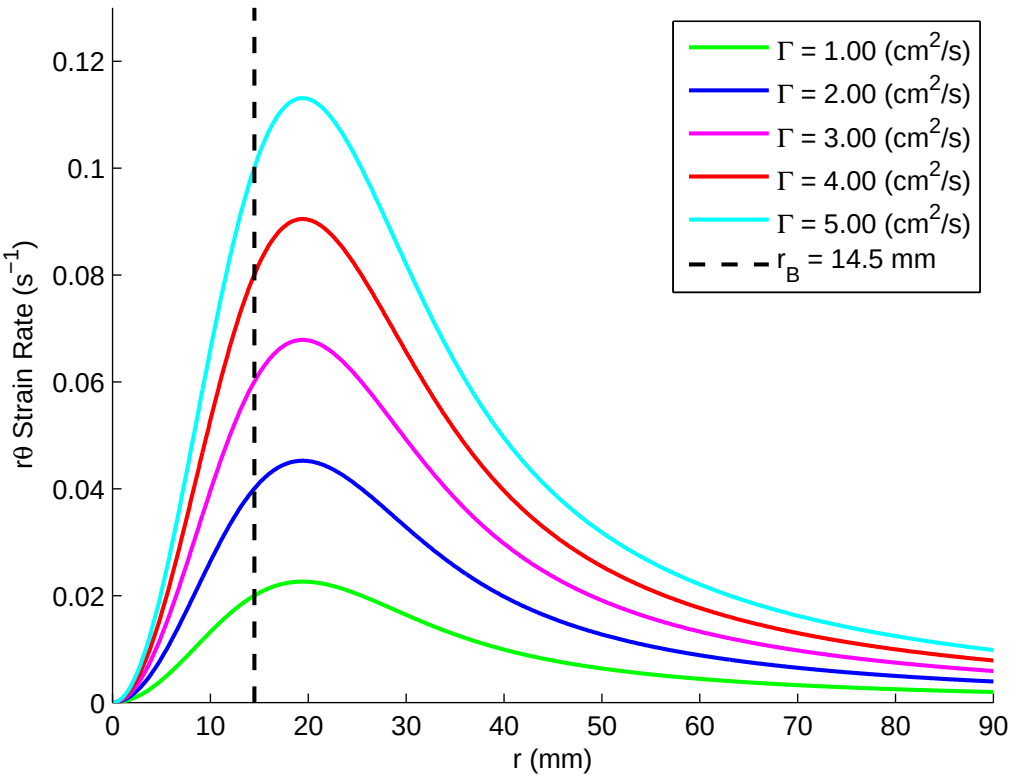

Figure 2.15: Profiles of $e_{r\theta}$ with varying circulation, Γ. The value of a is 1×10^{-2} s^{-1}.

The profiles of $e_{r\theta}$ are quite alike in appearance to the profiles of u_θ in section 2.3.2.1. The profiles start at zero at the vortex centerline, increase to the maximum value of $e_{r\theta}$, then decrease more gradually back to zero as r approaches infinity. The $e_{r\theta}$ peak occurs at a greater radial distance from the vortex centerline than the u_θ peak. Similarly by comparing Figures 2.14 and 2.15 to Figures 2.12 and 2.13, the effects of $e_{r\theta}$ on MPSR are clearly evident. The peak MPSR occurs at the exact location of peak $e_{r\theta}$, indicating that the local peak in $e_{r\theta}$ is responsible for the increase in MPSR.

As with MPSR and u_θ, increasing a increases the maximum $e_{r\theta}$ and shifts the location of maximum $e_{r\theta}$ towards the vortex centerline. It is also clear from Figures

2.14 and 2.15 that the apparent steepening of the MPSR peak with increasing a is due to the steepening of the $e_{r\theta}$ peak. This is a result of the maximum $e_{r\theta}$ being higher for higher values of a, but the width of the peak remaining nearly constant as a increases, necessitating larger slopes. As with the plots of u_θ, regardless of the value of a, the plots of $e_{r\theta}$ collapse to the same profile as r increases past the radius of maximum $e_{r\theta}$.

Increasing the circulation, Γ, increases the maximum $e_{r\theta}$, but does not alter the radial position of the peak. Unlike the profiles of $e_{r\theta}$ with changing a, profiles of $e_{r\theta}$ with changing Γ do not collapse to a single profile after reaching the peak value. Like the profiles of u_θ with changing Γ, the profiles of $e_{r\theta}$ with changing Γ remain distinct up to 10 cm away from the vortex centerline, although the profiles all approach zero as r goes to infinity.

2.3.2.4 Discussion of Theoretical Vorticity Profiles

Some commonalities of the profiles of vorticity are evident in Figures 2.16 and 2.17. The vorticity plots are similar in form to the right half of a normal distribution, with varying amplitude and variance. As such, regardless of the values of a and Γ, the vorticity is maximum on the vortex centerline (at $r = 0$) and decreases asymptotically to zero as r approaches infinity. Interestingly, the vorticity plots approach zero substantially faster than the plots of u_θ or $e_{r\theta}$ for the same range of a and Γ values.

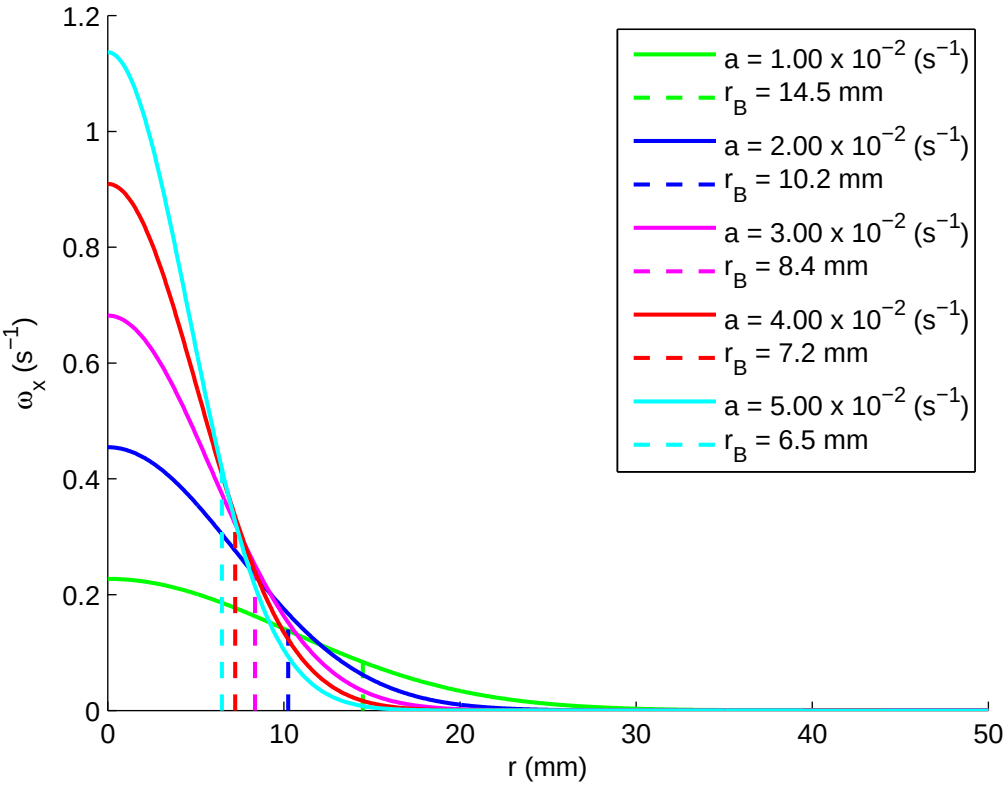

Figure 2.16: Profiles of vorticity with changing axial strain rate parameter, a. The value of Γ is 1.5 $cm^2 s^{-1}$.

As shown in Figure 2.16, increasing the axial strain rate parameter, a, has two noticeable effects. First, it results in higher maximum vorticity (still on the vortex centerline). Second, it results in faster decrease, i.e. the vorticity approaches zero faster at higher values of a. This is noticeably different from the behavior of the u_θ and $e_{r\theta}$ plots, in which increasing a shifted the location of the peak and the profiles collapsed to a single profile as r increased (above the r of maximum u_θ or $e_{r\theta}$).

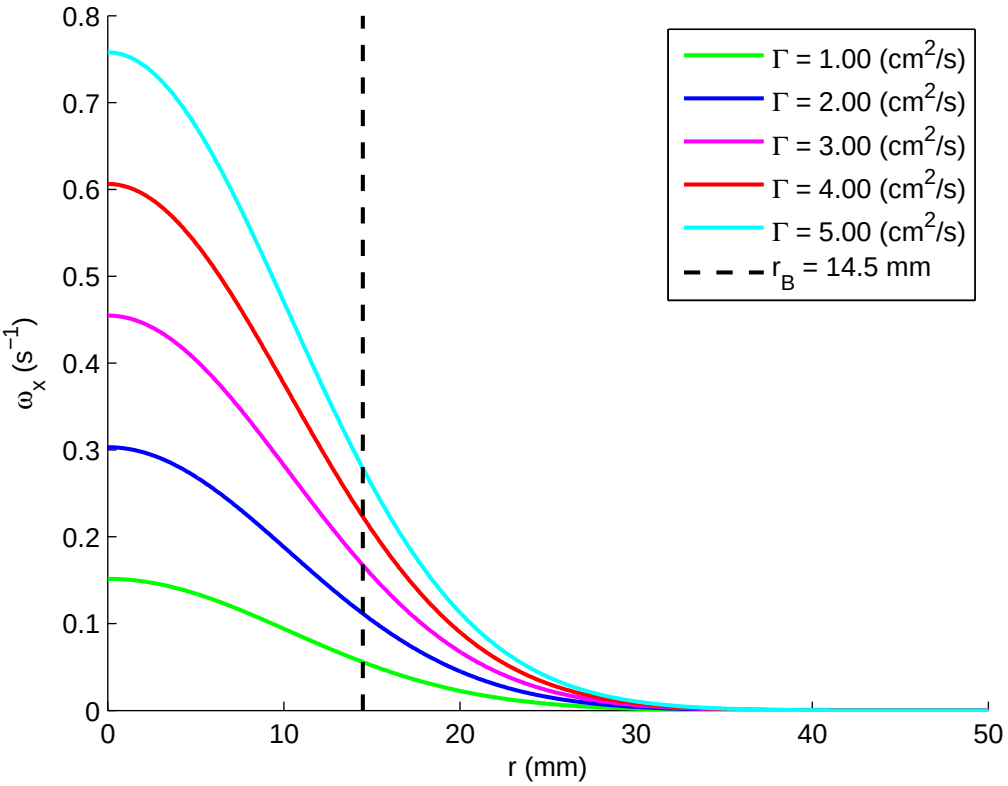

Figure 2.17: Profiles of vorticity with varying circulation, Γ. The value of a is $1 \times 10^{-2}\ s^{-1}$.

Increasing the circulation, Γ, increases the maximum vorticity. Beyond $r = 30$ mm, the vorticity is very close to zero for all of the profiles.

2.3.3 Parameter Estimation

To create a Burgers′ vortex that mimics the characteristics of coastal zone turbulence, the vortex parameters of r_B (vortex radius), a, and Γ must be estimated. As put forth in Gargett [1997], one must discover the size of the turbulent eddies that account for the most dissipation, and use that size as an estimate for the cartoon Burgers′ vortex radius r_B [Jumars et al., 2009]. To that end, Jumars et al. [2009]

take the derivative of the viscous dissipation rate of kinetic energy with respect to the wavenumber (k). The equation for the viscous dissipation rate of kinetic energy as a function of wavelength is given below [Tennekes and Lumley, 1972]:

$$\epsilon_\nu(k) = 2\alpha\nu\bar{\epsilon}^{\frac{2}{3}}k^{\frac{1}{3}}e^{\left[-\frac{3}{2}\alpha(k\eta)^{\frac{4}{3}}\right]} \tag{2.20}$$

In the above equation α is the Kolmogorov constant, which has a value of 1.64 based upon DNS experiments [Gotoh et al., 2002], η is the Kolmogorov length scale, ν is the kinematic viscosity, $\bar{\epsilon}$ is the dissipation rate (with the overbar indicating the mean, as before). To solve for the wavenumber (k) at which maximum dissipation occurs, Jumars et al. [2009] take the derivative of equation 2.20 and set it equal to zero. The wavenumber for which dissipation rate is maximum (k_d) is found to be $k_d = \frac{0.18}{\eta}$ [Jumars et al., 2009]. The turbulent eddy size, l, is defined as being roughly equal to $\frac{2\pi}{k}$ [Tennekes and Lumley, 1972]. Thus, to ensure that the vortex diameter is of the same size as the desired turbulent eddy (i.e. $d \approx l$), Jumars et al. [2009] rearrange the expression for the turbulent eddy size, l, to $k = \frac{2\pi}{l}$ then sets this expression for k equal to the maximum dissipation wavenumber k_d (i.e $k = k_d = \frac{2\pi}{d} = \frac{0.18}{\eta}$) [Jumars et al., 2009]. Solving this for d in terms of η, one estimate of the diameter (and the corresponding radius) of the vortex is found to be [Jumars et al., 2009]:

$$d = 11\pi\eta \tag{2.21}$$

$$r = 17.5\eta \tag{2.22}$$

It is important to note that k_d is not the *only* wavenumber at which dissipation

occurs, simply the wavenumber at which dissipation is *maximum* (Figure 2.18).

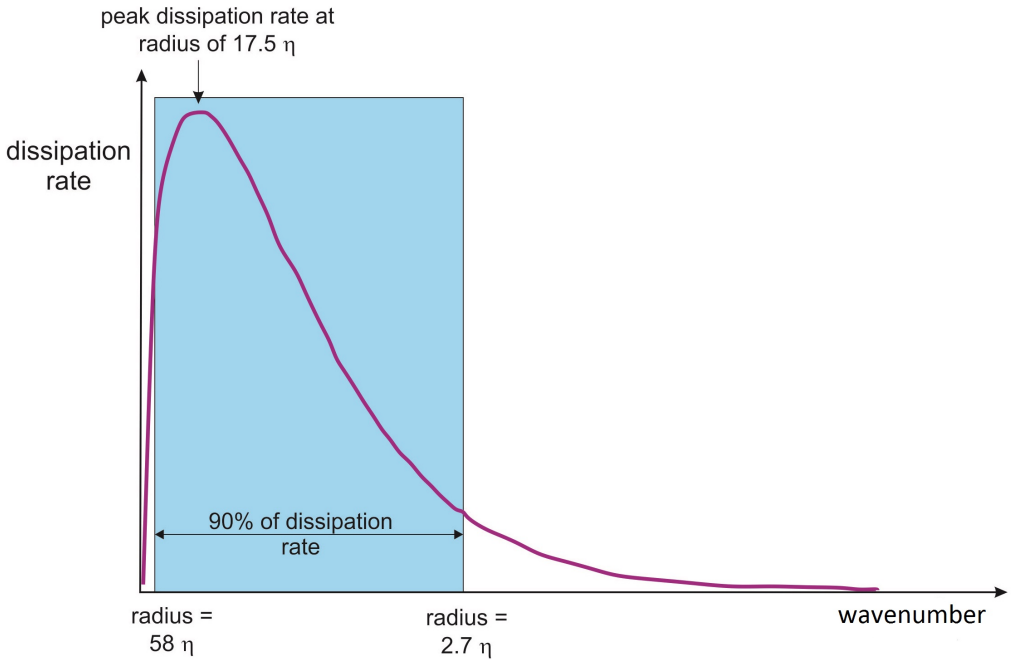

Figure 2.18: Dissipation rate plotted as a function of the wavenumber. 90 % of the total dissipation rate occurs in the range indicated. The scale at which the peak dissipation rate occurs is also noted.

As shown in Figure 2.18, the radius of peak dissipation rate does not give a proper estimate of a "typical" radius at which dissipation occurs [Jumars et al., 2009]. Jumars et al. [2009] also mention that the median wavelength (i.e. wavelength at which one half the dissipation occurs above that wavelength, and one half occurs below) is approximately equal to 8.1η. Thus, to estimate the characteristic Burgers′ vortex radius r_B, Jumars et al. [2009] elect to set it equal to the median wavelength, 8.1η, rather than the wavelength of maximum dissipation, 17.5η, judging the wavelength of median viscous dissipation to be a more representative estimate (note that He et al. [1999] estimates the wavelength of median dissipation to be 7.1η based upon analysis of the distribution of vortex Reynolds numbers, Re_Γ):

$$r_B = 8.1\eta \tag{2.23}$$

To estimate the axial strain rate parameter, a, Jumars et al. [2009] look to an equation in Davidson [2004], shown below, that gives the required axial strain rate in terms of the characteristic Burgers′ vortex radius r_B, already calculated from the above reasoning [Davidson, 2004]:

$$a = \frac{2\nu}{r_B^2} \tag{2.24}$$

Jumars et al. [2009] utilize a lengthy process to determine the circulation parameter (Γ) - a process made much simpler if one has access to target turbulent flow u_{rms} data (such as the data from turbulence levels in the Webster et al. [2004] T-Box experiments). Jumars et al. [2009] point to an equation put forth in Hatakeyama and Kambe [1997], which gives the value of Burgers′ vortex circulation (Γ) in terms of the root mean square of the velocity fluctuations (u_{rms}) and the characteristic Burgers′ vortex radius (r_B), shown below [Hatakeyama and Kambe, 1997, Jumars et al., 2009]:

$$\Gamma = 2\pi r_B u_{rms} \tag{2.25}$$

The above equation is assumed to hold true for isotropic turbulence [Hatakeyama and Kambe, 1997]. They justify it as a reasonable estimate for the circulation through the following reasoning. Using the equation above to estimate the circulation, one can

use it to form the vortex Reynolds number, shown below [Hatakeyama and Kambe, 1997]:

$$Re_\Gamma = \frac{\Gamma}{\nu} \tag{2.26}$$

This relationship can be combined with the Taylor scale Reynolds number, Re_λ, to form the fraction $\frac{Re_\Gamma}{\sqrt{Re_\lambda}}$. Using the estimate of circulation assumed by Hatakeyama and Kambe [1997] (Equation 2.25), one can show that this fraction is equivalent to 4π, which is very similar to the value for the same fraction obtained through DNS experiments by Jimenez et al. [1993]. As a result of this relationship, Hatakeyama and Kambe [1997], and later Jumars et al. [2009], claim that the Hatakeyama and Kambe [1997] relationship for estimating the Burgers′ vortex circulation, Γ, is reasonable.

Jumars et al. [2009] further discuss a procedure to estimate the root mean square of the velocity fluctuations (u_{rms}) to enable the use of equation 2.25. For this thesis, those procedures are unnecessary, as the u_{rms} values for the two turbulence levels we are attempting to reproduce with the Burge′s vortex apparatus are already published in Webster et al. [2004], shown in Tables 2.1 and 2.2.

CHAPTER III

METHODS

A device capable of creating a steady state Burgers′ vortex was designed and created. The Burgers′ vortex apparatus was designed to mimic the characteristics of a vortex potentially encountered in coastal zone turbulence. The device was calibrated with tomographic particle image velocimetry (Tomo-PIV) analysis of the generated vortex flow field. The Tomo-PIV analysis provided a full three dimensional velocity vector field and verified that the vortex produced by the apparatus has the desired characteristics. Behavioral assays at both turbulence levels were conducted on *Acartia tonsa* (Figure 3.1). Copepod behavior is compared to local hydrodynamics parameters such as strain rate and vorticity:

Figure 3.1: Picture of *Acartia tonsa*, image downloaded from http://www.3dmatt.com.

3.1 Experimental Design

The design of the experimental apparatus outlined herein follows the concept of a proposed vortex generation device put forth in Manneville et al. [2000] describing an acoustic technique to measure vortex characteristics. Manneville et al. [2000] generates this vortex using two co-rotating disks, rotating at identical speeds, which face each other with some separation distance between them. Each disk has a small hole in the center, out of which fluid flows due to the head difference between the vortex tank and the "drain" tank. The vortex is generated between the disks, and has the characteristic vortex stretching associated with the Burgers′ vortex. Figure 3.2 details the key components of the experimental set up:

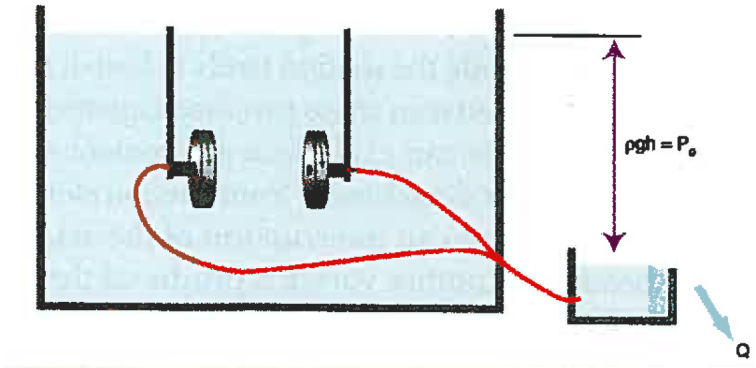

Figure 3.2: Schematic illustrating key components of Burgers′ vortex apparatus. Reprinted from Petitjeans [2003].

Neither Manneville et al. [2000] nor Petitjeans [2003] provide any quantitative data on the velocity field generated by this device. Based on the fluid visualization images provided in Figure 3.3 it was assumed that the apparatus could approximate the desired features of the Burgers′ vortex - an assumption later validated by Tomo - PIV experiments. Two aspects of the way the vortex is generated made the Burgers′ vortex model assumption probable. First, fluid rotation is generated by disk motion, providing an inducement mimicking the effects of circulation, Γ, in the list of Burgers′

vortex parameters discussed in Section 2.3. Second, withdrawing fluid out through the center of each disk provides a mechanism for the axial-straining-of-vorticity characteristic of a Burgers′ vortex.

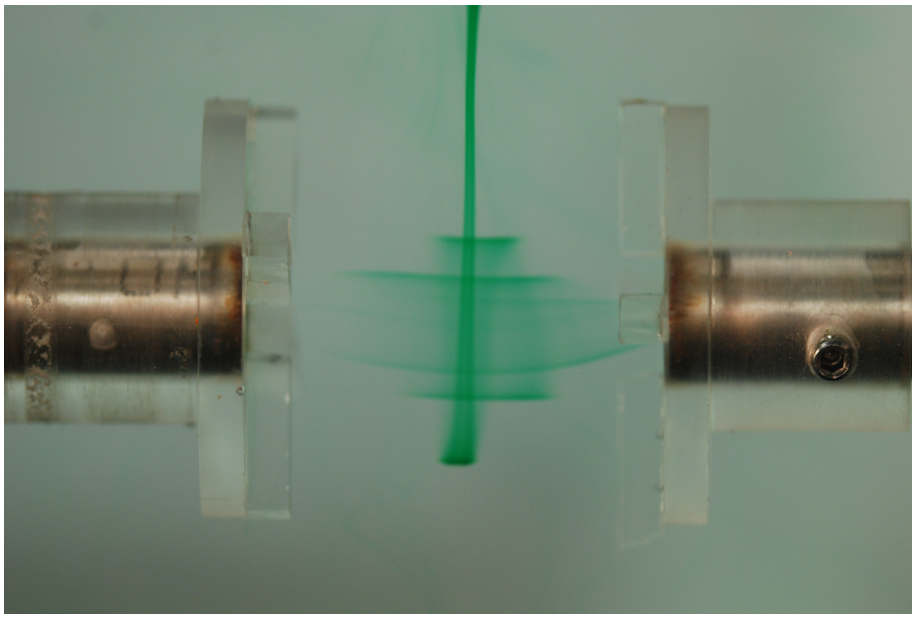

Figure 3.3: Dye flow visualization of a "T-Level" 3 Burgers′ vortex.

3.1.1 The Burgers′ Vortex Apparatus

The schematic detailing the resulting device, dubbed the Burgers′ vortex apparatus, is shown in Figure 3.4.

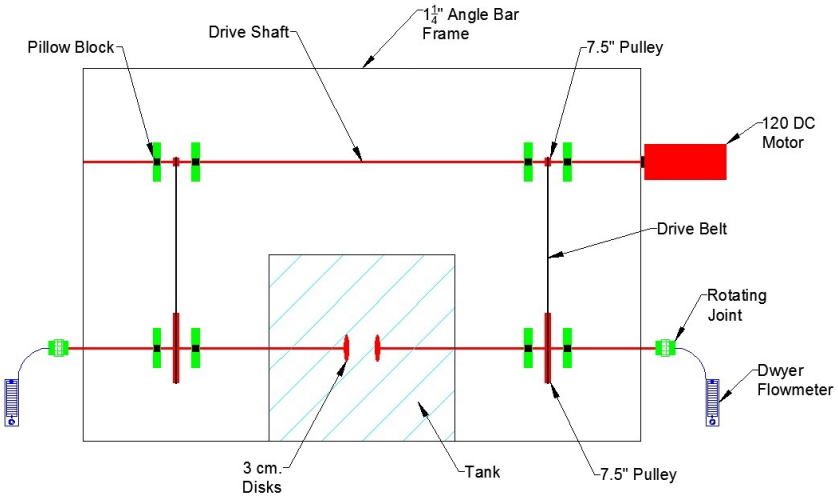

Figure 3.4: Schematic illustrating the key components of the Burgers′ vortex apparatus

The Burgers′ vortex apparatus consists of several key components. The tank in which the vortex is generated is constructed from 9.5 mm acrylic sheets, with outer dimensions of 20.64 cm (W) $\times$ 20.64 cm (L) $\times$ 27.31 cm (H). The location where the vortex is generated (i.e. the region between the two rotating disks) is centrally located with respect to the tank cross section, 15.24 cm above the bottom of the tank. The rotating disks, 3 cm in diameter, are fashioned out of acrylic. Each disk has a $\frac{3}{8}$ $in.$ hole drilled through the center, to accommodate the drive shaft. The four acrylic "paddles", spaced at 90° intervals along the face of each disk, are affixed to the disk face with acrylic cement. The paddles have a 0.25 $cm.$ square cross section and extend from the drive shaft hole to the edge of the disk (see Figure 3.5). The space between the paddles of the two disks is 2.4 $cm.$ A 9.5 mm hollow stainless steel rod with an inner diameter of 6.2 mm serves as the drive shaft for each disk. A 6.4 mm $6-32$ thread set screw secures each disk to the drive shaft.

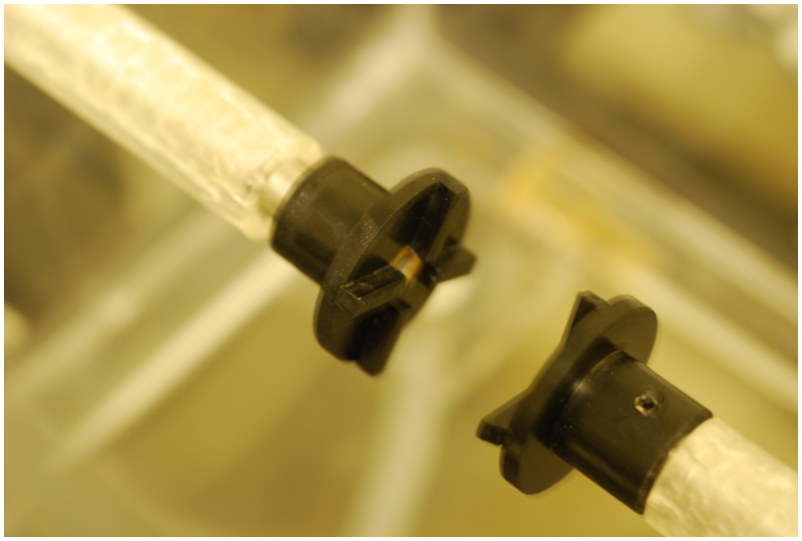

Figure 3.5: Photograph of the two disks affixed to the drive shafts in the Burgers′ vortex apparatus.

For each of the two disks, the drive shaft extends from the disk to the wall of the tank, through an o-ring pipe seal on the outside face of the tank wall(to prevent excessive leaking) and is inserted into two aluminum pillow blocks (designed to accommodate 9.5 mm shafts) for support (See Figures 3.6, 3.7, and 3.8). An acrylic base plate, affixed to the walls of the tank with $\frac{1}{4} - 20$ machine screws, maintains constant pressure on the pipe seal. Stop collars are installed on either side of the pillow blocks to avoid axial translation of the drive shaft. Each disk drive shaft is affixed with a 19.10 cm pulley, installed with three 6.4 mm $6 - 32$ thread set screws, centrally located between the two pillow blocks. The last component attached to each of the tank drive shafts is a rotating polybutylene tube fitting adapter. This component is a rotating hollow joint, one end of which slides onto the rotating tank drive shaft, while the other is affixed to stationary 9.5 mm plastic tubing (see Figures 3.6 and 3.7).

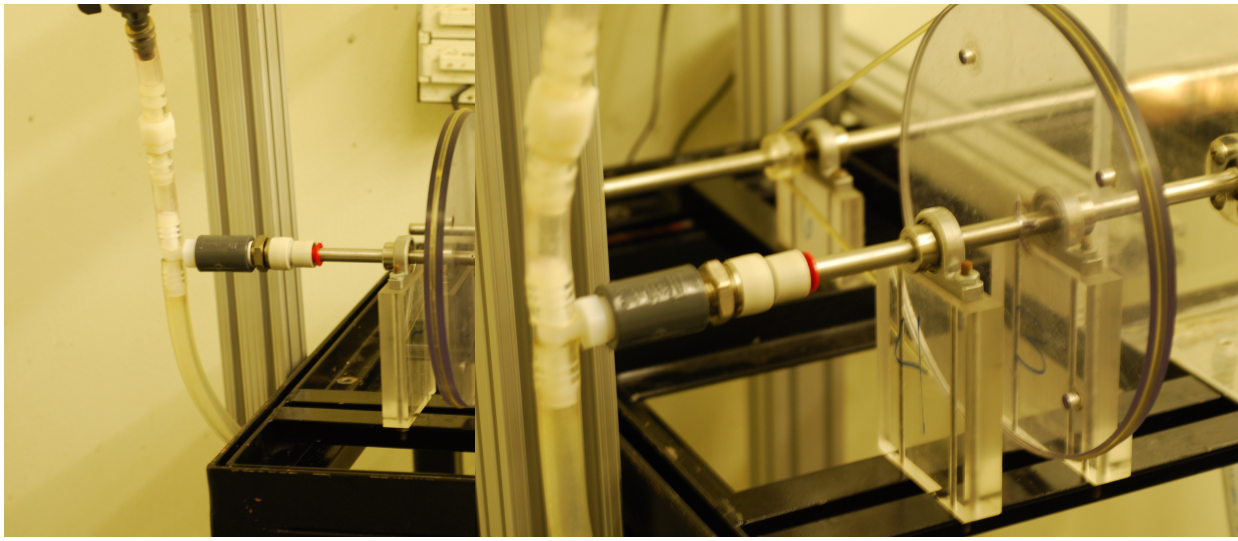

Figure 3.6: Front view of the left-hand-side drive shaft.

Figure 3.7: Side view of the left-hand-side drive shaft.

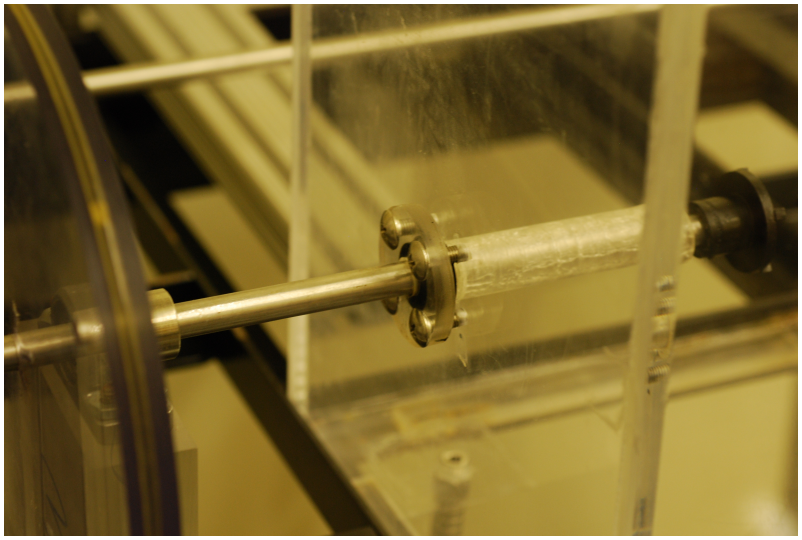

Figure 3.8: Close up of the shaft seal.

The plastic tubing leads to a flowmeter (Dwyer Instruments, Inc. - Model VFB-82-SSV), allowing the control of the outflow from each of the two disk holes individually. Downstream of the flowmeter, the tubing leads to the drain tank.

Two 73.66 *cm* o-rings (3.2 *mm* cross-section diameter) serve as drive belts for the tank drive shafts. These o-rings connect to the two 19.10 *cm* pulleys to two 1.91 *cm*

pulleys located on the main motor drive shaft. Each 1.91 cm pulley is affixed to the motor drive shaft with two 6.4 mm $6-32$ thread set screws. The motor drive shaft is a 9.5 mm hollow stainless steel rod, spanning the length of the apparatus. The motor drive shaft is supported by two aluminum pillow blocks, and, like the tank drive shafts, also equipped with two stop collars to prevent axial translation. Powering the drive shaft is a $120V$ AC/DC variable speed electric motor, located at one end of the drive shaft, and connected to the shaft itself with a spider coupling, to suppress any unpleasant effects that might result from slight motor-shaft misalignment (see Figures 3.9 and 3.10).

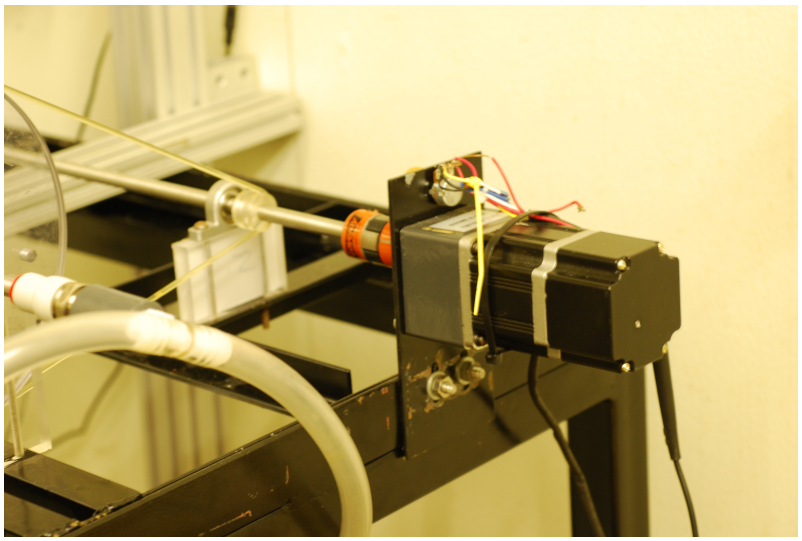

Figure 3.9: Photograph of the motor and motor drive shaft, including a pillow block, small pulley, and the spider coupling.

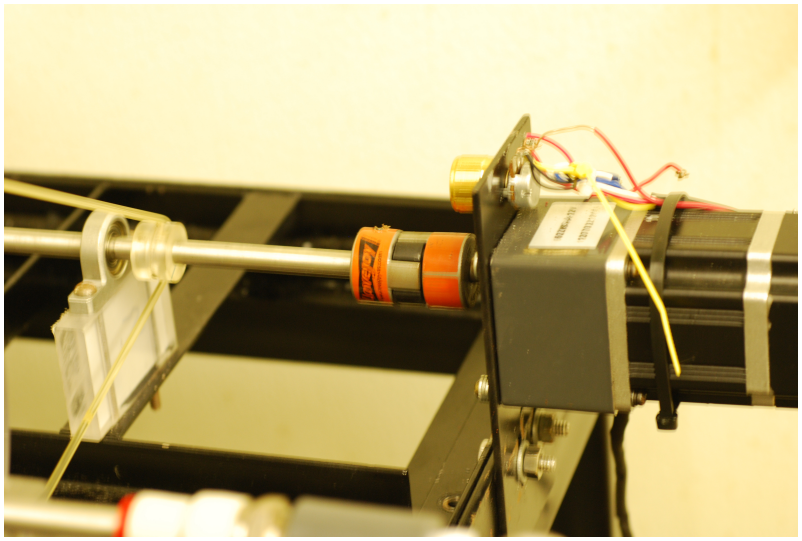

Figure 3.10: Close up of the spider coupling.

The entire apparatus rests on a stainless steel frame, welded together from 25.4 $mm \times 25.4\ mm \times 3.2\ mm$ angle bar.

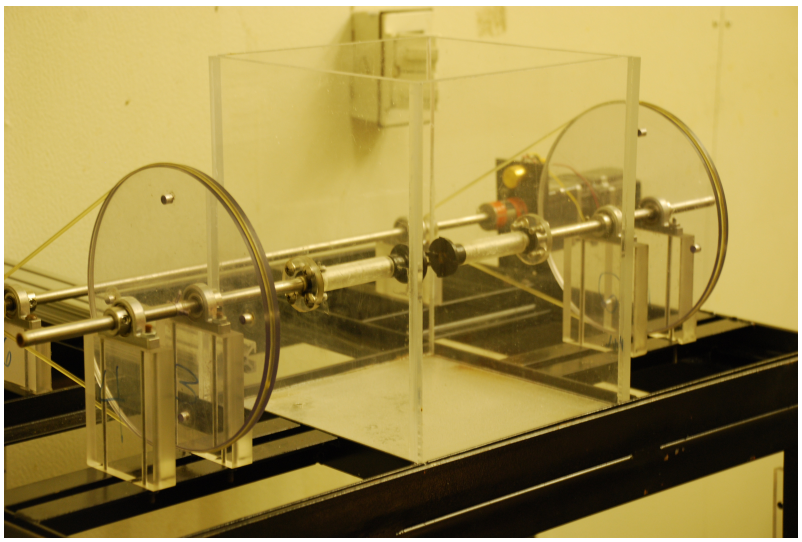

Figure 3.11: Photograph of the Burgers′ Vortex apparatus.

A significant design concept difference of note between the Burgers′ vortex apparatus (Figure 3.11) and the original vortex generator detailed by Manneville et al. [2000] and Petitjeans [2003] is the presence of the four equally spaced "paddles" on

the front face of each disk. Through the course of calibrating the Burgers′ vortex apparatus to achieve the desired vortex size and strength, it was determined that the shear stress generated from the (smooth) face of each disk was insufficient to induce fluid rotation in the region between the disks. Initial prototypes with smooth disks resulted in barely perceptible fluid motion in the center of the control volume (i.e., in the center between the two disks). As a result, the "paddles" were added to increase fluid rotation.

3.1.2 Target Parameters

Recall that the Burgers′ vortex apparatus is specifically intended to produce a vortex that mimics the characteristics of a vortex found in coastal zone turbulence, specifically isotropic turbulence "levels" 2 and 3, reported in the Webster et al. [2004] "T-Box" experiments.

Section 2.3.3 discusses the methodology necessary to determine the target parameters of the Burgers′ vortex, specifically the vortex radius (r_B), axial strain rate parameter (a), and circulation (Γ). The turbulence data tabulated in Webster et al. [2004] are the source of the turbulence characteristics required to estimate these parameters. Table 3.1 is a condensed version of the information found in Tables 2.1, 2.2, and 2.3, (reprinted from Webster et al. [2004]), specifically, the Kolmogorov length scale, η and the u_{rms} values. The u_{rms} values in Table 3.1 is the average of the u_{rms} values in Tables 2.1 and 2.2.

Table 3.1: Kolmogorov length scale, η and u_{rms} values for turbulence levels 1-4 in the Webster et al. [2004] T-Box.

Turbulence Level	**1**	**2**	**3**	**4**
η (cm)	0.15	0.10	0.057	0.045
u_{rms} (cm/s)	0.113	0.278	0.748	0.955

Equation 2.23 allows the estimation of the Burgers′ vortex radius, r_B given the Kolmogorov length scale, η. Specifically r_B is determined to be equal to 8.1η. From this value of r_B, the relationship in Equation 2.24 is used to determine the axial strain parameter, a. Lastly, the vortex circulation, Γ is computed from Equation 2.25. The results of these calculations for each of the four turbulence levels in the Webster et al. [2004] "T-Box" are reported in Table 3.2.

Table 3.2: Burgers′ vortex cartoon characteristic radius (r_B), axial strain (a) and circulation (Γ) target parameters for turbulence levels 1-4.

Turbulence Level	**1**	**2**	**3**	**4**
r_B (cm)	1.215	0.810	0.462	0.365
a (s^{-1})	1.423×10^{-2}	3.201×10^{-2}	9.851×10^{-2}	15.806×10^{-2}
Γ (cm^2/s)	0.859	1.412	2.168	2.187

3.1.3 Burgers′ Vortex Control Variables

The Burgers′ vortex apparatus has two easily-adjusted parameters that can be manipulated to alter the generated vortex. The first is the rotation rate of the drive shaft in RPM's (revolutions per minute), and the second is the flowrate of the fluid being withdrawn out the two rotating disks, Q (cm^3/min). These parameters are controlled through changing the speed of the electric motor and the flowrate settings

of the two flowmeters (one connected to each disk). To calibrate the rotation rate of the electric motor for each experiment, the motor was connected to a voltmeter (Fluke 73 III Multimeter, Fluke Corporation, Everett, WA) to measure control voltage. Measurements of the rotation rate were taken at 0.05 V intervals and a second-order polynomial function was fit to the data points, allowing the calculation of the rotation rate based on the control voltage. The results of the calibration function are given below.

$$RPM = 2.9409V^2 - 33.84V + 87.539 \tag{3.1}$$

In this equation the RPM is the rotation speed of the motor in revolutions per minute, and V is the control voltage. The pulley arrangement between the drive and disk shafts yields the following relationship:

$$RPM_d = 0.10 \times RPM \tag{3.2}$$

In this expression the RPM_d parameter is the rotation rate of the disks, and RPM is the motor revolutions per minute from Equation 3.1. The "gearing down" of the disk drive shaft is necessitated by the extremely low (relative to the motor revolutions per minute) disk revolutions per minute required to produce the target vortex, with the welcome benefit of significantly (by a factor of 10)increasing the torque available to spin the drive shafts when seated in the shaft seal.

The initial estimates of the rotation rate and flowrate necessary to produce the vortex require some initial assumptions and extrapolation; as such "dialing in" the

rotation rate and flowrate that *actually* produce the desired vortex required some iteration. The initial estimation procedure is as follows. The first step is the determination of several important physical dimensions of the Burgers′ vortex apparatus; the radius of the rotating disks is 1.5 cm, the separation between the disk outlets is 2.9 cm ($2.4 + 2 \times 0.25$, where 2.4 cm is the distance between the disk paddles, 0.25 cm is the paddle thickness), and the diameter of the disk flow outlet is 0.622 cm (the inner diameter of the hollow steel drive shaft). The construction of the Burgers′ vortex apparatus and the physical dimensions are discussed extensively in Section 3.1.1. With these dimensions in hand, one can compute what the x-direction velocity should be right at the disk outlet from Equation 2.15, e.g. u_x at the disk outlet is equal to $2ax$, where a is the target axial strain rate parameter found in Section 3.1.2, and x is the distance from the center of the vortex to the disk face ($2.9/2 = 1.45$ cm). The necessary flowrate, Q (cm^3/min) can be estimated by assuming constant velocity across the outlet cross-section and using the relationship $Q = VA$, where V is the x-direction velocity at the disk outlet, and A is the cross-section area of the disk flow outlet.

The rotation rate, ω (RPM), can be estimated from evaluating Equation 2.14 at the edge of the rotating disk. In this expression, $u_\theta = \frac{\Gamma}{2\pi r}\left[1 - e^{\left(\frac{-r^2 a}{2\nu}\right)}\right]$, r is the disk radius (1.5 cm), a is the target axial strain rate parameter, and Γ is the target circulation parameter. This allows the calculation of u_θ of the fluid adjacent to the outer edge of the disk. As an initial parameter estimation, u_θ of the fluid immediately adjacent to the edge of the disk is equal to u_θ of the disk (from the no-slip condition). Thus, the disk drive shaft rotation rate of the Burgers′ vortex apparatus must be such that it produces the calculated u_θ at the edge of the disk.

The final settings for the vortices corresponding to turbulence levels 2 and 3, shown in Table 3.3, were reached after implementing these estimation procedures,

and several iterations of varying the parameters and quantifying the flow via Tomo-PIV.

Table 3.3: The mean flow velocity at the disk flow outlet, u_x, disk rotation rate, ω, flowrate, Q, and voltage, V, settings used to produce turbulence level 2 and 3 Burgers′ vortices.

Turbulence Level	**2**	**3**
u_x (mm/s)	3.8	11.0
ω (RPM)	3.0	3.2
Q (cm^3/min)	7	20
Voltage (V)	2.074	1.998

3.2 Tomographic Particle Image Velocimetry

Data on the flow field induced by the Burgers′ vortex apparatus detailed in this thesis are collected through Tomographic Particle Image Velocimetry (henceforth referred to as Tomo-PIV). The purpose of these data are to quantify the flow field induced by the vortex generating apparatus for each of the two turbulence levels, both to ensure adherence to the desired characteristics of the vortex, as well as to have the flow field data to correlate with the behavioral assays. A brief overview of the basic principles of Tomo-PIV is outlined here, to provide the reader with some foundational knowledge of the topic. For a more thorough discussion of the topic, the reader is referred to an excellent topical review by Scarano [2013].

Tomo-PIV is a three dimensional, potentially time resolved, particle imaging technique that relies on sophisticated post-processing algorithms to create a three dimensional reconstruction of an illuminated volume of tracer particles [Elsinga et al., 2006a, Scarano, 2013]. This use of a three dimensional volume reconstruction, rather than

a series of two-dimensional measurement planes, distinguishes Tomo-PIV from many other forms of PIV, such as 3D particle tracking velocimetry [Scarano, 2013].

3.2.1 Tomo-PIV: Basic Principles

This section details the standard experimental setup for Tomo-PIV systems, as well as the process necessary to create the desired 3D velocity field. To begin, observe Figure 3.12, reproduced from Elsinga et al. [2005], which illustrates the basic setup and processes of Tomo-PIV.

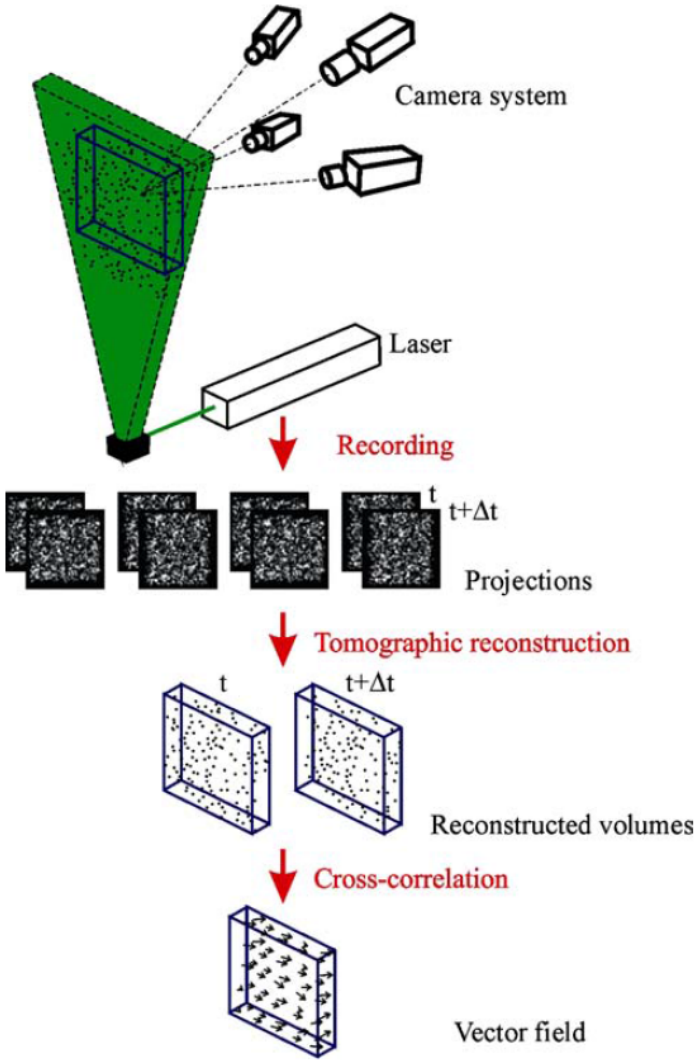

Figure 3.12: Generalized schematic of the Tomo-PIV setup. Reprinted from Elsinga et al. [2005].

First, consider the volume of the fluid to be measured. This measurement volume is illuminated by a light "column", typically generated by expanding a beam of laser light through an optical lens [Elsinga et al., 2006a, Scarano, 2013]. It is critical to maintain tight control over the size of the illuminated volume. Any light from outside the measurement volume will be included in the reconstructed volume as

noise [Scarano, 2013]. Thus, the practice of using razor blade or knife edge filters to cut down the light beyond the desired measurement volume has been adopted as standard practice [Scarano, 2013].

The fluid volume is seeded with tracer particles, which reflect light passing through the illuminated volume; this scattered light is collected into several (necessarily more than two) cameras [Scarano, 2013]. Each camera views the illuminated volume from a different angle. The setup of these cameras is a critical condition, as each image must be recorded in focus over the entire depth of the illuminated volume [Scarano, 2013]. The simplest way to increase the depth of field (the depth over which the object is in focus) is to increase the f-stop of the lens aperture [Scarano, 2013]. An increase in f-stop will increase the depth of field, but at the cost of decreasing the amount of light that reaches the camera sensor. Thus a balance must be reached between the aperture setting necessary to achieve the desired depth of field, and the light intensity required to observe the tracer particles. This balance is partially responsible for the limitations placed upon the thickness of the volume able to be accurately reconstructed [Scarano, 2013]. Additionally, one uses a Scheimpflug mount to align the camera sensor plane to the reference plane of the illuminated volume, somewhat mitigating the deleterious depth of field effects resulting from the angle between them [Scarano, 2013].

Each camera (typically) takes a set of image pairs, which can (and should) be pre-processed, then input into the tomographic reconstruction algorithm [Scarano, 2013]. The most widely accepted reconstruction algorithm is referred to as the multiplicative algebraic reconstruction technique (MART), which yields a three dimensional distribution of light intensity, $E(x, y, z)$ [Elsinga et al., 2006a, Scarano, 2013]. The particle reconstruction is performed by relating particle location in image space (particle location on the camera sensor) to a point in object space (the three dimensional reconstruction of the measurement volume) [Scarano, 2013]. To obtain an accurate relationship the system must be calibrated, accomplished by imaging a plate of evenly

spaced dots at set depth intervals through the entire measurement volume, similar to the calibration procedure for stereoscopic PIV [Scarano, 2013]. Unlike stereoscopic PIV, however, the calibration must be extremely precise [Scarano, 2013]. Work by Elsinga et al. [2006b] indicated that any motion of the cameras between data collection and calibration causing camera misalignment greater than a small fraction of the particle image will quickly result in unacceptable levels of error in the reconstructed particle field. For typical experimental conditions, camera motion in excess of the allowed tolerance is inevitable [Scarano, 2013]. Therefore, to correct for camera misalignment, three dimensional self-calibration procedures developed by Wieneke [2008] are necessary. For a more complete discussion of these calibration procedures, the reader is referred to Wieneke [2008].

Once the images have been processed, and the three-dimensional particle field obtained, the particle motion from one time step to the next is determined using a three-dimensional cross correlation [Scarano, 2013]. The position at which this correlation function is maximized gives the estimate of the displacement vector [Scarano, 2013]. To aid this process, one can incorporate multi-grid and iterative window deformation, techniques which use the calculated displacement vector from the previous time step as a "first guess" as to the location of the correlation function maximum at the subsequent time step [Scarano, 2002, 2013].

3.2.2 Tomo-PIV System

The specific Tomo-PIV system utilized in this study is nearly identical to that described in Murphy [2012]; the illumination and lens configuration are the only significant differences.

The system employs four Phantom v210 cameras (Vision Research Inc., Wayne, NJ) (Figure 3.13). While the cameras are capable of filming at more than two-thousand frames per second, all flow analysis for the present study is conducted at

Figure 3.13: Picture of the Tomo - PIV camera configuration. Each of the four Phantom v210 cameras is equipped with a Scheimpflug mount and a Nikon lens.

thirty frames per second. A high frame rate is necessary to capture turbulent velocity fluctuations, but for the steady state vortex flow field generated by the Burgers′ vortex apparatus, it is unnecessary. The resolution of each camera is 1280 x 800 pixels, sufficient to resolve the flow features of the Burgers′ vortex. The camera′s are each equipped with a 30 mm extension ring and a 105 mm focal length lens (Nikon, Tokyo, Japan). The viewing window for each camera is approximately 4 cm $\times$ 3 cm. The f-stop for each lens in all trials is set to f/22 to achieve the necessary depth of field (in the context of tomo-PIV, depth of field refers to the depth over which the tracer particles remain in focus) while still allowing sufficient light from the control volume. As suggested by Scarano [2013], Scheimpflug mounts are utilized on all cameras to alleviate some of the distortion due to the misalignment of the camera sensor plane and the viewing plane. The cameras are connected to optical rails by three-axis gear heads (Manfrotto, Cassola, Italy), rails that are themselves securely fastened to an optical table.

The interrogation volume is illuminated by a 33 W Nd:YLF pulse laser (Quatronix

Corp., Hauppauge, NJ) with a wavelength of 527 nm. Spherical plano-concave and biconvex lenses are used to expand and collimate the beam; the beam then passes through an adjustable aperture to "crop" it, with the goal of illuminating the control volume only. Any light outside the control volume will be incorporated into the reconstructed image - this is to be avoided if possible. For the Burgers′ vortex study the control volume is approximately 20 mm deep and 25 mm wide, i.e. the width of the gap between the disks. The depth of 20 mm approaches the practical limit of the depth of field of current Tomo-PIV systems, i.e. beyond this depth the 3-D particle reconstructions begin to lose substantial accuracy (if the volume can be reconstructed at all). This depth is insufficient to capture the entire Burgers′ vortex (recall the disks are 30 mm in diameter); to remedy this, it is assumed that the Burgers′ vortex is symmetric about the central axis, thus imaging the "front" half of the vortex is all that is required. Image acquisition and processing is performed in DaVis (LaVision, Ypsilanti, MI) on a Dell Precision M6500 laptop PC (Dell Inc., Round Rock, Texas). The four cameras and the laser pulse are synchronized using a LaVision high speed signal controller (LaVision, Ypsilanti, MI).

3.3 Tomo-PIV Flow Data Analysis

The images collected by the laptop PC are first pre-processed in DaVis (LaVision, Ypsilanti, MI) utilizing the following pre-processing algorithms: subtraction by sliding minimum over 3 $\times$ 3 pixels, normalization to a local average of 100 $\times$ 100 pixels, Gaussian smoothing of the tracer particles followed by sharpening of the smoothed particles, multiplying each pixel with a constant factor (10 $\times$), and masking out the rotating disks in each frame. Following image pre-processing, volumetric self-calibration is performed iteratively, following the procedures developed by Wieneke [2008].

At the conclusion of volumetric self-calibration the images are reconstructed in

DaVis into a three dimensional volume of light intensities with the fast-MART algorithm, a variation on the standard MART algorithm discussed in Section 3.2.2 that slightly reduces accuracy, while drastically decreasing compute time. As the MART (and fast-MART) algorithms are iterative by nature, any decrease in accuracy can be negated through additional iterations, and the savings in computational time for an individual iteration is often more than enough to compensate for the additional iterations required. The last step required along the velocity vector field acquisition path is the multi-pass three dimensional cross-correlation of the reconstructed light intensity volume using the procedure discussed in Scarano [2013].

At the conclusion of the image processing, volume reconstruction, and volume correlation, the DaVis software (LaVision, Ypsilanti, MI) provides the user with a three dimensional mesh of points at which the velocity vector components have been calculated. These data are exported as a .dat file, which can be opened an edited in Microsoft Notepad (Microsoft Corporation, Redmond, WA), and subsequently imported into Matlab (The MathWorks, Inc., Natick, MA).

3.3.1 Burgers′ Vortex Parameter Calculation Procedures

It must be confirmed that the flow field generated by the Burgers′ vortex apparatus is conforming to the desired flow characteristics. This section shall only discuss the *methods* used to compare the parameters of the flow field the Burgers′ vortex generates to the desired parameters. The derivation of the target Burgers′ vortex parameters, the results of the Jumar's [Jumars et al., 2009] procedure based upon the T-Box experiment data in Webster et al. [2004], as well as the comparison itself are treated in Sections 3.1.2 and 4.1, respectively.

Recall that in Section 2.3.3 the three main parameters of the Burgers′ vortex model were as follows: the Burgers′ vortex radius r_B, the constant axial strain rate parameter, a, and the vortex circulation, Γ. The velocity data from the Tomo-PIV

analysis are input into a specifically tailored Matlab code used to compute these three parameters following the procedures outlined below.

First, the centerline of the created flow field must be determined. The vorticity is maximum on the central axis of the vortex, i.e. $r = 0$.

$$\omega_x = \frac{\Gamma a}{2\pi\nu} e^{\left(\frac{-r^2 a}{2\nu}\right)} \tag{3.3}$$

Thus, the central axis of the vortex in each $y - z$ plane of tomo-PIV data is determined by locating the maximum of ω_x. For reference, from the perspective of the cameras in the tomo-PIV setup, the x-axis moves left to right across the volume, the y-axis bottom to top, and the z-axis front to back.

In the Matlab code, the vorticity is computed from the tomo-PIV velocity data, using a 2^{nd} order central difference scheme to determine the values of the velocity derivatives at each point. Then, the location of the central axis of the vortex is defined as the mode of the maximum vorticity location in each $y - z$ plane.

The axial strain parameter, a, is computed by determining the slope of u_x on the centerline of the Burgers′ vortex; recall from equation 2.15 that the slope of u_x is equal to $2a$. On the edges of the control volume the Tomo-PIV data often yields spurious vectors, therefore the Matlab program drops the first and last two points of the u_x data. The program then fits a line to the remaining data points, determines the slope, divides the slope by 2, and outputs a. Equation 2.24 is used to calculate r_B, once the axial strain parameter, a, is known.

Γ is defined in Kundu and Cohen [2004] as being equal to the area integral of the vorticity, $\vec{\omega}$. The integration is performed numerically for the front half region of the measurement volume using the discrete vorticity values, then multiplied by 2 to account for the contribution from the back half of the vortex.

3.4 Behavioral Assays and Data Analysis Techniques

3.4.1 Copepod Collection and Maintenance

Acartia tonsa copepods were collected off the coast of Maine, USA on July 2, 2013 by Rachel Lasley-Rasher using a vertical tow technique; and subsequently one-day air shipped to the Georgia Tech campus (Atlanta, GA). The copepods arrived on July 3, 2013, and were placed in a cold room at 12° Celsius and allowed to acclimate to temperature. Upon acclimation the copepod containers were diluted into larger buckets to provide the copepods with a less densely populated habitat, then fed algae. The water in the tanks was a combination of seawater shipped from Maine with the copepods and Instant Ocean artificial seawater with matching salinity and temperature (30-34 *ppt* and 12° Celsius). The buckets were aerated to maintain a reasonably high dissolved oxygen concentration.

3.4.2 Behavioral Assay Data Collection

The behavioral assays were performed on July 4, 2013 and July 5, 2013. Each behavioral assay consists of four stages. Stage one consists of a 30 minute copepod acclimation period, to allow the animals to become accustomed to the Burgers′ vortex tank. Stage two, a 55 minute recorded control period, with the Burgers′ vortex not running in the tank (i.e. stagnant flow conditions) to observe the copepod behavior in the tank in the absence of any stimuli - hereinafter referred to as the "control". Stage three, a 30 minute Burgers′ vortex flow establishment period, to allow the Burgers′ vortex to reach the prescribed steady state flow conditions. The fourth and final stage consists of a 55 minute recorded treatment period, to observe the behavior of the copepods in the presence of the Burgers′ vortex - hereinafter referred to as the "treatment". This procedure was repeated twice for each Burgers′ vortex strength, for a total of four data collection runs (each data collection run consists of a control and a treatment). All behavioral assays were conducted in the same apparatus, with

mixed-sex *Acartia tonsa*.

The experimental setup is as follows. Two Pulnix cameras (JIA, Inc., San Jose, CA), with a resolution of 720 × 480 pixels, are setup facing the "Front" and "Bottom" of the Burgers′ vortex tank. The "Front" camera face corresponds to the face of the tank opposite the motor drive shaft.

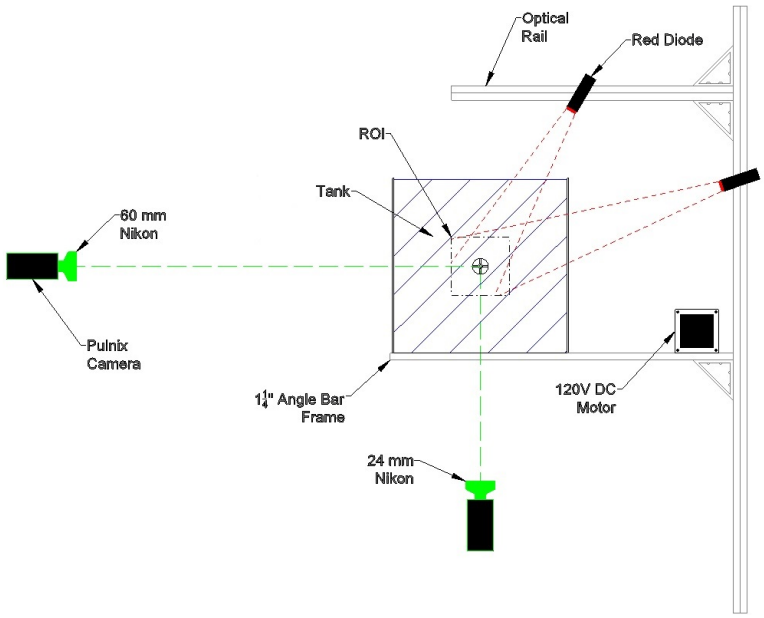

Figure 3.14: Schematic of the camera and lighting orientation, as well as the region of interest (ROI).

Both the front and bottom cameras are fitted with AF lens to C-mount camera adapters, to facilitate the use of Nikon camera lenses. The front camera is equipped with a $60mm$ Nikon lens and the bottom camera is equipped with a $24mm$ Nikon lens. Each camera records the video at $30Hz$ and transmits to a Sony Video Walkman Digital Video Cassette Recorder (Model GV-D900 NTSC - Sony, Inc.), which records the footage on 60 minute miniature digital video cassettes (Mini-DV's - either Panasonic, Inc. or Sony, Inc.). The cameras are focused on the rotating disks within the Burgers′ vortex apparatus, with roughly equivalent $9cm \times 7cm$ viewing windows. The tank illumination is provided by two near infrared fiber coupled diodes (CVI Melles Griot, 57PNL054/P4/S, $660nm$, $22mW$, Rochester, NY) (Figure 3.15).

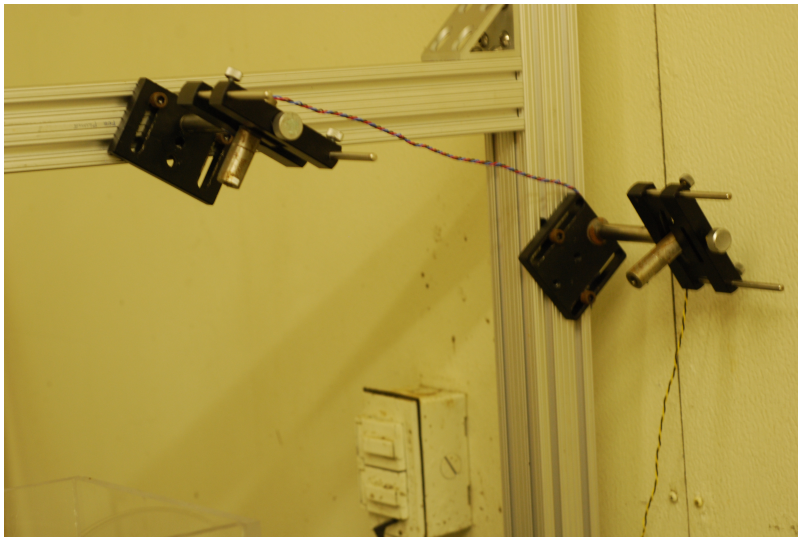

Figure 3.15: Picture of the two near IR diodes oriented to provide optimum ROI illumination.

3.4.3 Behavioral Assay Data Processing

The mini DV tapes are converted into .png (Portable Network Graphics) images using Adobe Premier Pro (Adobe Systems, Inc.), with each .png file representing a single frame of the video. The .png images are created at $15Hz$, therefore only every other frame is incorporated into the digitized video reconstruction. The .png files are processed into .avi (Audio-Video Interleave) movies using custom Matlab code written by Aaron True. The code reads in the individual .png images and creates an image stack; each image stack is a $720 \times 480 \times$ Number of Frames matrix. The image stack is processed in Matlab before being written to an .avi file; specifically, the code computes the mode of each pixel over the entire range of frames in the image stack and then subtracts that value from each pixel throughout every frame in the image stack. The filtered image stack is then converted to 256 color intensity greyscale and written to an uncompressed .avi file. This method of creating .avi files places limitations on the size of the .avi allowed; in this case the maximum uncompressed file size is approximately 2 giga-bytes. Therefore each 55 minute video is broken up into roughly 24 .avi clips, each clip consisting of a 2 minute 22 second 15 Hz uncompressed

.avi file.

Three-dimensional copepod trajectories are obtained through a lengthy and labor intensive process. First, the copepods in the front camera .avi files are tracked manually in DLTdv5, a Matlab particle tracking software developed by Hedrick [2008] at UNC Chapel Hill (Chapel Hill, North Carolina, USA). Second, the two-dimensional front camera trajectories created in the first step are run through a custom Matlab program. This program creates a new bottom camera "match file" by converting the front camera trajectory to the same frame of reference as the bottom camera. The key alterations made by the program are synchronizing the images in time, shifting the coordinate system to a common origin, and adjusting the scale (mm per pixel) to account for the differently sized viewing windows between the front and bottom cameras. The y-coordinates of the converted front camera trajectories are set to the image centerline (240 pixels), leaving only the x-position of the front camera trajectory variable. These bottom camera "match file" trajectories are loaded into the corresponding bottom camera .avi file. Figures 3.16 and 3.17 show the original front camera image, and the shifted bottom camera "match file" trajectory loaded into the bottom camera .avi respectively.

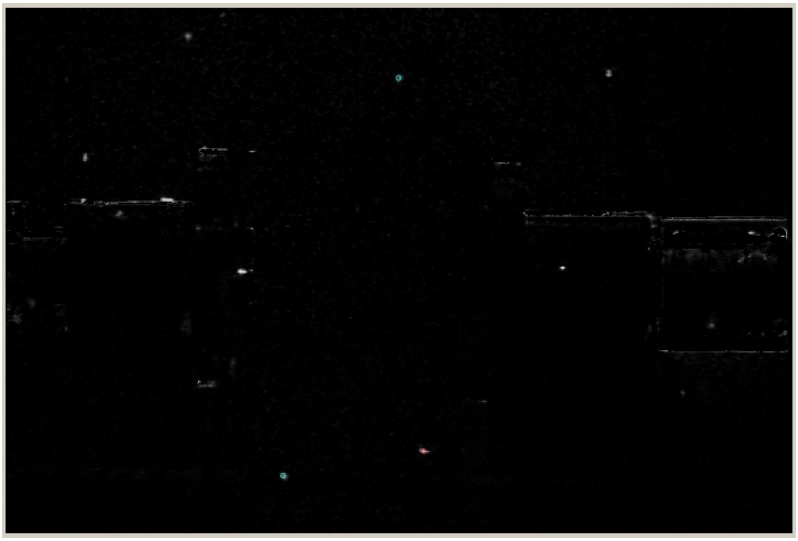

Figure 3.16: Single frame of a Front Camera .avi movie (Turbulence Level 2, Treatment Replicant 1, Front Camera .avi movie 1)), illustrating the original front camera copepod location. The red dot signifies the copepod location currently selected, the blue dots the non-selected copepod locations already tracked.

Figure 3.17: Single frame illustrating the copepod locations in Figure 3.16 converted and imported into the Bottom Camera .avi movie (again, Turbulence Level 2, Treatment Replicant 1, Bottom Camera .avi movie 1).

The third step is to manually go through each bottom camera .avi file (with the front camera copepod trajectory information visible) and search for bottom camera copepod trajectories that "match" the x-displacements of the front camera trajectories. Only the bottom camera copepod trajectories that are found to correspond to a front camera trajectory are tracked. This process is performed until 50 high quality matching trajectories are found in each control and treatment (in this context, high quality refers to trajectories that exceed 70 frames in length and the match is *quite certain*). Figure 3.18 pictorially represents this process.

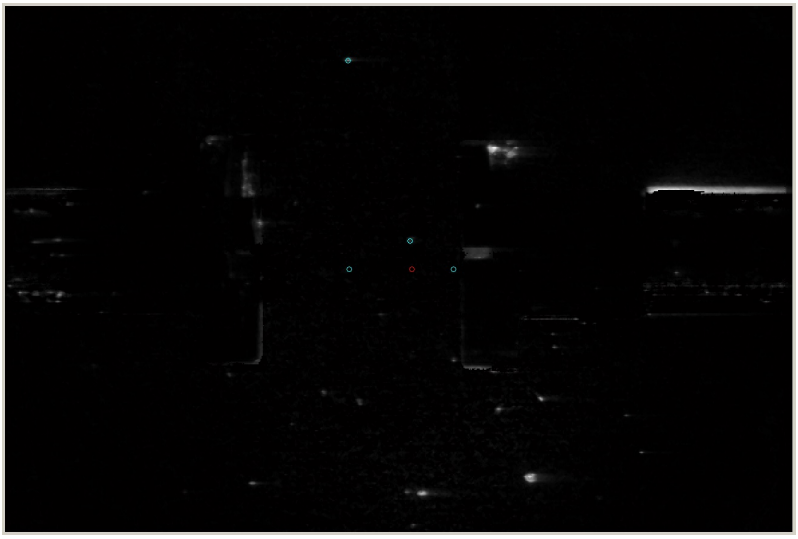

Figure 3.18: Single frame of Bottom Camera .avi (Turbulence Level 3 Treatment Replicant 2, Bottom Camera .avi movie 1), illustrating two discovered matches. Notice the two leftmost marks on the centerline (which correspond to the front camera converted locations) trajectories correspond to the same x-position as the matching bottom camera trajectories identified above them in the image.

In the fifth step, the bottom camera trajectories are combined with the original (unaltered) front camera trajectories using another Matlab code, which takes the y-component of each bottom camera trajectory, converts it to the front camera reference frame (using essentially the inverse of the process outlined in step two above), then

appends it to the front camera x and y data as the z component of the trajectory.

This process yields the three dimensional spatial position of each copepod as a function of time. To obtain the copepod velocity at each instant in time, finite difference approximations (i.e., central difference method) are performed on the copepod position data.

Lastly, the Burgers′ vortex flow velocity at the physical position of each copepod at each time step is calculated by synchronizing the origin of the copepod trajectories and the experimental flow data calculated in Section 3.3 via a trilinear interpolation function (see Figure 3.19) to interpolate the velocity at the copepod position by weighting the contributions from the eight neighboring flow data points.

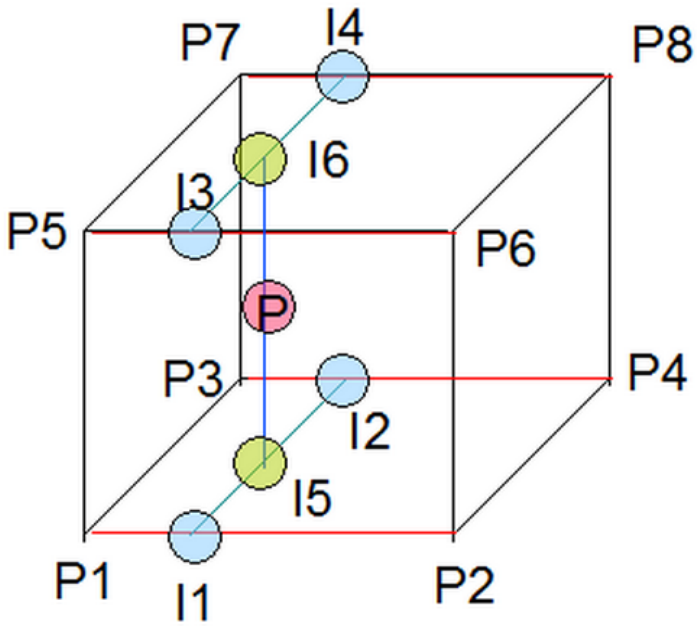

Figure 3.19: Sketch of the principles of trilinear interpolation. Reprinted from Kitchin [2014].

The flow velocities in the y- and z- directions at copepod positions located outside of the y and z range of the flow data are calculated from the theoretical Burgers′

vortex equations located in Section 2.3.1, specifically by solving Equations 2.13 and 2.14, with the appropriate values of a, Γ, and r_B calculated from the procedures in Section 3.3.1 substituted in, for u_r and u_θ and converting to Cartesian coordinates. The flow velocity in the x-direction is assumed to be zero in this case. If the copepod position is located outside the x range of the flow data but *inside* the y and z range, then the flow velocities in the x, y, and z directions are computed in the same manner, this time including Equation 2.15. If the copepod trajectory comes from a control case, then the flow velocities are necessarily zero.

3.4.4 Behavioral Assay Data Analysis

This section discusses the different copepod swimming behavior parameters that will be calculated and compared in the Results section, as well as a brief overview of the calculation algorithms.

3.4.4.1 Mean Relative Swimming Speed

The first parameter is the relative swimming speed. Physically this corresponds to how fast the copepod is moving relative to the flow velocity. The relative swimming speed is computed at each time step in the following manner:

First, compute the x y and z direction velocity differences.

$$u_{rs} = u_{copepod} - u_{flow} \tag{3.4}$$

$$v_{rs} = v_{copepod} - v_{flow} \tag{3.5}$$

$$w_{rs} = w_{copepod} - w_{flow} \tag{3.6}$$

Then, compute the velocity difference vector magnitude, $|\vec{u_{rs}}|$.

$$|\vec{u_{rs}}| = \sqrt{(u_{rs})^2 + (v_{rs})^2 + (w_{rs})^2} \tag{3.7}$$

The mean relative swimming speed for each trajectory is defined as:

$$\overline{|\vec{u_{rs}}|} = \frac{1}{n}\sum_{i=1}^{n} |\vec{u_{rs}}| \tag{3.8}$$

Where n is the number of frames in the trajectory.

3.4.4.2 Turn Frequency

The second parameter is the turn frequency. The turn frequency physically corresponds to the number of times the copepod changes its directional heading by more than 20° per second of time in the track. This parameter is computed by exploiting the geometric definition of the dot product to calculate the angle θ between the velocity vector at time $t + \Delta t$ and the velocity vector at time t, specifically:

$$\theta = \arccos\left(\frac{\overrightarrow{u_{t+\Delta t}} \cdot \overrightarrow{u_t}}{|\overrightarrow{u_{t+\Delta t}}||\overrightarrow{u_t}|}\right) \tag{3.9}$$

Then, to compute the turn frequency, the number of turns greater than 20° is divided by the total time of the trajectory.

3.4.4.3 Net-To-Gross Displacement Ratio

The third parameter is the net-to-gross displacement ratio (NGDR). The NGDR quantifies how straight the path is. For reference, a NGDR of 1 corresponds to a perfectly straight line, and a NGDR of 0 refers to a trajectory that ends at the exact same physical position as it begins. When comparing values of NGDR, it is critical to compare trajectories of the same length of time (or same displacement) since NGDR is scale dependent. As a general rule, shorter trajectories tend to have lower NGDR's, and longer trajectories higher NGDR's. Thus, to ensure unbiased results,

each copepod trajectory is broken up into 3 second (45 frame) sub-trajectories before computing the NGDR. The NGDR is calculated in the following manner.

Define the net displacement of each 45 frame sub-trajectory:

$$|\overrightarrow{x_{net}}| = \sqrt{(x_{45} - x_1)^2 + (y_{45} - y_1)^2 + (z_{45} - z_1)^2} \tag{3.10}$$

where the subscripts indicate the frame number. The gross displacement for the same sub-trajectory is computed using the following algorithm.

$$|\overrightarrow{x_{gross}}| = \sum_{i=1}^{44} \sqrt{(x_{i+1} - x_i)^2 + (y_{i+1} - y_i)^2 + (z_{i+1} - z_i)^2} \tag{3.11}$$

The mean NGDR for each trajectory is the average NGDR of each 45 frame sub-trajectory.

3.4.4.4 Alignment With the Vortex Axis

The fourth parameter is the alignment with the vortex axis. Physically, it corresponds to the angle between the copepod heading and the axis of rotation of the Burgers′ vortex. The algorithm to compute the axis alignment is similar to the turn frequency algorithm, except that the two vectors are the velocity vector at time t, $\vec{u_t}$, and the unit vector in the x-direction, $\hat{i}$. Before the angle is calculated, the x-direction velocity is replaced by the absolute value of the x-direction velocity since it is irrelevant whether the vector is aligned with the positive or negative $\hat{i}$ direction. Therefore, each angle will be less than or equal to 90°, and is computed as follows:

$$\theta = \arccos\left(\frac{\overrightarrow{u_t} \cdot \hat{i}}{|\overrightarrow{u_t}||\hat{i}|}\right) \tag{3.12}$$

To compute the mean alignment with the vortex axis for each trajectory the axis alignment angles are averaged over the total number of time steps in the trajectory.

3.4.4.5 Escapes per 5 Seconds per Copepod

The fifth behavior parameter is the number escapes per copepod per five seconds. This provides a normalized measure of copepod escape frequency. In this study, a copepod escape is defined as any instance of the copepod acceleration equaling or exceeding twice the mean copepod acceleration. To compute the copepod acceleration finite difference approximations are performed on the copepod velocity data in each of the three coordinate directions, (i.e., central difference):

$$a_{x_t} = \frac{u_{t+\frac{\Delta t}{2}} - u_{t-\frac{\Delta t}{2}}}{\Delta t} \tag{3.13}$$

The acceleration magnitude at each time step is then given by the following: expression:

$$|\vec{a}| = \sqrt{(a_x)^2 + (a_y)^2 + (a_z)^2} \tag{3.14}$$

Each instance of the copepod acceleration magnitude equaling or exceeding $2 \times \overline{|\vec{a}|}$ for a continuous sequence of one or more time steps is counted as a single escape. To compute the number of escapes per 5 seconds, the total number of escapes in each trajectory is divided by the trajectory duration, then multiplied by 5.

3.4.4.6 Escape Jump Location

The sixth copepod behavior parameter is the escape jump locations. Physically, this corresponds to the radial distance from the vortex axis to the location of an escape jump. This is simply quantified by calculating the copepods radial position from the y and z copepod position data at the first frame of the escape jumps already identified in Section 3.4.4.5.

3.4.4.7 Escape Acceleration

The seventh copepod behavior parameter is the mean escape acceleration. This physically corresponds to the acceleration of the copepod during the previously identified escape events. The accelerations at each frame of an escape event are already known from the analysis performed in Section 3.4.4.5, thus the mean acceleration during each escape event is simply the average of the accelerations in each frame of the escape.

3.5 Statistical Analysis

The copepod behavior data for control vs. treatment cases is statistically compared using an analysis of variance (ANOVA) test. In simple terms, ANOVA is a statistical test that determines the probability that two sets of data have the same mean, given the observed variance in the data (Zar [1999]). In this study, the ANOVA statistical tests are performed in JMP Pro 11 (SAS Institute Inc., Cary, North Carolina). The one-way (single factor) ANOVA computations for two sets of data result in the F-test statistic, which is compared to the critical value of the F-statistic for a given confidence level (95% in this case). If the value of the F-statistic yielded by the analysis equals or exceeds the critical F-value, then the null hypothesis is rejected. In this context, the null hypothesis, H_0, is that the means of the two data sets are equal. In addition to reporting whether the null hypothesis is rejected or not, the JMP analysis also reports the p-value of the test. The p-value corresponds to the probability that the means of the two data sets are equal. In the context of ecology research, a p-value less than 0.05 is considered to be a statistically significant result.

Several conditions must be met to ensure the validity of the results of ANOVA tests. These conditions include: random sampling of data, statistically independent samples, that the distributions of the resulting data closely approximate a normal distribution, and that the variance across treatment groups is the same [Zar, 1999].

While not a requirement for ANOVA analysis, the statistical power of the test is improved with equal sample sizes [Zar, 1999]. That being said, one of the key attractions of ANOVA in the context of animal behavior research is the relative robustness of the test with unequal sample sizes.

ANOVA is an effective test in the current study for several reasons. The random selection of *Acartia tonsa* ensures that the first criteria of ANOVA is met, and taking the statistical comparison data as the means of the copepod behaviors described in Section 3.4.4 strongly indicates the third criteria will also be met. Further, each set of data contains the results from approximately 60 trajectories. As such, the sample sizes are nearly equal in any statistical comparison, increasing the power of the test.

The ANOVA tests performed in this thesis are one-way single factor (two level) repeat-measures ANOVA. The factor of interest is the presence of the Burgers′ vortex or not, and the two levels within that factor are the two replicates of each Turbulence Level treatment. The replicates are nested inside of the Turbulence Level effect and tested for significance. If there is no effect of the replicate on the data, then the data of the two replicates are pooled (i.e., combined within the Turbulence Level). This statistical analysis is performed on each of the behavioral parameters introduced in Section 3.4.4.

CHAPTER IV

RESULTS AND DISCUSSION

4.1 Theoretical vs. Generated Vortex Flow Field

This section discusses the effectiveness with which the experimentally generated vortex mimics the vortices with median dissipation corresponding to Turbulence Levels 2 and 3 in Webster et al. [2004]. In addition, it contains a detailed comparison of the flow field generated by the Burgers′ vortex apparatus (discussed in Section 3.1.1) to the theoretical Burgers′ vortex flow field covered extensively in Section 2.3.2.

4.1.1 Comparison of Generated Vortex with Target Parameters

Tables 4.1 and 4.2 compare the target turbulence level vortex radius (r_B), strain rate (a), and circulation (Γ) parameters to the experimental vortex data for that same turbulence level. Recall that the target parameters are obtained by performing the procedures outlined in Section 2.3.3 on the Webster et al. [2004] turbulence data (the mean dissipation rate $\langle\epsilon\rangle$, the Kolmogorov length scale η, and the root mean square of the velocity fluctuations u_{rms}).

Table 4.1: Comparison of the target Turbulence Level 2 parameters (vortex radius r_B, strain rate a, and circulation Γ) to those computed from the Turbulence Level 2 experimental vortex data.

Turbulence Level 2	**Target**	**Meas.**
$\langle\epsilon\rangle$ (cm^2/s^3)	0.009	
η (mm)	1.0	
u_{rms} (mm/s)	2.78	
r_B (mm)	8.10	7.5
a (s^{-1})	3.201×10^{-2}	4.16×10^{-2}
Γ (cm^2/s)	1.412	1.468

The results show that the Turbulence Level 2 vortex generated by the Burgers′ vortex apparatus is quite close to the same size as the target vortex, with the measured r_B roughly 7% smaller than the target radius (see Table 4.1). The measured strain rate parameter a is in the vicinity of the target strain rate parameter, less than 30% higher than the target value. Lastly, the measured vortex circulation Γ is only 4% greater than the target value. It is sensible to conclude that the Burgers′ vortex apparatus is producing a very reasonable facsimile of the theoretical Turbulence Level 2 Burgers′ vortex cartoon. Based upon these results and the analysis in Section 2.3.2, it would be expected that the experimental vortex would be roughly the same size as the target vortex, but with slightly higher maximum strain rate and maximum vorticity, due to the larger strain rate parameter, a.

Table 4.2: Comparison of the target Turbulence Level 3 parameters (vortex radius r_B, strain rate a, and circulation Γ) to those computed from the Turbulence Level 3 experimental vortex data.

Turbulence Level 3	**Target**	**Meas.**
$\langle\epsilon\rangle$ (cm^2/s^3)	0.096	
η (mm)	0.57	
u_{rms} (mm/s)	7.48	
r_B (mm)	4.62	4.90
a (s^{-1})	9.851×10^{-2}	10.025×10^{-2}
Γ (cm^2/s)	2.168	1.735

Table 4.2 compares these parameters for the Turbulence Level 3 vortex. As with the generated Turbulence Level 2 vortex, the measured Level 3 vortex is very close in size to the target vortex (6% larger in this case). However, the measured Level 3 vortex much more accurately mimics the target strain rate parameter than the measured Level 2 vortex. The value of a for the Burgers′ vortex apparatus produced Level 3 vortex is less than 2% higher than the target value. The measured vortex Γ is approximately 20% lower than the target value. Overall, it is reasonable to conclude that the Burgers′ vortex apparatus is also capable of producing an accurate approximation of the theoretical Turbulence Level 3 Burgers′ vortex cartoon. Due to the decreased circulation in the measured vortex, one might expect to obtain slightly lower maximum strain rate and vorticity in than is desirable based upon the target conditions, but these effects are mitigated by the slightly higher strain rate parameter, a.

4.1.2 Generated Vortex Profiles Vs. Theoretical Burgers′ Vortex Profiles

This section compares the profiles of the Turbulence Level 2 and 3 vortices generated by the Burgers′ vortex apparatus to those that would be produced by theoretical Burgers′ vortices with identical strain rate parameter and circulation. This is to say that in all subsequent plots, the theoretical vortex of a given level has the same values of the strain rate parameter and circulation, but *not* necessarily the same r_B, as those found in the *measured* column of Tables 4.1 and 4.2.

4.1.2.1 u_θ Profiles

Figures 4.1 and 4.2 compare the theoretical u_θ profiles and the characteristic vortex radii (r_B) to the experimental data. For Turbulence Level 2, the experimental vortex accurately reproduces the velocity profile shape, but consistently displays higher velocities at any given radius, something on the order of 50% larger at the radius of maximum u_θ (see Figure 4.1). The experimental vortex radius is very similar to the theoretical vortex radius, another piece of evidence confirming the similarity of the experimental and theoretical velocity profiles.

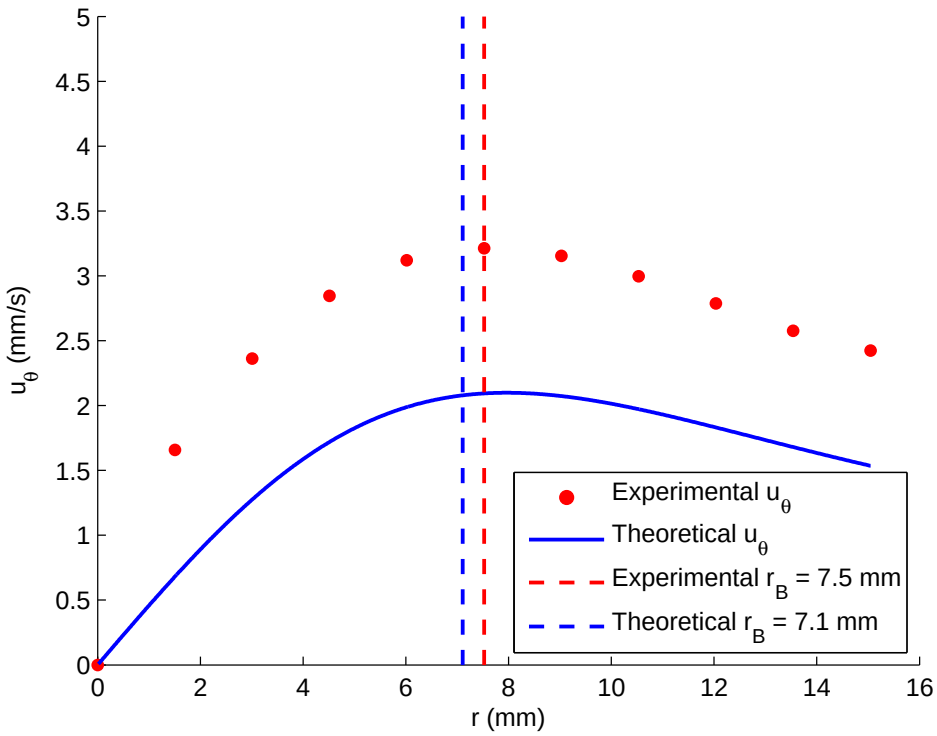

Figure 4.1: Profiles of u_θ comparing the theoretical prediction to the experimental data for Turbulence Level 2.

The comparison of the experimental Turbulence Level 3 vortex (see Figure 4.2) to the theoretical profile reveals slightly different characteristics than the Level 2 case. The experimental Level 2 vortex appeared to have the exact same profile as the theoretical vortex, only shifted up by a consistent value, whereas the experimental Level 3 appears to come up to a higher maximum u_θ (than the theoretical vortex) and then collapse onto the u_θ profile of the theoretical vortex. Despite the slightly higher peak (roughly 29% larger), the experimental Level 3 vortex appears to mimic the u_θ profile characteristics of the theoretical vortex. As was the case for the Level 2 vortex, the experimental Level 3 vortex radius, r_B, is very similar to the theoretical vortex radius.

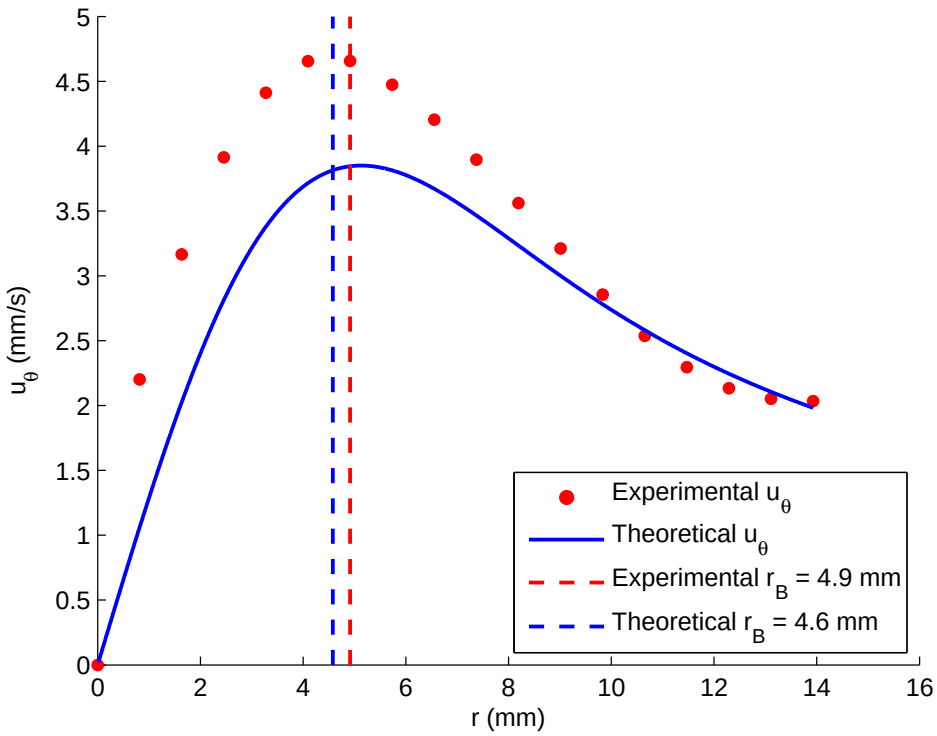

Figure 4.2: Profiles of u_θ comparing the theoretical prediction to the experimental data for Turbulence Level 3.

4.1.2.2 Axial Velocity Profiles

As shown in Figure 4.3, the experimental Turbulence Level 2 vortex very accurately mimics the axial velocity characteristics of the theoretical Level 2 vortex, both in profile shape and velocity magnitude.

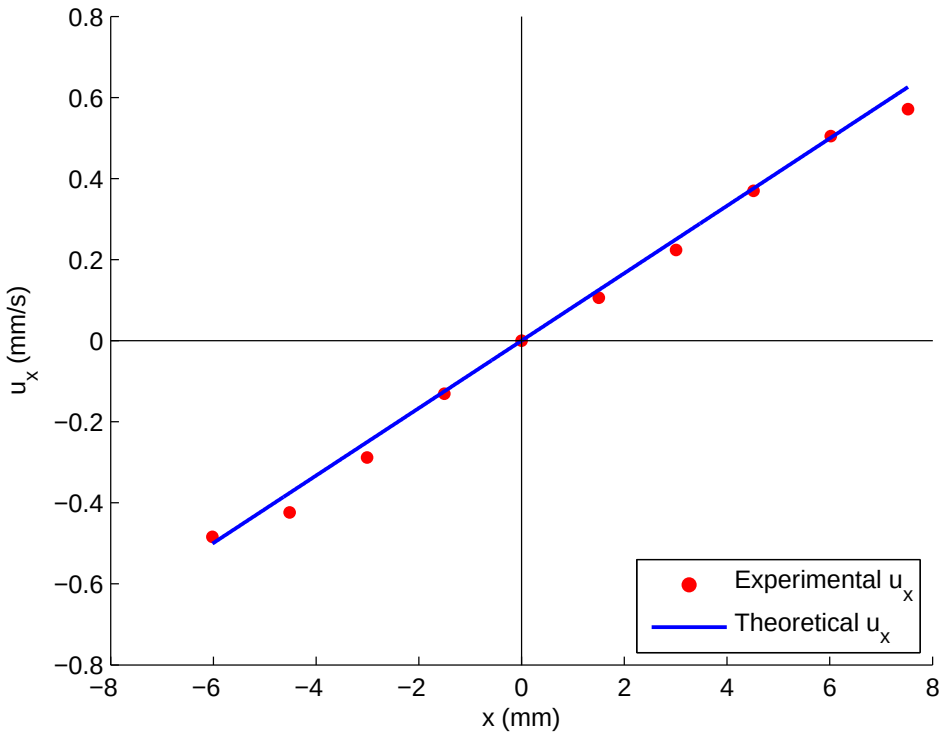

Figure 4.3: Profiles of u_x comparing the theoretical prediction to the experimental data for Turbulence Level 2.

As shown in Figure 4.4, the experimental u_x profile matches the theoretical profile quite well to one side of the vortex midpoint (the negative x values shown in the figure). However, on the other side of the vortex midpoint (positive x), the experimental u_x profile appears to change its slope, becoming steeper than the theoretical profile, before flattening out to a constant axial velocity at x positions above 6 mm.

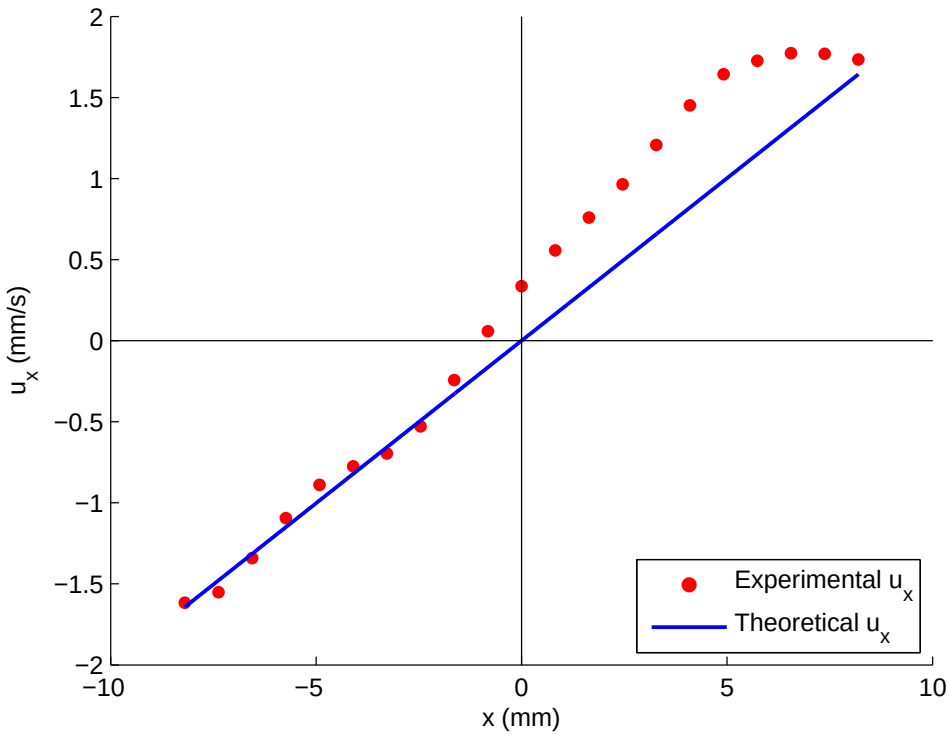

Figure 4.4: Profiles of u_x comparing the theoretical prediction to the experimental data for Turbulence Level 3.

4.1.2.3 Vorticity Profiles

Figures 4.5 and 4.6 compare the theoretical Turbulence Level 2 and 3 vorticity profiles to the experimental data. The experimental Turbulence Level 2 vortex is marvelously mimicking the vorticity profile of the theoretical Level 3 vortex. The only difference of note is that the experimental vorticity profile displays slightly higher maximum vorticity (on the vortex centerline), but collapses to the theoretical vorticity profile as the radius increases.

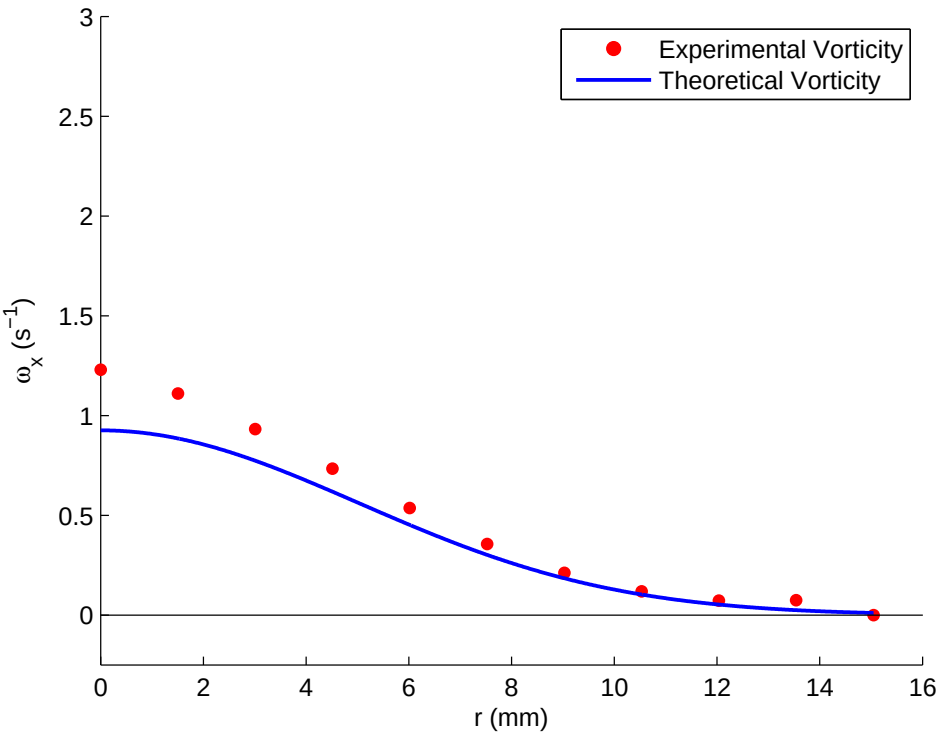

Figure 4.5: Profiles of vorticity (ω_x) comparing the theoretical prediction to the experimental data for Turbulence Level 2.

Similarly, the experimental Turbulence Level 3 vortex very accurately reproduces the vorticity profile of the theoretical Level 3 vortex. As with the Level 2 profile, the experimental Level 3 vorticity profile displays slightly higher maximum vorticity (on the vortex centerline), but collapses to the theoretical vorticity profile as the radius increases. Unlike the Level 2 vortex, the experimental Level 3 vorticity actually becomes slightly negative at large radii.

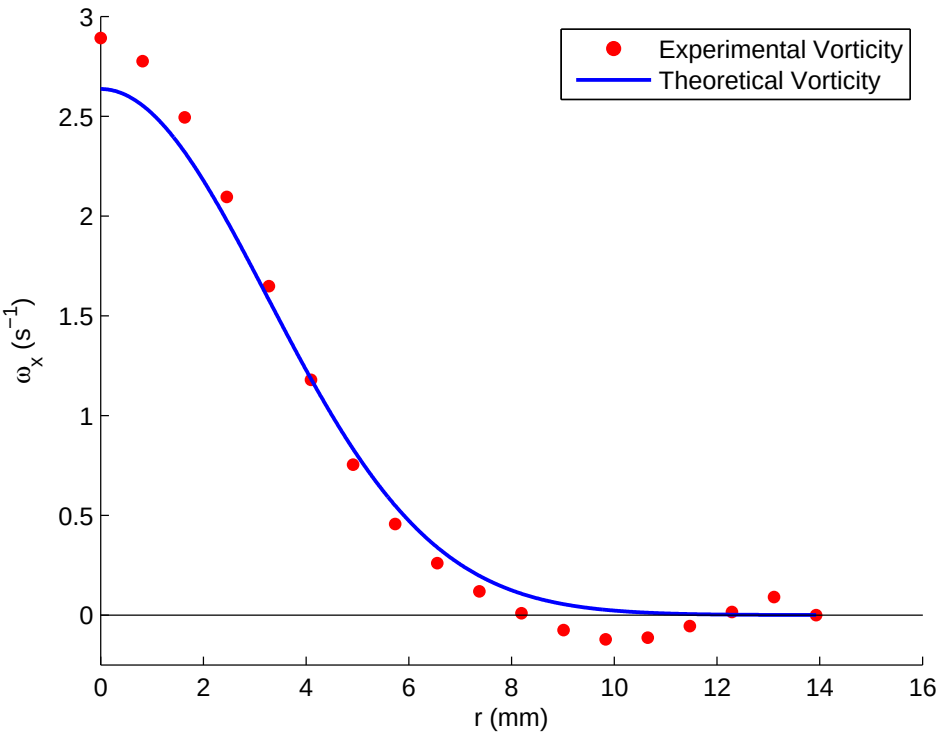

Figure 4.6: Profiles of vorticity (ω_x) comparing the theoretical prediction to the experimental data for Turbulence Level 3.

Overall, the Burgers′ vortex apparatus does an outstanding job replicating the vorticity profiles of the Burgers′ vortex cartoons corresponding to Turbulence Levels 2 and 3.

4.1.2.4 Maximum Principle Strain Rate Profiles

As was the case for the u_θ profile, the experimental Turbulence Level 2 maximum principal strain rate (MPSR) profile displays nearly identical profile shape to the theoretical vortex, but appears to be shifted up by a constant amount (see Figure 4.7). The experimental and theoretical profiles appear to start off at the same constant strain rate for small radii, but once the profiles begin climbing to their peak values, the experimental MPSR profile rises above the theoretical one, and remains there for the rest of the profile.

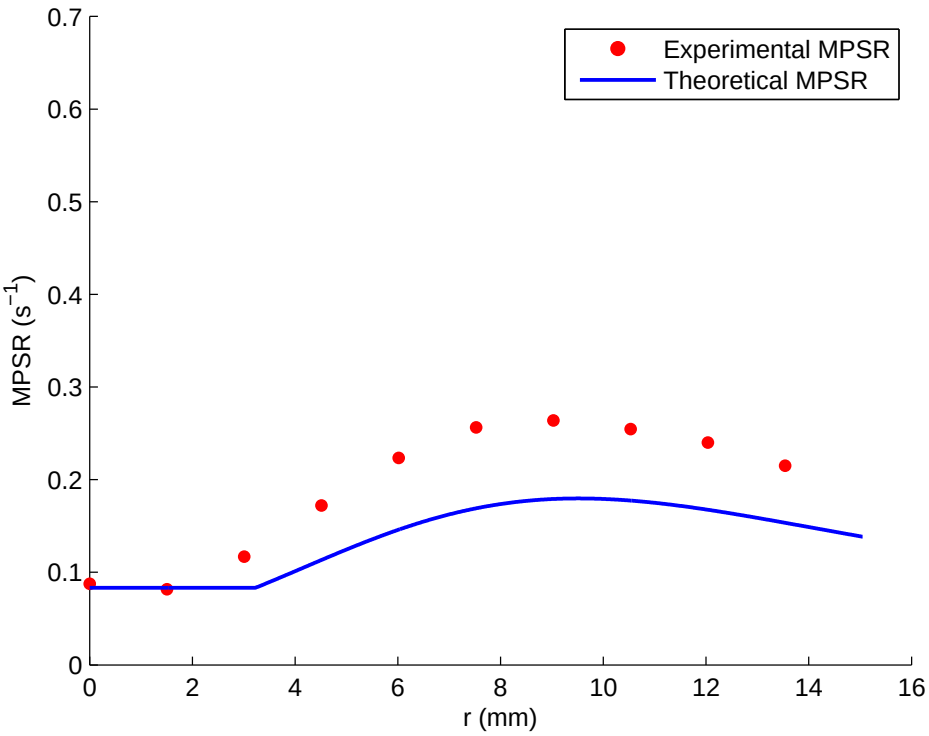

Figure 4.7: Profiles of MPSR comparing the theoretical prediction to the experimental data for Turbulence Level 2.

As shown in Figure 4.8, the experimental Turbulence Level 3 maximum principal strain rate profile possesses nearly identical profile shape to the theoretical profile for the majority of the radii in the control volume. The experimental profile does approach the theoretical profile at the largest radii in the control volume, as the maximum principal strain rate profiles decay from their peak values. Unlike the experimental Level 2 vortex (which displayed identical MPSR values during the constant phase of the MPSR profile at small radii), the experimental Level 3 vortex MPSR profile is constantly shifted upwards by a set amount in the region near the vortex central axis.

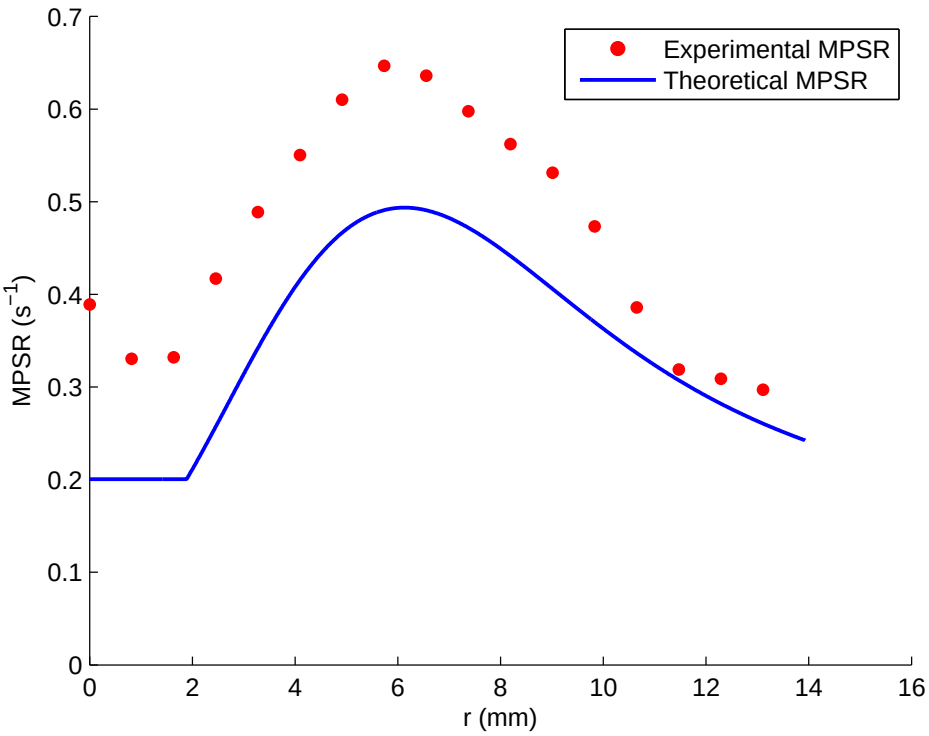

Figure 4.8: Profiles of MPSR comparing the theoretical prediction to the experimental data for Turbulence Level 3.

4.1.2.5 $e_{r\theta}$ Profiles

Figure 4.9 compares the experimental Turbulence Level 2 $e_{r\theta}$ profile to the same profile for the Burgers′ vortex cartoon. As has been the case for several of the profiles discussed, the experimental Level 2 $e_{r\theta}$ profile appears to be slightly higher than the theoretical profile at all radii, while retaining the same basic shape of the theoretical profile.

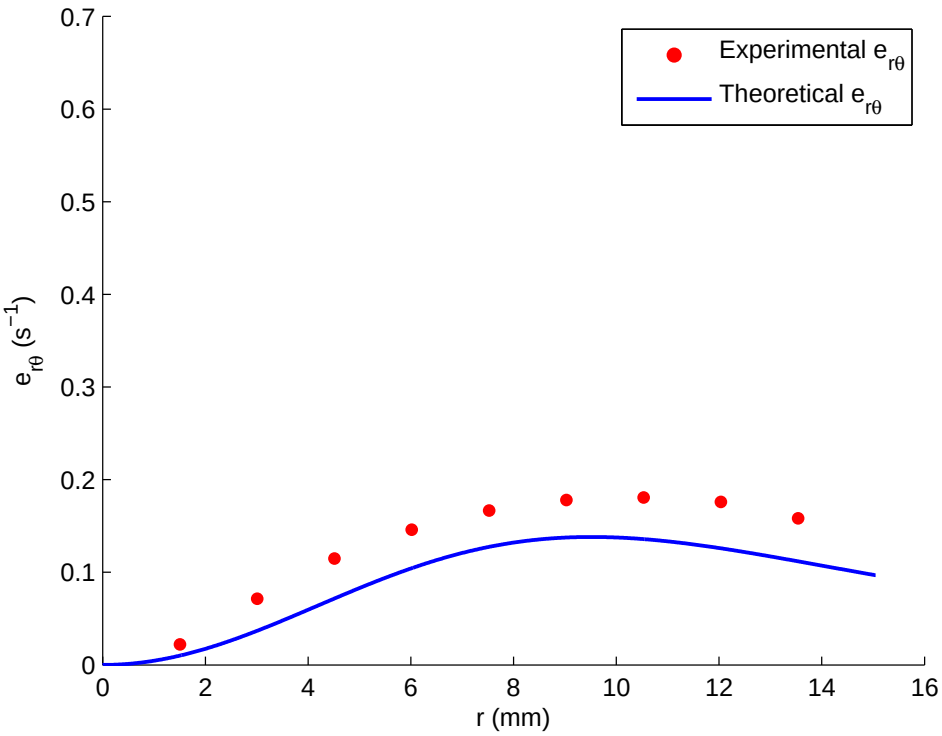

Figure 4.9: Profiles of $e_{r\theta}$ comparing the theoretical prediction to the experimental data for Turbulence Level 2.

The experimental $e_{r\theta}$ profile for Turbulence Level 3 again appears to have the same basic shape as the theoretical profile for the majority of radii in the control volume, with the constant upward offset in experimental $e_{r\theta}$ values (see Figure 4.10). From Figure 4.10, it is clear that the reason the experimental Level 3 maximum principal strain rate profile shape breaks away from the theoretical MPSR profile shape (in Figure 4.8, for large values of the radius) is due to a precipitous drop in $e_{r\theta}$ for large radii.

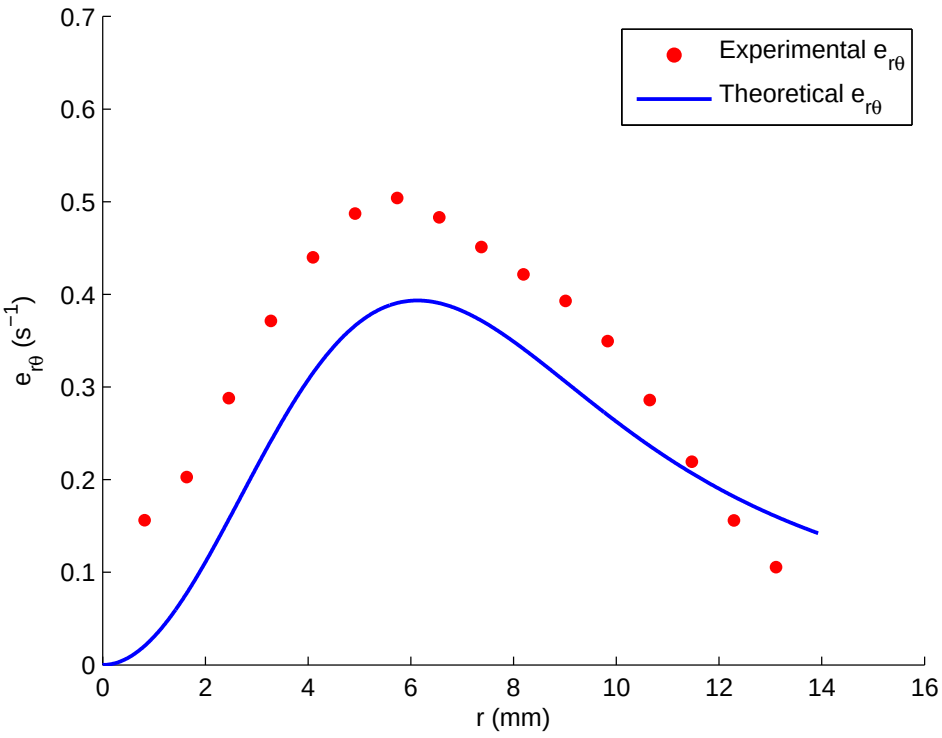

Figure 4.10: Profiles of $e_{r\theta}$ comparing the theoretical prediction to the experimental data for Turbulence Level 3.

4.2 Behavioral Assay Results

This section presents the copepod swimming behavior results. Recall that Turbulence Levels 2 and 3 were selected because copepod behavior data collected in the Webster et al. [2004] T-Box and published in Yen et al. [2008] indicated a significant change in copepod swimming kinematics between Turbulence Levels 2 and 3, and we hypothesize that the change is due to a behavioral response to the finescale turbulent vortex structure. Therefore, similarly drastic changes in copepod swimming kinematics are expected in the Burgers′s vortex apparatus between Turbulence Levels 2 and 3 treatments.

4.2.1 Turbulence Level 2 Behavioral Assays

4.2.1.1 Turbulence Level 2 Swimming Kinematics

Table 4.3 shows the mean values of relative swimming speed, turn frequency, angle of alignment with the vortex axis, net-to-gross displacement ratio, escapes per copepod per 5 seconds, and escape acceleration for the Turbulence Level 2 cases (Control A and B, Treatment A and B, where A and B signify the replicate). Overall the data for Turbulence Level 2 appears inconclusive. The mean relative swimming speed and the mean net-to-gross displacement both significantly increase from the control to the treatment, and both the treatment and the replicate have a significant effect on the parameters. Though the effect of the treatment on these two parameters is significant, this result is not definitive, as the replicate effect is also significant, therefore the true cause of the variability in these parameters is uncertain. Neither the treatment nor the replicate are significant for the escapes per copepod per 5 seconds data, the mean alignment with the vortex axis, or the mean turn frequency. It appears that the mean escape acceleration significantly increases from control to treatment, however only the effect of the replicate is significant. Therefore, this result is due to the drastic difference between replicates A and B, rather than the effect of treatment.

Based on these findings, it is reasonable to conclude that the presence of a Turbulence Level 2 Burgers′ vortex does not significantly affect copepod swimming kinematics. The data show that the replicate is responsible for the variability between control and treatment in the Turbulence Level 2 data set, and that the effect of the treatment itself (the presence of the vortex) is murky at best.

Table 4.3: Mean values of kinematic parameters for Turbulence Level 2, as well as the P-values for the effect of both the treatment (i.e., treatment or control) and the replicate (i.e., A or B). P-values marked with a * are considered significant (< 0.05).

	Cont. A	**Cont. B**	**Treat. A**	**Treat. B**	**Treat. P-Value**	**Repl. P-Value**
***Relative* Speed** (mm/s)	4.30	2.59	4.72	4.14	0.0007*	0.0002*
Turn Freq.	0.891	0.869	0.860	0.884	0.6565	0.4318
Axis Alignment $(^\circ)$	63.65	61.06	66.22	63.35	0.0643	0.1008
NGDR	0.408	0.525	0.654	0.619	0.0001*	0.0164*
Escapes per Copepod per 5 **sec.**	0.01664	0.01384	0.01406	0.01381	0.1502	0.0899
Escape Accel. (mm/s^2)	205.84	148.78	179.75	190.76	0.4116	0.0002*

4.2.1.2 Turbulence Level 2 Escape Location Analysis

Figure 4.11 shows the normalized histograms of escape jump location as a function of radius for the two Turbulence Level 2 Control replicates (A and B). These histograms are discrete PDF's that have been normalized by the effective area of each bin - each bin represents an annulus in physical space. As such they graphically represent the escape jump density as a function of radial position. Figure 4.11 does not seem to show a clear preferred escape jump location for either Turbulence Level 2 Control replicate A or B (disregarding the spike at a radius of approximately 17.5 *mm* for Control replicate B). This result is to be expected; no flow is present in the tank during the control cases, therefore there are no hydrodynamic cues to trigger an escape jump.

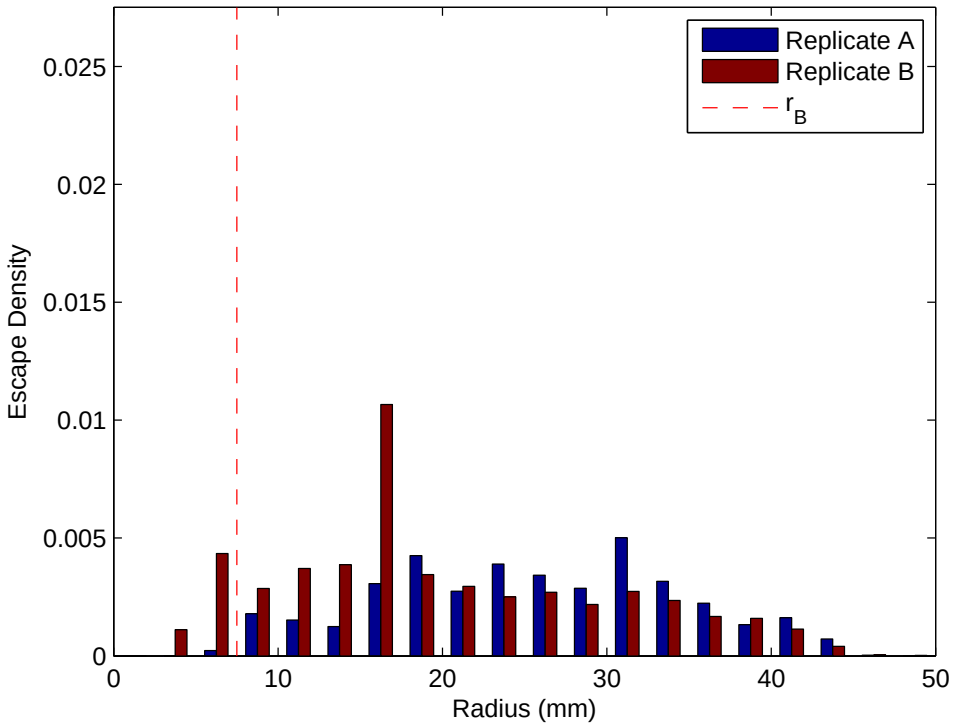

Figure 4.11: Normalized histogram of escape jump locations as a function of radius for the Turbulence Level 2 Controls. The histograms are normalized by the area of the annulus corresponding to the radial location in order to account for the varying area of the bin region. The vortex radius, r_B, equals 7.5 mm for Turbulence Level 2.

Figure 4.12 shows the normalized histograms of escape jump location as a function of radius for the two Turbulence Level 2 Treatment replicates (A and B). The term "Treatment" indicates the presence of a vortex generated by the Burgers′ vortex apparatus. The plot shown in Figure 4.12 indicates a slight increase in escape jump density towards to core of the vortex (at $r = 0$) for Turbulence Level 2 Treatment replicate A; however, this preference is very mild. Turbulence Level 2 Treatment replicate B exhibits no such behavior, appearing essentially indistinguishable from the Turbulence Level 2 Control replicates. Cumulatively, the escape jump density for copepods in the presence of a Turbulence Level 2 vortex varies very little, if at

all, from the escape jump density for copepods in stationary fluid (the Turbulence Level 2 Control replicates). This provides further validation of the results obtained in Section 4.2.1.1, i.e., that the presence of the Turbulence Level 2 vortex does not significantly influence copepod behavior.

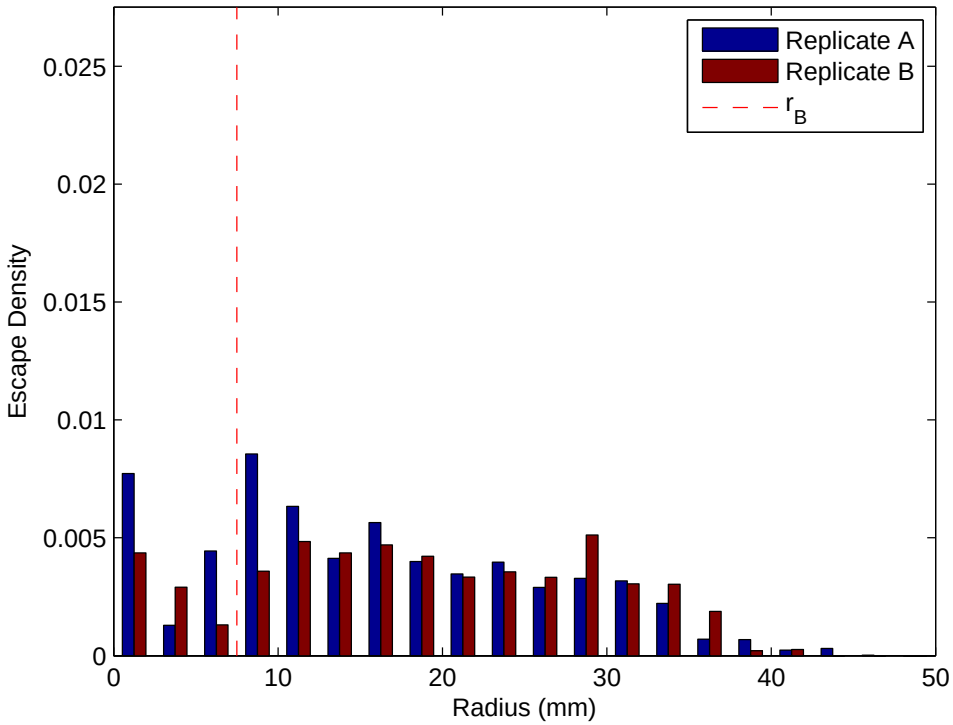

Figure 4.12: Normalized histogram of escape jump locations as a function of radius for the Turbulence Level 2 Treatments. The histograms are normalized by the area of the annulus corresponding to the radial location in order to account for the varying area of the bin region. The vortex radius, r_B, equals 7.5 mm for Turbulence Level 2.

4.2.2 Turbulence Level 3 Behavioral Assays

4.2.2.1 Turbulence Level 3 Swimming Kinematics

Table 4.4 shows the mean values of relative swimming speed, turn frequency, angle of alignment with the vortex axis, net-to-gross displacement ratio, escapes per copepod per 5 seconds, and escape acceleration for the Turbulence Level 3 cases

(Control A and B, Treatment A and B, where A and B signify the replicate). The statistical analysis of the Turbulence Level 3 behavioral data reveal a much clearer picture than the Turbulence Level 2 data.

There is a significant effect of treatment but not replicate on the mean relative swimming speed, the mean turn frequency, the mean alignment with the vortex axis, the mean net-to-gross displacement ratio, and the mean escape acceleration parameters. Neither the treatment nor the replicate is significant for escapes per copepod per 5 seconds data. These findings indicate that the replicate does not significantly affect the Turbulence Level 3 data set, and allows pooling of the data (i.e., combining replicates A and B). The ANOVA results for the combined data set are shown in Table 4.5.

Table 4.4: Mean values of kinematic parameters for Turbulence Level 3, as well as the P-values for the effect of both the treatment (i.e., treatment or control) and the replicate (i.e., A or B). P-values marked with a * are considered significant (< 0.05).

	Cont. A	**Cont. B**	**Treat. A**	**Treat. B**	**Treat. P-Value**	**Repl. P-Value**
***Relative* Speed** (mm/s)	3.07	3.66	7.46	5.94	$< 0.0001^*$	.2731
Turn Freq.	0.931	0.885	0.887	0.862	0.0387^*	0.0744
Axis Alignment $(^\circ)$	63.82	60.91	65.18	66.30	0.0008^*	0.0935
NGDR	0.403	0.434	0.597	0.582	$< 0.0001^*$	0.6304
Escapes per Copepod per 5 sec.	0.01451	0.01639	0.01431	0.01579	0.6283	0.1296
Escape Accel. (mm/s^2)	207.59	189.66	257.65	237.92	0.0005^*	0.3964

As shown in Table 4.5, Turbulence Level 3 results in clearly defined changes in copepod swimming kinematics from control to treatment. The *Acartia tonsa* swim substantially faster relative to the ambient flow velocity in the presence of Turbulence Level 3 vortex (significantly higher mean relative swim speed in the treatment than the control). They also swim in a straighter path in the presence of Turbulence Level 3 vortex, and turn less frequently (significantly higher net-to-gross displacement ratio, and significantly lower turn frequency). These three behaviors combine to move the copepod away from the vortex more quickly. Further, the copepods travel more orthogonal to the central axis in the presence of Turbulence Level 3 vortex, as seen in the significant increase in mean angle of alignment with the vortex axis. Recall that an angle of 0° would indicate the trajectory is exactly parallel to the vortex axis, whereas an angle of 90° is exactly orthogonal. This indicates that the copepods not only travel faster and in a straighter path to avoid or escape the vortex, they also orient their direction of travel to achieve the same. While the copepods do not escape more frequently (no significant change in escapes per copepod per 5 seconds), when they do escape, they do so far more powerfully, with significantly higher mean escape accelerations in the presence of the Turbulence Level 3 vortex than in the control case.

Table 4.5: Mean swimming kinematics values of the pooled Turbulence Level 3 data set (i.e., combining replicates A and B), as well as the P-value of the corresponding ANOVA tests. P-values marked with a * are considered significant (< 0.05).

	Control	**Treatment**	**P-Value**
***Relative* Speed** (mm/s)	3.41	6.66	$< 0.0001^*$
Turn Freq.	0.905	0.874	0.0332^*
Axis Alignment $(^\circ)$	62.14	65.77	0.0006^*
NGDR	0.421	0.589	$< 0.0001^*$
Escapes/Copepod/5 s	0.01545	0.01508	0.2307
Escape Accel. (mm/s^2)	198.62	247.47	0.0031^*

Based upon the results in Tables 4.4 and 4.5, it is clear that the presence of the Turbulence Level 3 Burgers′ vortex strongly influences copepod behavior via specific changes in swimming kinematics that appear to move the copepod away from the vortex core.

4.2.2.2 Turbulence Level 3 *Escape Location Analysis*

Figure 4.13 shows the normalized histograms of escape jump location as a function of radius for the two Turbulence Level 3 Control replicates (A and B). As was the case with the Turbulence Level 2 Control replicates (Figure 4.11), the Turbulence Level 3 Control replicates (Figure 4.13) do not show a clear preferred escape jump location for either replicate A or B. Again, this result is to be expected; no flow is present in the tank during the control cases, therefore there are no hydrodynamic cues to trigger an escape jump.

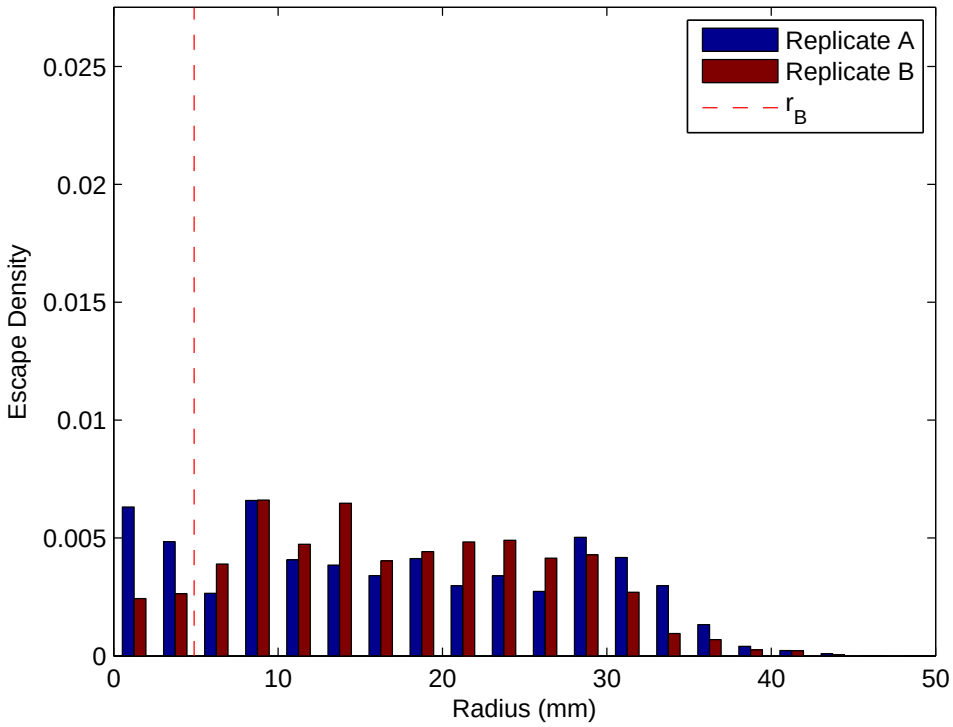

Figure 4.13: Normalized histogram of escape jump locations as a function of radius for the Turbulence Level 3 Controls. The histograms are normalized by the area of the annulus corresponding to the radial location in order to account for the varying area of the bin region. The vortex radius, r_B, equals 4.9 mm for Turbulence Level 3.

Figure 4.14 shows the normalized histograms of escape jump location as a function of radius for the two Turbulence Level 3 Treatment replicates (A and B). Both replicates of the Turbulence Level 3 treatment (Figure 4.14) exhibit large spikes in escape jump density inside (closer to the vortex core) the vortex radius, r_B. This is consistent with the conclusion drawn in Section 4.2.2.1, i.e., the presence of a Turbulence Level 3 vortex dramatically alters copepod swimming kinematics and escape behavior.

Further, it would be ideal to quantify the fluid cue that is triggering such a dramatic up-tick in escape density at radial distances closer to the vortex central axis

than r_B. To this end, consider the threshold radius (r_B) as it relates to the characteristics of the flow field of the Burgers′ vortex apparatus discussed in 4.1.2. The four most likely fluid cues that could trigger an escape response are, u_θ, maximum principal strain rate (MPSR), $e_{r\theta}$, and ω_x; recall that these are the only parameters that vary with radial position for a Burgers′ vortex flow field.

Considering the location of the peaks in u_θ, MPSR, $e_{r\theta}$, and ω_x only, r_B is closest to the location of the maximum value of u_θ. However, this cue is unlikely to be the trigger for an escape response for two reasons. First, the magnitude of u_θ is already quite high as copepods approach the center of the vortex (from a location far outside the vortex); recall that u_θ gradually increases to its peak value as one moves from large radial positions inward (see Figure 4.2). In fact, u_θ has already begun to decrease as one moves past the location of maximum u_θ towards r_B. Therefore, if one assumes that copepods have a threshold sensitivity to u_θ magnitude, the threshold will be met well outside r_B (unless the threshold u_θ magnitude is exactly $u_{\theta_{max}}$ for the Turbulence Level 3 vortex - a very unlikely event). Second, prior results by Haury [1980], Fields and Yen [1997], and Kiørboe et al. [1999] all indicated that strain rate related quantities were the least variable in eliciting an escape response from copepods.

Neither MPSR nor $e_{r\theta}$ are good candidates for triggering the escape behavior seen in these Burgers′ vortex treatments. Recall that MPSR is constant in the "near-the-vortex-core" region, increases to a maximum value at a radial position greater than r_B, and decreases back to the same constant as the "near-the-vortex-core" region at large radial positions (Figure 4.8). $e_{r\theta}$ is zero in the "near-the-vortex-core" region, increases to a maximum value at a radial position greater than r_B, and decreases back to zero at large radial positions (Figure 4.10). Similar to the reasoning for u_θ, if one assumes that copepods have a threshold sensitivity to MPSR or $e_{r\theta}$ magnitude, the threshold will be met well outside r_B.

Therefore, the most likely hydrodynamic cue for triggering the escape behavior seen in these Burgers′ vortex treatments is vorticity. Recall that vorticity is zero far away from the vortex core, and only begins to rise at a distance of approximately $2r_B$ away from the vortex core (Figure 4.6). As a copepod approaches a distance r_B away from the vortex core, the vorticity is rapidly increasing, until the vorticity peaks on the vortex centerline (Figure 4.6). This seems to contradict results by Haury [1980], Fields and Yen [1997], and Kiørboe et al. [1999] which indicated that strain rate was the least variable in eliciting an escape response from copepods. However, these results are not entirely incompatible with previous findings; vorticity (through the rotation tensor) and strain rate are both components of the velocity gradient tensor (see Equation 2.1), hence they both relate to spatial gradients of velocity. Therefore, if copepods can sense the differential velocity associated with strain rate using their setal array, then they similarly would be able to sense the differential velocity associated with vorticity.

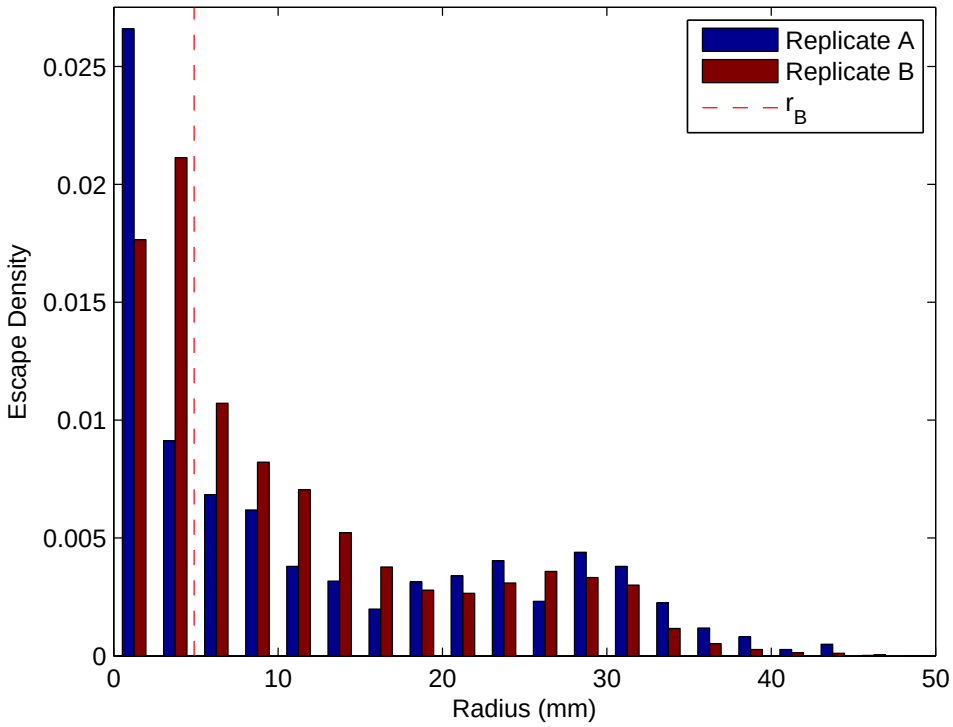

Figure 4.14: Normalized histogram of escape jump locations as a function of radius for the Turbulence Level 3 Treatments. The histograms are normalized by the area of the annulus corresponding to the radial location in order to account for the varying area of the bin region. The vortex radius, r_B, equals 4.9 mm for Turbulence Level 3.

CHAPTER V

SUMMARY AND CONCLUSIONS

5.1 Summary

A device, dubbed the "Burgers′ Vortex Apparatus", was built to create a steady state theoretical Burgers′ vortex flow field in a small tank, such that copepod behavioral assays could be conducted to examine copepod response to the flow field. The Burgers′ vortex flow field was calibrated to mimic turbulence cartoons [Jumars et al., 2009] corresponding to two turbulence intensity levels described by Webster et al. [2004] as Level 2 ($\epsilon = 0.009\ cm^2/s^3$) and Level 3 ($\epsilon = 0.096\ cm^2/s^3$), which span an apparent behavior transition in copepods [Yen et al., 2008]. Tomographic Particle Image Velocimetry (Tomo - PIV) was used to fully quantify the three-dimensional flow field, both to examine how well the generated vortex flow field matched a theoretical Burgers′ vortex solution and to "calibrate" the vortex with the appropriate turbulence cartoon. *Acartia tonsa* behavioral assays were conducted in the Burgers′ vortex apparatus to examine copepod response to Level 2 and Level 3 vortices. The objective of this analysis is to examine the validity of the hypothesis that copepods purposely move away from regions of high turbulence intensity.

The Burgers′ vortex apparatus vortices consistently mimicked the u_θ, u_x, MPSR, $e_{r\theta}$, and ω_x profile shapes of the corresponding theoretical Burgers′ vortices. The Burgers′ vortex apparatus flow field generally exhibited higher u_θ, u_x, MPSR, and $e_{r\theta}$ magnitudes than the corresponding theoretical Burgers′ vortex. The experimental ω_x profiles matched the theoretical ω_x magnitudes better, and were nearly identical in shape. The parameters of the vortices generated in the Burgers′ vortex apparatus, specifically the axial strain rate parameter, a, circulation, Γ, and characteristic vortex

radius, r_B, all aligned well with the parameters of the vortex cartoons corresponding to Level 2 and 3 turbulence intensities in the Webster et al. [2004] T-Box (Tables 2.1, 2.2, and 2.3).

Acartia tonsa exhibited no meaningful changes in swimming kinematics or escape behavior in the presence of the Turbulence Level 2 vortex. Conversely, they exhibited drastic changes in swimming kinematics and escape behavior in the presence of the Turbulence Level 3 vortex. As summarized in Table 5.1, *Acartia tonsa* increased relative swim speed, angle of alignment with the vortex axis, net-to-gross displacement ratio, and escape acceleration, as well as decreased turn frequency, when in the presence of a Turbulence Level 3 vortex (relative to control).

Table 5.1: Behavioral response changes from control to treatment (presence of a Turbulence Level 3 vortex) of *Acartia tonsa*. Indicators marked with a * are considered significant (< 0.05).

Behavior Statistic	**Control to Level 3 Vortex**
***Relative* Speed** (mm/s)	$\uparrow^*$
Turn Freq.	$\downarrow^*$
Axis Alignment $(^\circ)$	$\uparrow^*$
NGDR	$\uparrow^*$
Escapes/Copepod/$5\ s$	no change
Escape Accel. (mm/s^2)	$\uparrow^*$

Further, the normalized histograms of escape density revealed an increase in escape density near the vortex core region when copepods were exposed to a Turbulence Level 3 vortex (Figure 4.14). The normalized histograms of escape density for the Turbulence Level 2 vortex exhibited no such behavior (Figure 4.12).

5.2 Conclusions

The flow data collected through Tomo-PIV clearly indicate that the moniker "Burgers′ Vortex Apparatus" is apt. The device is capable of generating a flow field that accurately mimics the characteristics of a theoretical Burgers′ vortex with the same axial strain parameter, a and circulation, Γ. The shapes of the u_θ, u_x, MPSR, $e_{r\theta}$, and w_x profiles (compared with the same profiles for the theoretical vortex) constitute compelling evidence of this. Further, the Turbulence Level 2 and 3 vortices generated in this device are very accurately mimicking the characteristics of the desired turbulence cartoons that correspond to turbulence intensity Levels 2 and 3 in the Webster et al. [2004] T-Box, as shown by the comparison of target and obtained axial strain rate parameter, circulation, and characteristic vortex radius in Tables 4.1 and 4.2. It is therefore reasonable to conclude that the Burgers′ vortex apparatus is an effective and appropriate device for generating Burgers′ vortices that represent turbulence cartoons for the nearly isotropic turbulence characteristics of turbulence intensity Levels 2 and 3 in the Webster et al. [2004] T-Box.

Further, the Burgers′ vortex apparatus is an effective platform for conducting behavioral assays of copepod response to turbulence. The behavioral assays conducted with *Acartia tonsa* indicated that the copepods did not respond to the presence of Turbulence Level 2 vortices. However, the response to Turbulence Level 3 vortices was significant for several kinematic parameters. The copepods clearly exhibited behavior aimed at removing themselves from the presence of the Level 3 vortex. This confirms the hypothesis that copepods exhibit behavioral responses to the fluid flow structure associated with finescale turbulence. This is also consistent with the concept that there is a threshold turbulence intensity above which *Acartia tonsa* will alter their swimming behavior to avoid.

Considering the locations of *Acartia tonsa* escape behavior in the presence of a Turbulence Level 3 vortex as compared to the flow field characteristics it appears

that, in this particular case, the hydrodynamic cue that is likely triggering the escape response is vorticity. This is evidenced by the location of increase in escape density (at radial distances from the vortex core less than r_B) and the corresponding high value of vorticity at that same location.

Overall, this study provides strong evidence confirming the hypothesis that the copepod *Acartia tonsa* purposely moves away from regions of high turbulence intensity. *Acartia tonsa* exhibited a host of changes to swimming kinematics in the presence of a Turbulence Level 3 vortex that direct the animal away from the vortex region. Further, the turbulence intensity that triggers this behavior appears to lie somewhere between the Webster et al. [2004] T-Box Levels 2 and 3, as the presence of Turbulence Level 2 vortices did not evoke this response in *Acartia tonsa*.

5.3 Future Directions

Due to time constraints, no attempt was made to reproduce the Level 1 and Level 4 turbulence intensities in the Webster et al. [2004] T-Box experiments. Doing so would provide additional flow data to further validate the Burgers′ vortex apparatus as an effective generator of Burgers′ vortex turbulence cartoons, and the subsequent behavioral trials would provide additional copepod swimming kinematics data to further corroborate the conclusion drawn in this study (i.e., for Turbulence Level 1 copepods should exhibit similar behavior to Turbulence Level 2 - no response, and for Turbulence Level 4 copepods should exhibit similar behavior to Turbulence Level 3 - attempt to move away from the vortex).

Similarly, due to time constraints, the only copepod behavioral trials presented in this study are of *Acartia tonsa*. A natural next step would be to perform the same experiments upon another species of copepod. Indeed, the video data of the copepod behavioral assays has already been collected for *Temora longicornis*, and awaits digitization and tracking. This is particularly of interest because *Acartia tonsa*

is a hop-sink swimmer, whereas *Temora longicornis* is a cruise swimmer. Further, these species have disparate setae array morphology, which suggests they differ in their flow sensing abilities.

Lastly, one could examine how copepod response varies (if at all) in the presence of vortices with identical characteristics, but oriented in a different direction. As the vortex presented in this study is horizontal, the next logical step seems to be examining copepod response to a vertical Burgers′ vortex. This idea was suggested at the 2014 Ocean Sciences Conference by Dr. David Fields in order to evaluate the effects of vortex alignment on the behavior response. A few significant modifications on the original Burgers′ vortex apparatus design will have to be implemented to effectively perform these experiments, particularly the mechanism by which fluid is withdrawn out of the "top" drive shaft.

References

G.A. Boxshall, J. Yen, and R. Strickler. Functional significance of the sexual dimorphism in the cephalic appendages of *Euchaeta rimana*. *Bulletin of Marine Science*, 61(2):387–398, 1997.

C. Bronmark and L. Hansson. *The Biology of Lakes and Ponds*. Oxford University Press, New York, 2005.

J.M. Burgers. A mathematical model illustrating the theory of turbulence. *Advances in Applied Mechanics*, 1:171–199, 1948.

P.A. Davidson. *Turbulence: An Introduction for Scientists and Engineers*. Oxford University Press, Oxford, 2004.

J.F. Dower, T.J. Miller, and W.C. Leggett. The role of microscale turbulence in the feeding ecology of larvel fish. *Advances in Marine Biology*, 31:169–220, 1997.

G.E. Elsinga, F. Scarano, B. Wieneke, and B.W. van Oudheusden. Tomographic particle image velocimetry. In *6th International Symposium on Particle Image Velocimetry*, Pasadena, California, USA, 2005. a.

G.E. Elsinga, B.W. van Oudheusden, and F. Scarano. Experimental assessment of tomographic-piv accuracy. In *13th International Symposium on Applications of Laser Techniques to Fluid Mechanics*, Lisbon, Portugal, 2006a. a.

G.E. Elsinga, F. Scaranoand B. Wieneke, and B.W. van Oudheusden. Tomographic particle image velocimetry. *Experiments in Fluids*, 41:933–947, 2006b. b.

D.M. Fields and J. Yen. The escape behavior of *Pleuromamma xiphias* in response to quantifiable fluid mechanical disturbance. In P.H. Lenz, D.K. Hartline, J.E. Purcell, and D.L. MacMillan, editors, *Zooplankton: sensory ecology and physiology*, volume 1, pages 323–340. Gordon and Breach, 1996.

D.M. Fields and J. Yen. The escape behavior of marine copepods in response to quantifiable fluid mechanical disturbance. *Journal of Plankton Research*, 19:1289–1304, 1997.

D.M. Fields, D.S. Schaeffer, and M.J. Weissburg. Mechanical and neural responses from the mechanosensory hairs on the antennule of *Gaussia princeps*. *Marine Ecology Progress Series*, 227:173–186, 2002.

P.S. Galbraith, H.I. Browman, R.G. Racca, A.B. Skiftesvik, and J.F. Saint-Pierre. Effect of turbulence on the energetics of foraging in atlantic cod *Gadus morhau* larvae. *Marine Ecology Progress Series*, 281:241–257, 2004.

A.E. Gargett. Theories and techniques for observing turbulence in the ocean euphotic zone. *Scientia Marina*, 61 Suppl. 1:25–45, 1997.

T. Gotoh, D. Fukayama, and T. Nakano. Velocity field statistics in homogeneous steady turbulence obtained using a high-resolution direct numerical simulation. *Physics of Fluids*, 14:1065–1081, 2002.

T.C. Granata and T.D. Dickey. The fluid mechanics of copepod feeding in a turbulent flow: a theoretical approach. *Progress in Oceanography*, 26:243–261, 1991.

K.B. Gretchen, M. Grosell, and K.V. Brix. Toxicity of silver, zinc, copper, and nickel to the copepod *Acartia tonsa* exposed via a phytoplankton diet. *Environmental Science & Technology*, 40(6):20632068, 2006.

N. Hatakeyama and T. Kambe. Statistical laws in random strained vortices turbulence. *Physical Review Letters*, 79:1257–1260, 1997.

L.R. Haury. Experimental evaluation of the avoidance reaction of *Calanus finmarchicus*. *Journal of Plankton Research*, 2(3):187–202, 1980.

L.R. Haury, H. Yamazaki, and E.C. Itsweire. Effects of turbulent shear flow on zooplankton distribution. *Deep-Sea Research*, 37:447–461, 1990.

G. He, G.D. Doolen, and S. Chen. Calculation of longitudinal and transverse velocity structure functions using a vortex model of isotropic turbulence. *Physics of Fluids*, 11:3743–3758, 1999.

M.R. Heath, E.W. Henderson, and D.I. Baird. Vertical distribution of herring larvae in relation to physical mixing and illumination. *Marine Ecology Progress Series*, 47:211–228, 1988.

T.L. Hedrick. Software techniques for two- and three-dimensional kinematic measurements of biological and biomimetic systems. *Bioinspiration and Biomimetics*, 3: 034001, 2008.

A.G. Humes. How many copepods? *Hydrobiologia*, 292/293:1–7, 1994.

L.S. Incze, D. Hebert, N. Wolff, N. Oakey, and D. Dye. Changes in copepod distributions associated with increased turbulence from wind stress. *Marine Ecology Progress Series*, 213:229–240, 2001.

H. Jiang, T.R. Osborn, and C. Meneveau. The flow field around a freely swimming copepod in steady motion. part i: Theoretical analysis. *Journal of Plankton Research*, 24(3):167–189, 2002. a.

J. Jimenez. Oceanic turbulence at millimeter scales. *Scientia Marina*, 61:47–56, 1997.

J. Jimenez, A. Wray, P. Saffman, and R. Rogallo. The structure of intense vorticity in isotropic turbulence. *Journal of Fluid Mechanics*, 255:65–90, 1993.

P.R. Jonsson and P. Tiselius. Feeding behavior, prey detection and capture efficiency of the copepod *Acartia tonsa* feeding on planktonic ciliates. *Marine Ecology Progress Series*, 60:35–44, 1990.

P.A. Jumars, J.H. Trowbridge, E. Boss, and L. Karp-Boss. Turbulence-plankton interactions: a new cartoon. *Marine Ecology*, 30:133–150, 2009.

T. Kiørboe and E. Saiz. Planktivorous feeding in calm and turbulent environments, with emphasis on copepods. *Marine Ecology Progress Series*, 122:135–145, 1991.

T. Kiørboe and A.W. Visser. Predator and prey perception in copepods due to hydromechanical signals. *Marine Ecology Progress Series*, 179:81–95, 1999.

T. Kiørboe, E. Saiz, and A. Visser. Hydrodynamic signal perception in the copepod *Acartia tonsa*. *Marine Ecology Progress Series*, 179:97–111, 1999.

John Kitchin. MS Windows 7 kitchingroup.cheme.cmu.edu. `http://kitchingroup.cheme.cmu.edu/dft-book/images/trilinear-interpolation.png`. Accessed: 2-25-2014.

G. S. Kleppel. On the diets of calanoid copepods. *Marine Ecology Progress Series*, 99:183, 1993.

A.N. Kolmogorov. Dissipation of energy a locally isotropic turbulence. *Doklady Akademii Nauk SSSR*, 32:16–18, 1941.

P.K. Kundu and I.M. Cohen. *Fluid Mechanics*. Elsevier Academic Press, 2004.

Y. Lagadeuc, M. Boule, and J.J. Dodson. Effect of vertical mixing on the vertical distribution of copepods in coastal waters. *Journal of Plankton Research*, 19:1183–1204, 1997.

J.R.N. Lazier and K.H. Mann. Turbulence and diffusive layers around small organisms. *Deep-Sea Research*, 36:1721–1733, 1989.

P.H. Lenz, T.M. Weatherby, W. Weber, and K.K. Wong. Sensory specialization along the first antenna of a calanoid copepod, *Pleuromamma xiphias* (crustacea). In P.H. Lenz, D.K. Hartline, J.E. Purcell, and D.L. MacMillan, editors, *Zooplankton: sensory ecology and physiology*, volume 1, pages 355–363. Gordon and Breach, 1996.

P.H. Lenz, A.E. Hower, and D.K. Hartline. Force production during pereiopod power strokes in *Calanus finmarchicus*. *Journal of Marine Systems*, 49:133–144, 2004.

D.M. Lewis. A simple model of plankton dynamics coupled with les of the surface mixed layer. *Journal of Theoretical Biology*, 234:565–591, 2005.

T.S. Lundgren. Strained spiral vortex model for turbulent fine structure. *Physics of Fluids*, 25:2193–2203, 1982.

D.L. Mackas, H. Sefton, C.B. Miller, and A. Raich. Vertical habitat partitioning by large calanoid copepods in the oceanic sub-arctic pacific during spring. *Progress in Oceanography*, 32:259–294, 1993.

B.R. MacKenzie. Turbulence, larval fish ecology and fisheries recruitment: a review of field studies. *Oceanologica ACTA*, 23:357–375, 2000.

S. Manneville, A. Maurel, F. Bottausci, and P. Petitjeans. Acoustic characterization of a stretched vortex in an infinite medium. *Lecture Notes in Physics New York then Berlin*, 2000:225–234, 2000.

C.A. Manning and A. Bucklin. Multivariate analysis of the copepod community of near-shore waters in the western gulf of maine. *Marine Ecology Progress Series*, 292:233–249, 2005.

C. Marrase, E. Saiz, and J.M. Redondo. Lectures on plankton and turbulence. *Scientia Marina*, 61:1–238, 2000.

J. Mauchline. *The Biology of Calanoid Copepods*. Academic Press, London, 1998.

C.B. Miller. *Biological Oceanography*. Blackwell Publishing, 2004.

David Murphy. *Planktonic Propulsion: The Hydrodynamics, Kinematics, and Design of Metachrony*. PhD thesis, Georgia Institute of Technology, Atlanta, GA, 2012.

D.W. Murphy, D.R. Webster, and J. Yen. A high-speed tomographic piv system for measuring zooplanktonic flow. *Limnology and Oceanography - Methods*, 10:1096 – 1112, 2012.

F. Peters and C. Marrase. Effects of turbulence on plankton: and overview of experimental evidence and some theoretical considerations. *Marine Ecology Progress Series*, 205:291–306, 2000.

P. Petitjeans. Stretching of a vortical structure: filaments of vorticity. *Europhysics News*, January/February:20–23, 2003.

S.B. Pope. *Turbulent Flows*. Cambridge University Press, Cambridge, 2000.

D.I. Pullin and P.G. Saffman. Vortex dynamics in turbulence. *Annual Review of Fluid Mechanics*, 30:31–51, 1998.

B.J. Rothschild and T.R. Osborn. Small-scale turbulence and plankton contact rates. *Journal of Plankton Research*, 10:465–474, 1988.

E. Saiz and M. Alcaraz. Free-swimming behavior of *Acartia clausi* (copepoda: Calanoida) under turbulent water movement. *Marine Ecology Progress Series*, 80: 229–236, 1992.

E. Saiz and T. Kiørboe. Predatory and suspension-feeding of the copepod *Acartia tonsa* in turbulent environments. *Marine Ecology Progress Series*, 122:147–158, 1995.

E. Saiz, A. Calbet, and E. Broglio. Effects of small-scale turbulence on copepods: the case of *Oithona davisae*. *Limnology and Oceanography*, 48:1304–1311, 2003.

F. Scarano. Iterative image deformation methods in piv. *Measurement Science and Technology*, 13:R1–19, 2002.

F. Scarano. Tomographic piv: principles and practice. *Measurement Science and Technology*, 24:012001, 2013.

R. Strickler and A. Bal. Setae of the first antennae of the copepod *Cyclops scutifer* (sars): their structure and importance. *Procedures of the National Academy of Science*, 70(9):2656–2659, 1973.

G.I. Taylor. Diffusion by continuous movements. *Proceedings of the London Mathematical Society*, 20:196–211, 1921.

H. Tennekes and J.L. Lumley. *A first course in turbulence*. MIT Press, Cambridge, MA, 1972.

Aaron Conway True. Patchiness: Zooplankton behavior in finescale vertical shear layers. Master's thesis, Georgia Institute of Technology, Atlanta, GA, 2011.

L.A. van Duren and J.J. Videler. Escape from viscosity: the kinematics and hydrodynamics of copepod foraging and escape swimming. *Journal of Experimental Biology*, 206:269–279, 2003.

A.W. Visser, H. Saito, E. Saiz, and T. Kirboe. Observations of copepod feeding and vertical distribution under natural turbulent conditions in the north sea. *Marine Biology*, 138:1011–1019, 2001.

D.R. Webster, A. Brathwaite, and J. Yen. A novel laboratory apparatus for simulating isotropic oceanic turbulence at low reynolds number. *Limnology and Oceanography: Methods*, 2:1–12, 2004.

P.H. Wiebe, C.S. Davis, and C.H. Greene. Visualizing life in the ocean interior. *Oceanus*, 35:100–106, 1992.

B. Wieneke. Volume self-calibration for 3d particle image velocimetry. *Experiments in Fluids*, 45:549–556, 2008.

C.B. Woodson, D.R. Webster, M.J. Weissburg, and J. Yen. Response of copepods to physical gradients associated with structure in the ocean. *Limnology and Oceanography*, 50:1552–1564, 2005.

H. Yamazaki. Turbulence problems for planktonic organisms. *Marine Ecology Progress Series*, 139:304–305, 1996.

H. Yamazaki and K.D. Squires. Comparison of oceanic turbulence and copepod swimming. *Marine Ecology Progress Series*, 144:299–301, 1996.

J. Yen. Life in transition: balancing inertial and viscous forces by planktonic copepods. *The Biological Bulletin*, 198:213–224, 2000.

J. Yen and D.M. Fields. Escape responses of *Acartia hudsonica* nauplii from the flow field of *Temora longicornis*. *Archiv fur Hydrobiologie Beiheft*, 36:123–134, 1992.

J. Yen, P.H. Lenz, D.V. Gassie, and D.K. Hartline. Mechanoreception in marine copepods: Electrophysical studies on the first antennae. *Journal of Plankton Research*, 14:495–512, 1992.

J. Yen, K.D. Rasberry, and D.R. Webster. Quantifying copepod kinematics in a laboratory turbulence apparatus. *Journal of Marine Systems*, 69:283–294, 2008.

M. Yokokawa, K. Itakura, A. Uno, T. Ishihara, and Y. Kaneda. 16.4-tflops direct numerical simulation of turbulence by a fourier spectral method on the earth simulator. In *Proceedings of the ACM/IEEE conference on Supercomputing*, Baltimore, Maryland, USA, 2002.

Jerrold H. Zar. *Biostatistical Analysis, 4th Edition*. Prentice Hall, Upper Saddle Hall, NJ, 1999.